Model Predictions for the Spin Susceptibility of Cuprates

Dissertation

zur

Erlangung der naturwissenschaftlichen Doktorwürde

(Dr. sc. nat.)

vorgelegt der

Mathematisch-naturwissenschaftlichen Fakultät

der

Universität Zürich

von

Tamás Mayer

aus

Ungarn

Promotionskomitee

Prof. Dr. Hugo Keller (Vorsitz)

Prof. Dr. Peter Fritz Meier (Leitung der Dissertation)

Prof. Dr. Hans Beck

Zürich, 2005

Contents

Abstract

So far calculations of the spin susceptibility χ in cuprates have been performed in the framework of weak coupling approximations. However, it is known that cuprates belong to Mott–Hubbard doped materials where electron correlations are important. In this work the effects of strong correlations on high–T_c superconductors are investigated.

In the first part a new analytic expression for the spin susceptibility below T_c is proposed, which is obtained for a model that is closely related to those based on the idea of the formation of copper–oxygen singlets in layered cuprates. The superconducting energy gap is introduced phenomenologically, since the interactions which lead to pairing in cuprates are still not clear.

To clarify the differences of the results obtained in weak and strong coupling approximations, we perform in the second part numerical calculations based on the weak coupling limit. In particular, the spin susceptibility is evaluated using parameter values adapted to measurements of the Fermi surface, neutron scattering and NMR data. Possible superconducting gap symmetries are investigated, including s–wave and d–wave types of pairing symmetry.

In the third part the spin susceptibility in the so–called singlet–correlated band model is studied numerically, based on previous knowledge gained from the weak coupling limit. Using parameter values from Fermi surface measurements, the temperature dependence of various NMR properties in the superconducting state is calculated, including Knight shifts, spin–spin relaxation and spin–lattice relaxation rates. It is shown that within the framework of the proposed model the observed NMR and neutron scattering phenomena in the superconducting state can be accounted for by utilizing the Fermi surface from photoemission experiments. Therefore a very interesting connection is found between the results of surface and bulk experiments.

Zusammenfassung

Die bisherigen Berechnungen der Spinsuszeptibilität χ in Kuprat–Supraleitern wurden im Rahmen von Approximationen durchgeführt, die auf der Annahme von schwacher Kopplung der praktisch frei beweglichen Ladungsträger an das Ionengitter basieren. Es ist jedoch bekannt, dass Kuprate zu den Mott–Hubbard dotierten Materialien gehören, bei denen Elektronenkorrelationen eine wichtige Rolle spielen. In der vorliegenden Arbeit wird untersucht, welche Auswirkungen diese starken Korrelationen auf χ von Hoch–Temperatur Supraleitern haben.

Im ersten Teil wird ein neuer analytischer Ausdruck für χ vorgeschlagen, welcher auf einem speziellen Hubbard Modell beruht. Die Energielücke im supraleitenden Zustand wird phänomenologisch eingeführt, da die Wechselwirkungen, die zur Paarung in Kupraten führen, noch umstritten sind.

Um die Unterschiede der Resultate zwischen schwachen und starken Korrelationen klarzulegen, wird im zweiten Teil zunächst wieder auf die Näherung der schwachen Korrelationen eingegangen. Aufgrund von verbesserter Auflösung in Photoemissionsspektroskopie sind die Fermiflächen in Kupraten vor kurzem genau gemessen worden. Daraus lassen sich Parameterwerte, welche die kinetische Energie der Ladungsträger beschreiben, genau bestimmen. Diese Werte werden in der Modellrechnung verwendet, um sowohl die Temperaturabhängigkeiten von verschiedenen NMR Experimenten als auch die Resultate inelastischer Neutronenstreuung zu erklären. Es werden verschiedene Symmetrien für die Energielücke untersucht, die aufgrund von s– und d–wellenartiger Paarungssymmetrie möglich sind.

Im dritten Teil wird die Spinsuszeptibilität im Falle von starken Korrelationen untersucht und mit den Resultaten der schwacher Kopplung und den Experimenten verglichen. Es wird gezeigt, dass im Rahmen des Modells unter Berücksichtigung starker Korrelationen alle Experimente, die direkte Informationen über χ liefern, mit einem einzigen Satz von Parameterwerten erklärbar sind.

1 Introduction

Superconductivity was discovered in 1911 in Holland by H. K. Onnes [63], when he observed a sudden (and unexpected) drop in the electrical resistivity of mercury below 4.15 K. Despite great scientific effort, the quantum theory of superconductivity by Bardeen, Cooper and Schrieffer (BCS) [1] came 46 years after the discovery, in 1957. This theory, which explains the fascinating properties of superconductors from first principles, is widely considered (along with Landau's Fermi–liquid theory) as one of the most successful theories in condensed matter physics.

Among the most profound predictions of the theory is the existence of coherence factors in the transition probabilities in the superconducting state. This phase coherence among the wave functions of the occupied one electron states leads to "case–I" and "case–II" interactions, depending on whether the perturbation is even (like for ultrasonic absorption) or odd (like for nuclear relaxation) under time reversal. This results in theoretically distinct processes which can be tested experimentally. In the case of ultrasonic attenuation, a sharp drop was predicted upon entering the superconducting state and was confirmed experimentally by Morse [59] in 1959. On the other hand, in the nuclear relaxation rate there is a large increase upon entering the superconducting state, followed by an exponential drop at lower temperatures. This behavior was confirmed experimentally by Hebel and Slichter [34] in 1957. This so–called "Hebel–Slichter" peak is one of the distinctive features of "low–temperature" superconductors.

In the year 1986, Bednorz and Müller [5] discovered a new family of superconductors, named as "high–temperature" superconductors because of their high transition temperatures. It was soon clear that the superconductivity in these new materials cannot be explained within the framework of existing theories. One example is the absence of the above mentioned Hebel–Slichter peak in the measured nuclear relaxation rate of high–temperature superconductors. To date there exists no widely accepted theory for cuprate superconductors.

The measured nuclear relaxation rate in metals is directly related to the so–called spin susceptibility of itinerant electrons. Therefore the spin susceptibility of cuprates is the focus point of many ongoing investigations. Experiments related to the spin susceptibility comprise the temperature dependence of the Knight shift, spin–spin and spin–lattice relaxation rates as

well as inelastic neutron scattering (INS) measurements. The most complete set of experimental data have been obtained for the Y–Ba–Cu–O compounds.

The theoretical approaches to the spin susceptibility can be separated into two parts. The first one deals with a single–band Hubbard model with the effective Coulomb interaction U_e taken to be of the order of the bandwidth in cuprates (weak coupling limit). Based on this assumption, the dynamical spin susceptibility can be calculated within a standard random–phase approximation (RPA) approach. Extensive studies of nuclear magnetic resonance (NMR) data were carried out within the framework of this model by Bulut and Scalapino [14] between 1990–1994 and Mack et al. in 1998 [50]. In the meantime, the features observed by inelastic neutron scattering were studied theoretically by several groups. For the most recent developments in this topic see I. Eremin et al. [23, 24]. However, in all of these calculations the effect of electronic correlations were not taken into account properly.

At the same time, there were a number of studies, devoted to analyzing the spin susceptibility within the strong coupling t–J model [4, 64, 65, 73, 80], for which standard many–body perturbative methods do not work. It has been found that to a large extent, both weak and strong coupling calculations agree with each other. However, so far there is no complete understanding whether both INS and NMR data can be explained consistently within one model, using the same parameter values of the given theory.

In the present work we analyze this question in detail. In collaboration with M. Eremin (Kazan State University) and I. Eremin (Freie Universität Berlin) we have investigated the effect of strong correlations on high–T_c superconductors. Starting from the singlet–correlated band model [27], we use a well established decoupling procedure of the equation of motion and approximate higher order correlation functions so as to obtain an analytical expression for the dynamical spin susceptibility which takes into account strong correlations. It has been found by Hubbard and Jain [42] already in 1968 that the dynamical susceptibility expression has a non–trivial correction due to strong correlation effects. This correction is different from the conventional Pauli–Lindhard susceptibility, therefore it cannot be exactly included in the RPA approach. It has been found later by I. Eremin [21] that this correction term should be modified due to the contribution to the spin susceptibility from the lower Hubbard band, even if the latter is completely filled. In 1998 Zavidonov and Brinkmann [86] have incorporated the local spin fluctuation effect in a more systematic way, using a low Hubbard sub–band model.

In the present work we extend the previous analysis and present an analytical expression for the dynamical susceptibility in the upper Hubbard sub–band in the superconducting state. The mechanism that causes the pairing in cuprates is still being debated. Therefore we have introduced the superconducting gap function phenomenologically into our model. We perform an extended numerical evaluation of these analytical expressions and find that most of the available experimental data which are directly related to the spin susceptibility can be explained consistently within one set of model parameters. These experiments include the magnetic resonance peak observed by INS and the temperature dependence of the NMR spin shift, spin–spin and the spin–lattice relaxation rates, measured in the superconducting state. In our analysis we take advantage of other available experiments, like the Fermi surface topology in various cuprate superconductors that is determined by high–resolution angle–resolved photoemission. We analyze possible pairing symmetries and by comparison to experimental results, systematically exclude all candidates, save the $d_{x^2-y^2}$–wave gap symmetry. Assuming this pairing symmetry, we propose an optimal set of parameters for the optimally doped $YBa_2Cu_3O_7$ and $Bi_2Sr_2CaCu_2O_8$ compounds.

This work is organized as follows. In the first part (Sections 2–4) we introduce the model system and present the new analytical expression for the spin susceptibility in the superconducting state of cuprates. Basic experimental facts as well as the experimental techniques for probing the spin susceptibility will also be discussed here. In the second part (Section 5) we analyze possible pairing symmetries by comparison to experiments in $YBa_2Cu_3O_7$, within the framework of the RPA susceptibility. In the third part (Section 6) we study the spin susceptibility in the singlet–correlated band model by analyzing experiments in the superconducting state of the materials $YBa_2Cu_3O_7$ and $Bi_2Sr_2CaCu_2O_8$. Section 7 contains a summary and the conclusions. Details of the derivation of the expression for the spin susceptibility are given in Appendix A.

2 Some experimental facts about cuprates

In this section we summarize the known characteristics of high–temperature superconductors. In particular, we wish to briefly discuss those aspects which will be relevant for our model system and the analyzed experiments.

2.1 Introduction

J. G. Bednorz and K. A. Müller discovered in 1986 that, with suitably chosen doping[1] δ, $La_{2-\delta}Ba_{\delta}CuO_4$ becomes a superconductor at a critical temperature T_c=30 K. Soon afterwards several other high–temperature superconducting materials have been found. Among these is $YBa_2Cu_3O_{7-\delta}$, whose critical temperature T_c=92 K is well above the condensation temperature of nitrogen (77 K). To date the highest critical temperature is $T_c \simeq 133$ K observed in $HgBa_2Ca_2Cu_3O_{8+\delta}$ by Schilling et al. [70]. All these materials contained copper and oxygen atoms in their molecular structure. Soon it was realized that the superconducting property of these materials cannot be explained in the framework of the BCS theory based only on electron–phonon interaction. There is not yet any broadly accepted theory for high–temperature superconductivity.

2.2 Pseudogap

One of the most discussed topics, related to underdoped cuprates, is the so–called pseudogap phenomenon. Experimental results show a deviation from Fermi–liquid behavior in the normal state of underdoped high–T_c superconductors, namely, a suppression of the density of states (DOS) near the Fermi level. This suppression is mostly referred to as "pseudogap behavior". It was observed in many different experiments (angle-resolved photoemission, NMR, neutron scattering, tunneling spectroscopy, specific heat etc.), among these first by NMR. In a Fermi–liquid a temperature–independent susceptibility is expected. Contrary to this, the susceptibility in high–T_c superconductors decreases with decreasing temperature.

[1] Under doping we understand the introduction of charge carriers into the crystalline structure. At optimal doping T_c is maximal. The regions below and above optimal doping are called under– and overdoped.

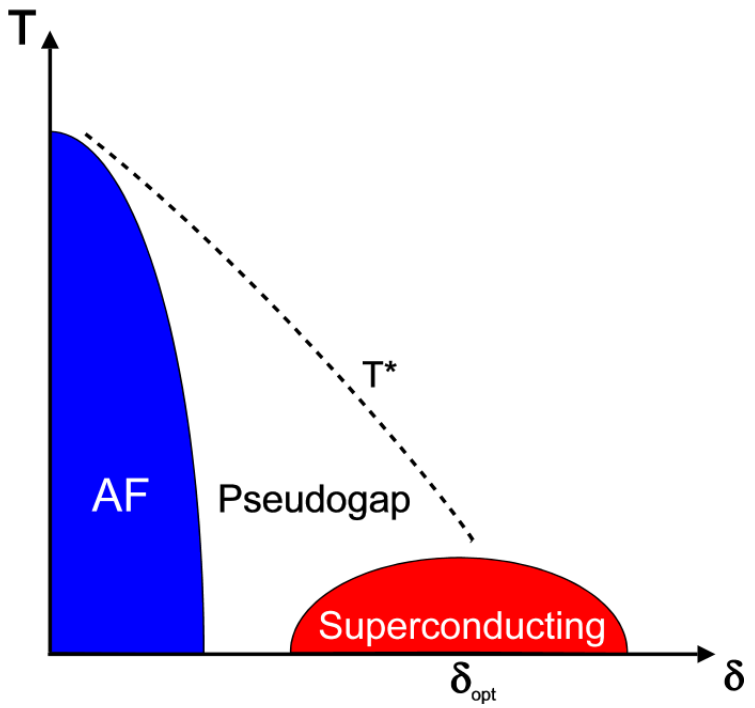

Figure 1: Schematic phase–diagram of the high–temperature superconductors.

Both Knight shift and spin–lattice relaxation measurements have indicated pseudogap–behavior. In overdoped compounds the Knight shift is practically temperature independent in the normal state. This is in accordance with our expectations based on the Pauli spin susceptibility in a metal. Below T_c the spin susceptibility decreases, because in the spin–singlet state Cooper pairs form. However, in the underdoped material K decreases (with decreasing temperature) already in the normal state and there is practically no observable change at T_c. The temperature below which the Knight shift starts to decrease in underdoped cuprates is usually denoted as T^*. The pseudogap phenomena has been observed on Cu(2), O(2,3) nuclei and also on the Y nucleus between the CuO_2–planes.

Let us consider now, how the phenomenon depends on the doping. In Figure 1 we display a possible phase–diagram of the high–temperature superconductors showing the different phases for different dopings. We must keep

in mind, however, that this phase–diagram is only schematic and has been constructed on the basis of NMR measurement data. Let us start with the non–doped ($\delta = 0$) parent compound: an antiferromagnetic (AF) insulator. Upon doping the long–range AF order is destroyed and the material becomes a metal which exhibits unusual properties. As already explained, underdoping the material results in observing a pseudogap, whereas overdoping causes the phenomenon to vanish. In the area of light overdopings, T^* (transition temperature) goes over into T_c.

A good overview of the experimental results regarding the pseudogap is provided in [82].

2.3 Crystalline structure

The crystalline structure of high–temperature superconductors is similar to the perovskite structure. In general, the perovskite structure consists of a big atom A, some transient metal T and oxygen atoms. The 6 oxygen atoms surround T and together they build a TO_6 octahedron. Figure 2 shows the crystalline structure of La_2CuO_4. The six–coordinated copper, the CuO_6 octahedron is clearly recognizable. This octahedron is distorted in the c–direction. This distortion is related to the Jahn–Teller–effect. Also recognizable in the figure is the CuO_2–plane. A common characteristics of all known high–T_c superconducting cuprates is that they contain one or several CuO_2–planes in their crystalline structure. These planes are believed to be the electronically active elements, responsible for superconductivity. The most extensively studied compounds are $YBa_2Cu_3O_{6+\delta}$ and $YBa_2Cu_4O_8$, both containing one double CuO_2–plane in their elementary cell. In Figure 3 we display the structure of $YBa_2Cu_3O_7$, with its double CuO_2–plane. Table 1 provides an overview of the most important high–temperature superconducting materials.

2.4 Electronic structure

The parent compounds of all of the high–temperature superconductors are antiferromagnetic insulators. Let us consider an ionic model and a copper atom in the CuO_2–plane. This copper is in a $3d^9$–state. Consequently, compared with a completely filled $3d^{10}$–shell, one electron is missing. The

Insulating parent compound	High–T_c superconductor	T_c^{max} [K]
La_2CuO_4	$La_{2-\delta}Ba_\delta CuO_4$	30
La_2CuO_4	$La_{2-\delta}Sr_\delta CuO_4$	38
$YBa_2Cu_3O_{6+\delta}$, $\delta < 0.4$	$YBa_2Cu_4O_8$	80
$YBa_2Cu_3O_{6+\delta}$, $\delta < 0.4$	$YBa_2Cu_3O_{6+\delta}$, $\delta > 0.4$	95
BiSrCuO	$Bi_2Sr_2Ca_2Cu_3O_{10}$	110
TlBaCuO	$Tl_2Ba_2Ca_2Cu_3O_{10}$	125
HgBaCuO	$HgBa_2Ca_2Cu_3O_{8+\delta}$	133

Table 1: Most important high–temperature superconducting materials.

missing electron, or in the hole–representation the added hole, has spin 1/2. The crystalline field triggers an energy splitting of the atomic 3d orbitals. In the O_6–octahedron the distance between the copper atom and the apex oxygen atom is larger than the distance between copper and planar oxygen atoms. As a consequence of this distortion, the antibonding $3d_{x^2-y^2}$ orbitals have the highest energy. Furthermore, the unpaired electron (hole) belongs to this atomic orbital. There is superexchange interaction between the magnetic moments of holes belonging to $3d_{x^2-y^2}$ orbitals of neighbouring Cu–ions. At low temperature, this exchange interaction supports an antiferromagnetic ordering.

By suitable doping additional electrons are removed from the CuO_2–planes. In the hole representation this means that additional holes are introduced into the CuO_2–plane. Doping can be achieved, for example, by heating up the sample in an oxygen atmosphere or by changing the composition of the planes. In $La_{2-\delta}Sr_\delta CuO_4$ some La atoms are replaced by Sr, in $YBa_2Cu_3O_{7-\delta}$ the oxygen content is modified. The immediate consequence of doping is that the antiferromagnetic ordering becomes weaker. The antiferromagnetic ordering vanishes completely at a doping level $\delta \simeq 0.04$ in $La_{2-\delta}Sr_\delta CuO_4$. At a further increased doping level, above $\delta \simeq 0.06$, the materials become conducting.

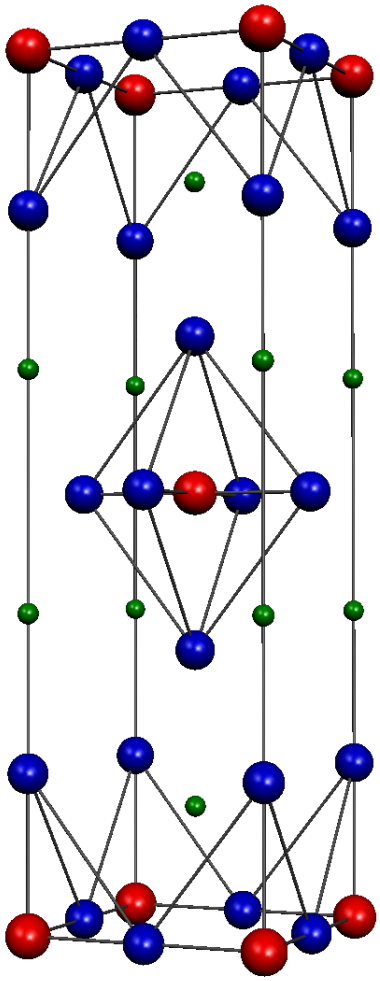

Figure 2: View of the La_2CuO_4 structure. Cu atoms are represented by red, La atoms by green and O atoms by blue balls. The six–coordinated copper and the CuO_2–planes are shown.

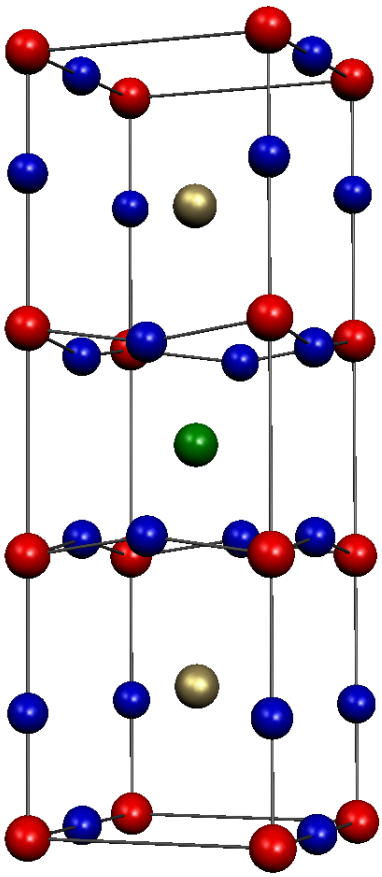

Figure 3: View of the $YBa_2Cu_3O_7$ structure. Cu are represented by red, Y atoms by green, Ba atoms by gold and O atoms by blue balls. This structure has two CuO_2–planes in the elementary cell, separated by an Y–atom.

3 Theory

3.1 Hubbard model

In this section we introduce the so–called Hubbard model. In particular, we will discuss the origin of Hubbard sub–bands and the t–J model as well as the algebra of Hubbard X–operators.

3.1.1 Hubbard sub–bands and the t–J model

The Hubbard model was introduced in 1963 [36, 37, 38, 39, 40, 41, 42] to describe strongly correlated electron systems and has been used ever since in numerous situations. It has a wide range of applications including metal–insulator transitions and the treatment of ferromagnetism, antiferromagnetism and paramagnetism. Since the discovery of the high–T_c cuprates, the model is used in various numerical and analytical forms to describe the physical phenomenon of the CuO_2–planes. In this chapter we will introduce this model, along with its basic forms and applications.

Let us consider the standard Hubbard model with the Hamilton operator in the second quantisation form

$$\mathcal{H} = \underbrace{\sum_{i,j,\sigma} t_{ij} c^{\dagger}_{i\sigma} c_{j\sigma}}_{kinetic\ energy} + \underbrace{U \sum_{i} n_{i\uparrow} n_{i\downarrow}}_{potential\ energy}, \tag{1}$$

where i indexes the lattice sites and $\sigma = \uparrow, \downarrow$ is the spin.

- The operator $c^{\dagger}_{i\sigma}$ ($c_{i\sigma}$) creates (annihilates) an electron with spin σ at lattice site i.
- $c^{\dagger}_{i\sigma} c_{j\sigma}$ transfers an electron of spin σ from lattice site j to i.
- $n_{i\sigma}$ is the number operator for electrons of spin σ at site i.
- U (Hubbard U) is the Coulomb repulsion between electrons at the same site.

- t_{ij} is the kinetic "hopping" term. According to photoemission experiments, this term may have up to five components ($t_1 ... t_5$) in high–T_c superconductors: t_1 if (i, j) are nearest neighbours (NN), t_2 if (i, j) are next nearest neighbours (NNN) etc...

To fix the expectation value of the particle number, we can introduce the chemical potential μ. The extended Hamiltonian then contains an additional term

$$\mathcal{H}' = -\mu \sum_{i,\sigma} n_{i\sigma}. \tag{2}$$

Let us now take a look at three simple cases. First we consider the case of free fermions. This means that there is no interaction and $U = 0$ holds. We can diagonalize the Hamilton operator by applying a Fourier transformation. Let

$$c_{\mathbf{k}\sigma} = \sum_i e^{-i\mathbf{k}\mathbf{R}_i} c_{i\sigma} \tag{3}$$

be the Fourier transform of the operators $c_{i\sigma}$. The Hamilton operator (1) becomes

$$\mathcal{H} = \sum_{\mathbf{k},\sigma} \varepsilon_{\mathbf{k}} c^{\dagger}_{\mathbf{k}\sigma} c_{\mathbf{k}\sigma}, \tag{4}$$

where $\varepsilon_{\mathbf{k}}$ is determined by

$$\varepsilon_{\mathbf{k}} = \sum_{i-j} t_{ij} e^{i\mathbf{k}(\mathbf{R}_i - \mathbf{R}_j)}. \tag{5}$$

In the simple case of a quadratic 2D lattice with NN and NNN hopping only, the band structure is given by $\varepsilon_{\mathbf{k}} = -2t_1 (\cos k_x + \cos k_y) - 4t_2 \cos k_x \cos k_y$. Figure 4 shows the band structure of this $t_1 - t_2$ model for various ratios t_2/t_1. The Hamiltonian in this case describes a conductor.

Next we comment shortly on the case $t_{ij} = 0$. The Hamiltonian (1) turns into

$$\mathcal{H} = U \sum_i n_{i\uparrow} n_{i\downarrow}. \tag{6}$$

We see that the hopping between the lattice sites is not possible. We have an insulator with two energy levels $\varepsilon = 0$ and $\varepsilon = U$, which give rise to

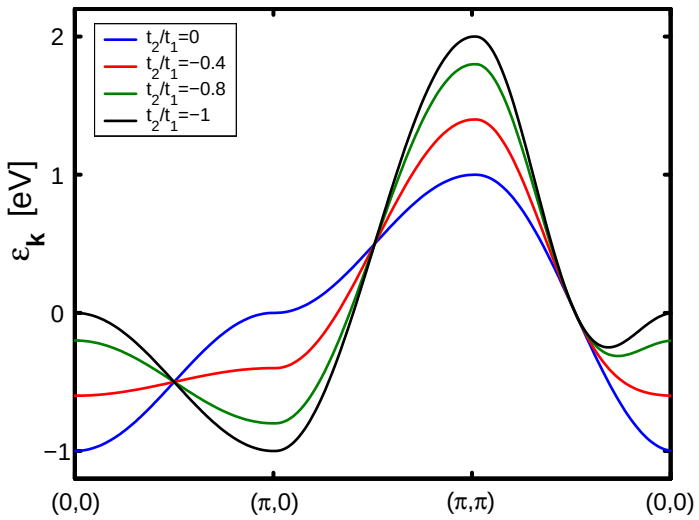

Figure 4: Band structure of the two dimensional $t_1 - t_2$ model, with $t_1 = 0.25$ eV and no interaction ($U = 0$) for various ratios t_2/t_1.

two Hubbard sub–bands, the "lower Hubbard band" (LHB) and the "upper Hubbard band" (UHB) when we consider the case of $t \neq 0$.

The situation with $t \neq 0$, $t \ll U$ is the so–called strong coupling limit [32]. The large Coulomb term U makes the double occupancy of sites improbable. If U is large enough, a gap opens in the energy spectrum and we have two bands: a LHB and an UHB with bandwidths w. The metal–insulator transition occurs at $w = U$. That means that, with varying U, we can obtain metallic or insulating systems.

To derive an effective Hamiltonian within one sub–band, we utilize a canonical Schrieffer–Wolf transformation [72]. The goal is to eliminate the coupling between the LHB and UHB in first order in t/U. The Hamiltonian (1) will be transformed to

$$\widetilde{\mathcal{H}} = e^{-S}\mathcal{H}e^{S} = \mathcal{H} + [\mathcal{H}, S] + \frac{1}{2}\left[[\mathcal{H}, S], S\right] + ..., \tag{7}$$

where $S = \mathcal{O}(t/U)$. The basic idea of the t–J model is to take into account inter sub–band hopping terms within one sub–band (usually LHB). Mathematically, it means that the Hamiltonian (1) splits into three terms

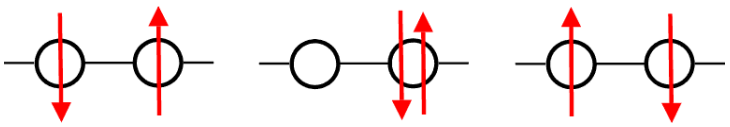

Figure 5: Antiferromagnetic exchange in the t-J model.

$$\mathcal{H} = \mathcal{H}^1_{kin} + \mathcal{H}^2_{kin} + \mathcal{H}_U, \tag{8}$$

where $\mathcal{H}^1_{kin}$ is the fraction of the kinetic term which does not change the number of doubly occupied sites, $\mathcal{H}^2_{kin}$ is the part which changes this number and $\mathcal{H}_U$ is the Coulomb term. Then we seek the operator S so, that $[\mathcal{H}_U, S] = -\mathcal{H}^1_{kin}$ holds. Thus in the transformed Hamiltonian $\widetilde{\mathcal{H}}$ the double occupancy will be excluded in first order. The solution yields the effective Hamiltonian, which is usually referred to as t–J model [88]

$$\mathcal{H}_{t-J} = \sum_{i,j,\sigma} t_{ij} \widetilde{c}^\dagger_{i\sigma} \widetilde{c}_{j\sigma} + \sum_{i,j} J_{ij} \left[(\mathbf{S}_i \mathbf{S}_j) - \frac{n_i n_j}{4} \right]. \tag{9}$$

Here $\widetilde{c}^\dagger_{i\sigma} = c^\dagger_{i\sigma} (1 - n_{i\overline{\sigma}})$ are projected operators, with factors $(1 - n_{i\overline{\sigma}})$ which exclude that two electrons simultaneously occupy the same lattice site. This means that this model considers charge fluctuations like $Cu^{2+} \leftrightarrow Cu^{+}$. In this connection one can expect that the t–J model will be relevant to electron doped cuprates like $Nd_{2-x}Ce_xCuO_4$. The exchange interaction between lattice sites occupied by spins S_i is given by $J_{ij} = 2 |t_{ij}|^2 / U$. This term describes corrections to the strict exclusion of the double occupancy (or the Cu^{3+} states). The hopping to a neighbouring site and back is possible if the spins are antiparallel. This antiferromagnetic exchange process is illustrated in Figure 5. At half filling $n = 1$ (i.e. one e^- per lattice site) the hopping is prohibited and the $t - J$ model is reduced to a Heisenberg model of localised spins

$$\mathcal{H} = J \sum_{i,j} \mathbf{S}_i \mathbf{S}_j. \tag{10}$$

3.1.2 The algebra of Hubbard X–operators

It is possible to rewrite the discussed models in a convenient way using the Hubbard projection X–operators. These are defined as follows

$$X^{\alpha,\beta} = |\alpha\rangle \langle\beta| , \tag{11}$$

where we dropped the lattice site index i for brevity.

If we take our basis as the 4 possible states : $|0\rangle$, $|\downarrow\rangle = c^{\dagger}_{i\downarrow}|0\rangle$, $|\uparrow\rangle = c^{\dagger}_{i\uparrow}|0\rangle$, $|\uparrow\downarrow\rangle = c^{\dagger}_{i\uparrow}c^{\dagger}_{i\downarrow}|0\rangle$, then the creation (annihilation) operators can be expressed in terms of the X–operators, for example:

$$c^{\dagger}_{\uparrow} = X^{\uparrow,0} + X^{2,\downarrow},$$

and vice versa

$$X^{\uparrow,0} = c^{\dagger}_{\uparrow}(1 - n_{\downarrow}) .$$

Note: we will use the notation $X^{2,\uparrow} \equiv X^{\uparrow\downarrow,\uparrow}$ in further discussions.

The Hamiltonian (1) can be rewritten as

$$\begin{aligned} \mathcal{H} &= \sum_{i,j,\sigma} t_{ij} \left[X^{\sigma,0}_i X^{0,\sigma}_j + X^{2,\sigma}_i X^{\sigma,2}_j \right] \\ &+ \sum_{i,j,\sigma} t_{ij} \left[X^{\sigma,0}_i X^{\overline{\sigma},2}_j + X^{2,\overline{\sigma}}_i X^{0,\sigma}_j \right] \\ &+ \sum_i U X^{2,2}_i . \end{aligned} \tag{12}$$

As a first step we consider $t_{ij} = 0$. In this case the operators $X^{\sigma,0}$ and $X^{\sigma,2}$ diagonalize the Hamiltonian. The corresponding quasiparticle energies are $\varepsilon_{\mathbf{k}} = 0$ (LHB) and $\varepsilon_{\mathbf{k}} = U$ (UHB). Next we allow for hopping, meaning $t_{ij} \neq 0$. In the limit $t \ll U$, the exclusion of double occupancy in first order t/U leads to the effective Hamiltonian

$$\mathcal{H}_{eff} = - \sum_{i,j,\sigma,\sigma'} \frac{|t_{ij}|^2}{U} (-1)^{1-\sigma-\sigma'} X^{\sigma,\sigma'}_i X^{\overline{\sigma},\overline{\sigma}'}_j . \tag{13}$$

Finally, the t–J model can be written as

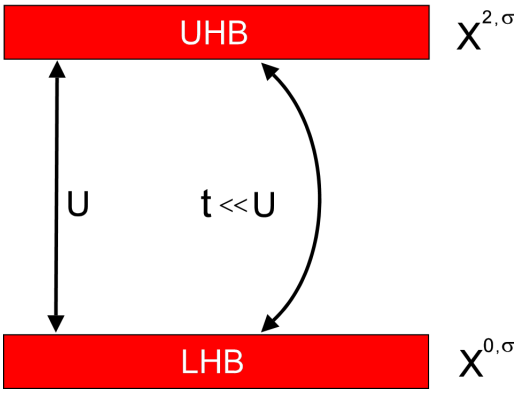

Figure 6: Schematic picture of the LHB and UHB along with the corresponding Hubbard operators.

$$\mathcal{H}_{t-J} = \sum_{i,j,\sigma} t_{ij} X_i^{\sigma,0} X_j^{0,\sigma} + \sum_{i,j} J_{ij} \left[\mathbf{S}_i \mathbf{S}_j - \frac{n_i n_j}{4} \right]. \tag{14}$$

The operator $X^{\sigma,0}$ corresponds to $\tilde{c}_{i\sigma}^{\dagger}$ from the previous section. The first term describes the hopping in the LHB, whereas the second term involves the hopping from LHB to UHB and back. This exchange coupling is of course only possible if the spins are antiparallel. Figure 6 displays the bands in this model, along with the corresponding Hubbard operators.

Let us discuss at this point some important relations, involving the Hubbard projection operators. These operators obey the completeness equation

$$X^{0,0} + X^{\uparrow,\uparrow} + X^{\downarrow,\downarrow} + X^{2,2} = 1. \tag{15}$$

Also, it is important to note that they follow the multiplication rule

$$X^{\alpha,\beta} X^{\gamma,\eta} = \delta_{\beta,\gamma} X^{\alpha,\eta}. \tag{16}$$

Other useful relations include the spin operator S^z, the doping parameter y and the total number of spins n

$$\underbrace{X^{\uparrow,\uparrow} + X^{\downarrow,\downarrow} + 2X^{2,2}}_{\substack{number\ of\ carriers \\ in\ one\ unit\ cell}} = 1 - y \tag{17}$$

$$X^{\uparrow,\uparrow} - X^{\downarrow,\downarrow} = 2S^z \tag{18}$$

$$X^{\uparrow,\uparrow} + X^{\downarrow,\downarrow} = n. \tag{19}$$

Finally, the anticommutators for these operators are related to the doping level and the spin operator as follows

$$\begin{aligned} \left\{X^{\uparrow,0}, X^{0,\uparrow}\right\} &= \frac{1+y}{2} + S^z \\ \left\{X^{2,\uparrow}, X^{\uparrow,2}\right\} &= \frac{1-y}{2} + S^z. \end{aligned} \tag{20}$$

Here we see that these operators do not fulfill the Fermi or Bose commutator relations. The question whether standard perturbation theory in terms of Feynman diagrams can be applied is therefore not trivial.

3.1.3 Electron–hole transformation

We consider the transformation $c^\dagger_{i,\sigma} = 2\sigma d_{i,-\sigma}$, $c_{i,\sigma} = 2\sigma d^\dagger_{i,-\sigma}$.

The Hamiltonian (1) becomes

$$\begin{aligned} \mathcal{H}' &= \sum_{i,j,\sigma} t_{ij} d_{i\sigma} d^\dagger_{j\sigma} + U \sum_i d_{i\downarrow} d^\dagger_{i\downarrow} d_{i\uparrow} d^\dagger_{i\uparrow} \\ &= - \sum_{i,j,\sigma} t_{ij} d^\dagger_{j\sigma} d_{i\sigma} + U \sum_i \left(1 - d^\dagger_{i\uparrow} d_{i\uparrow}\right)\left(1 - d^\dagger_{i\downarrow} d_{i\downarrow}\right) \\ &= - \sum_{i,j,\sigma} t_{ij} d^\dagger_{j\sigma} d_{i\sigma} + U \sum_i n_{i\uparrow} n_{i\downarrow} + UN - UN_h, \end{aligned} \tag{21}$$

where N is the number of unit cells and N_h is the number of the holes. As we can see, the structure of the Hamiltonian does not change except for two additive constant terms. In general this transformation is not a symmetry–transformation of the Hubbard model. However, on a bipartite lattice (such as a high–T_c superconductor's CuO_2–plane) we can utilize the canonical transformation $d_{i\sigma} \to d_{i\sigma}$ if $d_{i\sigma} \in$ lattice A, and $d_{i\sigma} \to -d_{i\sigma}$ if $d_{i\sigma} \in$ lattice B. This transformation changes the sign of the kinetic energy and our Hamiltonian becomes the same as for electrons.

3.2 Special microscopic models for high-T_c superconductors

3.2.1 First approximation or the spin–fermion model

Among the first models, which tried to describe high-T_c superconductivity, was a simple Hubbard model taking into account one hybridized $3d_{x^2-y^2}$–$2p_\sigma$ orbital, localized at the Cu site. The effect of oxygen was neglected. In this case one can utilize a 1–band model such as in Section 3.1

$$\mathcal{H} = \sum_{i,j,\sigma} t_{i,j} d^\dagger_{i\sigma} d_{j\sigma} + U \sum_i n_{i\uparrow} n_{i\downarrow}. \tag{22}$$

Here the operator $d^\dagger_{i\sigma}$ ($d_{i\sigma}$) creates (annihilates) a hole with spin σ at the orbital of site i. These operators satisfy the relation $\left\{ d^\dagger_{i\sigma}, d_{j\sigma'} \right\} = \delta_{ij}\delta_{\sigma\sigma'}$. The operator $n_{i\sigma} = d^\dagger_{i\sigma} d_{i\sigma}$ counts the number of holes with spin σ at site i. As described in Section 3.1, the first term accounts for the hopping of the particles, whereas the second term describes a Coulomb interaction. The particles are affected if they are at the same site, and they must have spin $\downarrow\uparrow$ because of the Pauli principle. A review on this model can be found in [18].

3.2.2 Copper–oxygen band for hole doped cuprates

Next we consider a more accurate model of the CuO_2–planes. This new model should include the oxygen p–orbital. Namely, upon doping, the additional hole dwells mainly at the oxygen site [62]. It is therefore necessary to

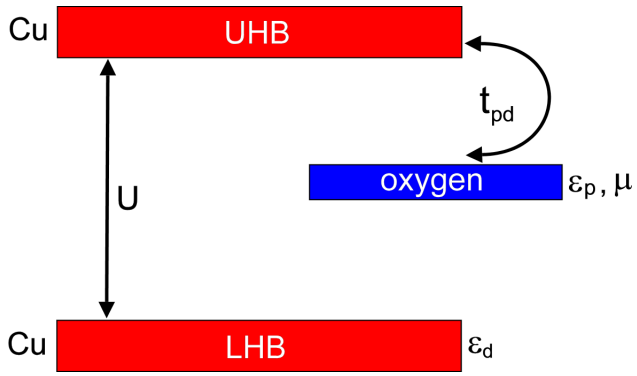

Figure 7: Energy scheme for the description of hole doped cuprate superconductors.

introduce a new p–band in the Hamiltonian

$$\mathcal{H}_0 = \varepsilon_d \sum_i n_i^d + \varepsilon_p \sum_j n_j^p + U_d \sum_i n_{i\uparrow}^d n_{i\downarrow}^d, \tag{23}$$

where ε_d, ε_p are the on–site energies of the copper and oxygen holes and U_d refers to the Coulomb interaction. Furthermore $n_i^d(n_j^p)$ are the copper 3d (oxygen 2p) hole densities at the sites i and j, respectively. The first two terms are connected to the chemical potential, the last term to the Coulomb repulsion. With the relation $\varepsilon_d < \varepsilon_p < \varepsilon_d + U_d$ we are able to describe the experimental fact that the additional holes are localized mainly at the oxygen site. Namely, further holes in the 3d–shell would require a higher energy than is needed to fill up the 2p–shells, so the holes occupy mainly the oxygen site. Figure 7 illustrates this energy scheme. The quasiparticle operators for this Hamiltonian are given by $X_i^{\uparrow,0} = d_{i\uparrow}^\dagger (1 - n_{i\downarrow})$ and $X_i^{2,\uparrow} = d_{i\downarrow}^\dagger n_{i\uparrow}$.

The lowest excitation of the system corresponds to the transfer of a hole from the 3d–orbital to the 2d–orbital. We treat this hopping t_{pd} between these orbitals as a perturbation to the energy scheme. The Hamiltonian for the hopping is given by

$$\mathcal{H}_1 = t_{pd} \sum_{i,j,\sigma} \left(d_{i\sigma}^\dagger p_{j\sigma} + p_{j\sigma}^\dagger d_{i\sigma} \right). \tag{24}$$

Figure 8 shows the CuO_2–planes along with the discussed orbitals, energies and interactions.

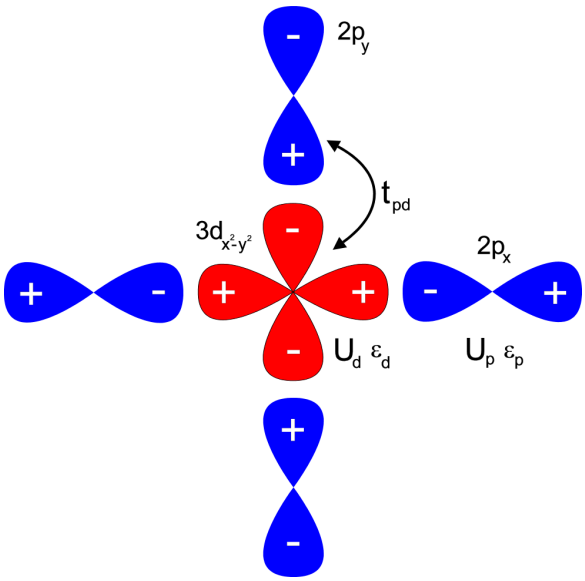

Figure 8: Schematic picture of the CuO_2–planes in high–temperature superconductors.

Perturbation theory, similarly to that outlined in Section 3.1.1 leads to the effective Hamiltonian

$$\mathcal{H}_{eff} = \sum_{i,j,\sigma,\sigma'} J_{pd} \left(-1\right)^{1-\sigma-\sigma'} p_i^{\sigma,\sigma'} X_j^{\bar{\sigma},\bar{\sigma}'}, \tag{25}$$

where $J_{pd} \simeq t_{pd}^2 / \left(U - \varepsilon_p + \varepsilon_d\right)$.

The diagonalization of this Hamiltonian is covered in [27]. The corresponding quasiparticle operator is

$$\psi_i^{pd,\uparrow} = \frac{1}{\sqrt{2}} \left(X_i^{\uparrow,\uparrow} p_i^{\downarrow} - X_i^{\uparrow,\downarrow} p_i^{\uparrow} \right), \tag{26}$$

where p_i is a combination of the four oxygen states around the copper with the same symmetry as the copper site, i.e. $x^2 - y^2$ (see Figure 8). The physical meaning of this operator is that the carriers (holes) move over the four oxygen sites, but they can form singlet copper–oxygen combinations at the copper site for a short time. The index pd refers to this Zhang–Rice

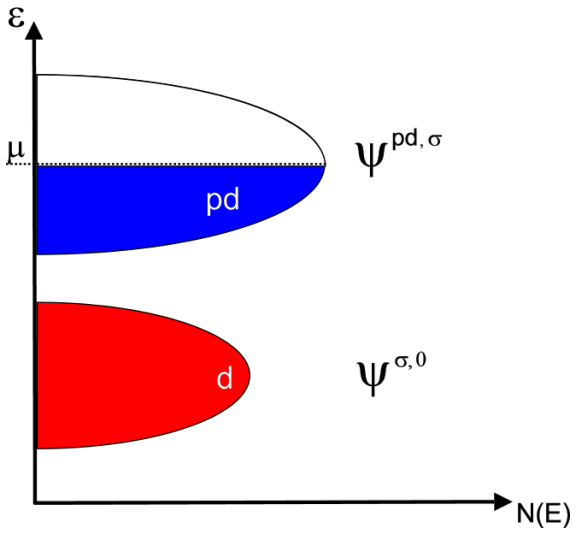

Figure 9: Schematic band picture in the copper–oxygen band model. The red one has a copper LHB character, whereas the blue one is a copper–oxygen singlet–correlated band.

singlet formation. In the singlet combination one spin belongs to the copper and the other to the oxygen combination with the same symmetry as the copper. The spectral weight of the singlet–correlated band changes with doping as $f = 2\delta/(1+\delta)$. This means that, contrary to the normal Fermi picture, the half filling regime is already reached at $\delta = 1/3$. Figure 9 shows the band picture along with the corresponding quasiparticle operators. For the operators $\psi_i^{pd,\sigma}$ the following expressions hold:

$$\begin{aligned} \psi^{0,0} + \psi^{\uparrow,\uparrow} + \psi^{\downarrow,\downarrow} + \psi^{pd,pd} &= 1 \\ \psi^{\uparrow,\uparrow} + \psi^{\downarrow,\downarrow} + 2\psi^{pd,pd} &= 1+\delta \\ \psi^{\uparrow,\uparrow} - \psi^{\downarrow,\downarrow} &= 2S^z \\ \psi^{\uparrow,\uparrow} + \psi^{\downarrow,\downarrow} &= n. \end{aligned} \tag{27}$$

We recognize these relations, as they are very similar to the equations for the Hubbard X–operators covered in Section 3.1.2 on page 15. Most importantly,

the anticommutators are similarly related to the doping level δ and spin S^z as

$$\begin{aligned} \left\{\psi^{pd,\sigma}, \psi^{\sigma,pd}\right\} &= \frac{1+\delta}{2} + 2\sigma S^z = P + 2\sigma S^z \\ \left\{\psi^{\sigma,0}, \psi^{0,\sigma}\right\} &= \frac{1-\delta}{2} + 2\sigma S^z = P - \delta + 2\sigma S^z. \end{aligned} \tag{28}$$

Note: we will refer to the factor $(1+\delta)/2$ as P in later discussions.

Since the commutator algebra is different from that valid in the weak coupling conventional Fermi liquid scenario, the expression for the spin susceptibility will be quite different from the Pauli–Lindhard formula. The starting point for our calculations will be a similar effective t-J Hamiltonian as in the original Zhang–Rice paper [88]. However, instead of making an additional electron–hole transformation, we will keep the hole picture. Our Hamiltonian is given as

$$\mathcal{H} = \sum_{i,j,\sigma} t_{ij} \psi_i^{pd,\sigma} \psi_j^{\sigma,pd} + \sum_{i,j} J_{ij} \left[(\mathbf{S}_i \mathbf{S}_j) - \frac{n_i n_j}{4} \right] + \sum_{i,j} G_{ij} \delta_i \delta_j, \tag{29}$$

where J_{ij} is the superexchange parameter of the copper spins (this coupling originates from the virtual hopping from LHB to UHB via the oxygen state). G_{ij} is an effective density–density interaction parameter. This parameter allows to account for the screened Coulomb repulsion and phonon (or plasmon) mediated interactions as well. Furthermore $\psi_i^{pd,\sigma}\left(\psi_i^{\sigma,pd}\right)$ are the composite copper–oxygen creation (annihilation) operators of the copper–oxygen singlet states in the plane. Consequently, the first term describes the quasiparticle hopping between unit cells. The last term is a Coulomb–like interaction between doped holes, which can be usually neglected, because it does not contribute to the spin susceptibility. In the next chapters we will calculate the spin susceptibility in the framework of this new "singlet–correlated band" model. As the first step to these calculations, we consider the dynamic susceptibility in the standard BCS theory.

3.3 Spin susceptibility in the BCS theory

In preparation for later calculations and discussions it is of interest to consider the spin susceptibility in the framework of the generalized BCS theory. This expression for the susceptibility was previously used by various authors [16, 50] to describe the behavior of high–T_c superconductors within the random–phase approximation scheme. To distinguish the BCS approach from Hubbard models we use in this subsection the notation $a^\dagger_{\mathbf{k},\sigma}$ ($a_{\mathbf{k},\sigma}$) for the creation (annihilation) operators of electrons.

The BCS pairing Hamiltonian is given by

$$\mathcal{H} = \sum_{\mathbf{k},\sigma} (\varepsilon_{\mathbf{k}} - \mu)\, a^\dagger_{\mathbf{k},\sigma} a_{\mathbf{k},\sigma} - V \sum_{\mathbf{k},\mathbf{k}'} a^\dagger_{\mathbf{k}',\uparrow} a^\dagger_{-\mathbf{k}',\downarrow} a_{-\mathbf{k},\downarrow} a_{\mathbf{k},\uparrow}, \tag{30}$$

where the first term describes a free electron gas and the second term is an attractive interaction between electrons with opposite spin and momentum. The chemical potential is introduced to fix the expectation value of the particle number. To decouple the interaction term we replace (30) with an effective Hamiltonian

$$\mathcal{H} = \sum_{\mathbf{k},\sigma} (\varepsilon_{\mathbf{k}} - \mu)\, a^\dagger_{\mathbf{k},\sigma} a_{\mathbf{k},\sigma} - \sum_{\mathbf{k}} \left(\Delta a^\dagger_{\mathbf{k},\uparrow} a^\dagger_{-\mathbf{k},\downarrow} + \Delta^* a_{-\mathbf{k},\downarrow} a_{\mathbf{k},\uparrow} \right), \tag{31}$$

where

$$\Delta = -V \sum_{\mathbf{k}'} \langle a_{-\mathbf{k}',\downarrow} a_{\mathbf{k}',\uparrow} \rangle \tag{32}$$

is the gap in the energy spectrum. This Hamiltonian can be diagonalized by Bogoliubov's transformation

$$\begin{aligned} a_{\mathbf{k},\uparrow} &= u_{\mathbf{k}} \alpha_{\mathbf{k},\uparrow} + v_{\mathbf{k}} \alpha^\dagger_{-\mathbf{k},\downarrow} \\ a_{\mathbf{k},\downarrow} &= u_{\mathbf{k}} \alpha_{\mathbf{k},\downarrow} - v_{\mathbf{k}} \alpha^\dagger_{-\mathbf{k},\uparrow}. \end{aligned}$$

The coefficients must obey the relation $|u_{\mathbf{k}}|^2 + |v_{\mathbf{k}}|^2 = 1$ for the transformation to be canonical. They are given by

$$\begin{aligned} u^2_{\mathbf{k}} &= \frac{1}{2}\left[1 + \frac{\varepsilon_{\mathbf{k}} - \mu}{E_{\mathbf{k}}}\right] \\ v^2_{\mathbf{k}} &= \frac{1}{2}\left[1 - \frac{\varepsilon_{\mathbf{k}} - \mu}{E_{\mathbf{k}}}\right], \end{aligned}$$

where we define $E_{\mathbf{k}} = \sqrt{(\varepsilon_{\mathbf{k}} - \mu)^2 + |\Delta|^2}$. The resulting Hamiltonian takes the form

$$\mathcal{H} = \sum_{\mathbf{k}} \left((\varepsilon_{\mathbf{k}} - \mu) - E_{\mathbf{k}} \right) + \sum_{\mathbf{k},\sigma} E_{\mathbf{k}} \alpha^{\dagger}_{\mathbf{k},\sigma} \alpha_{\mathbf{k},\sigma}. \tag{33}$$

The first term is a constant energy shift and the second term describes the quasiparticle excitations with energy $E_{\mathbf{k}}$. The form of the new quasiparticle energy implies a gap Δ in the energy spectrum. The new operators obey the canonical anticommutator relations $\left\{ \alpha_{\mathbf{k}}, \alpha^{\dagger}_{\mathbf{k}'} \right\} = \delta_{\mathbf{k},\mathbf{k}'}$, $\{\alpha_{\mathbf{k}}, \alpha_{\mathbf{k}'}\} = 0$. Equation (32) for the energy gap can be expressed as

$$\Delta = V \sum_{\mathbf{k}'} \frac{\Delta_{\mathbf{k}'}}{E_{\mathbf{k}'}} \tanh\left(\beta E_{\mathbf{k}'}\right). \tag{34}$$

This expression is referred to as "gap function". It agrees with the result originally obtained by Bardeen, Cooper and Schrieffer.

To derive the susceptibility we use the Hamiltonian (33) in Bogoliubov's form and utilize the Green's function method

$$\chi_0^{+-}(\mathbf{q}, \omega) = -2\pi i \left\langle \left\langle S^{+}_{\mathbf{q}} \left| S^{-}_{-\mathbf{q}} \right\rangle \right\rangle \right., \tag{35}$$

where $S^{+}_{\mathbf{q}}$ and $S^{-}_{-\mathbf{q}}$ are the usual spin density operators given by

$$S^{+}_{\mathbf{q}} = \sum_{\mathbf{k}} a^{\dagger}_{\mathbf{k}+\mathbf{q},\downarrow} a_{\mathbf{k},\uparrow} \qquad S^{-}_{-\mathbf{q}} = \sum_{\mathbf{k}} a^{\dagger}_{\mathbf{k}+\mathbf{q},\uparrow} a_{\mathbf{k},\downarrow}.$$

Using Bogoliubov's quasiparticle operators we can express these pairs of operators as

$$\begin{aligned} a^{\dagger}_{\mathbf{k}+\mathbf{q},\uparrow} a_{\mathbf{k},\downarrow} &= u_{\mathbf{k}+\mathbf{q}} u_{\mathbf{k}} \alpha^{\dagger}_{\mathbf{k}+\mathbf{q},\uparrow} \alpha_{\mathbf{k},\downarrow} + v_{\mathbf{k}+\mathbf{q}} u_{\mathbf{k}} \alpha_{-\mathbf{k}-\mathbf{q},\downarrow} \alpha_{\mathbf{k},\downarrow} \\ &- u_{\mathbf{k}+\mathbf{q}} v_{\mathbf{k}} \alpha^{\dagger}_{\mathbf{k}+\mathbf{q},\uparrow} \alpha^{\dagger}_{-\mathbf{k},\uparrow} - v_{\mathbf{k}+\mathbf{q}} v_{\mathbf{k}} \alpha_{-\mathbf{k}-\mathbf{q},\downarrow} \alpha^{\dagger}_{-\mathbf{k},\uparrow}. \end{aligned} \tag{36}$$

The equation of motion for the Green's function using the notation of Nolting [61] is written as follows

$$(\omega + i\Gamma) \left\langle \left\langle S^{+}_{\mathbf{q}} \left| S^{-}_{-\mathbf{q}} \right\rangle \right\rangle \right. = \frac{i}{2\pi} \left\langle \left[S^{+}_{\mathbf{q}}, S^{-}_{-\mathbf{q}} \right] \right\rangle + \left\langle \left\langle \left[S^{+}_{\mathbf{q}}, \mathcal{H} \right] \left| S^{-}_{-\mathbf{q}} \right\rangle \right\rangle \right., \tag{37}$$

where Γ is an artificially introduced damping factor that will characterize the lifetime of the quasiparticles. We can calculate the susceptibility from the equation of motion, utilizing equation (36) and remembering the anti-commutator relations of Bogoliubov's operators. It is given by

$$\begin{aligned}
\chi_0^{+-}(\mathbf{q},\omega) &= \frac{1}{N}\sum_{\mathbf{k}} \left(x_{\mathbf{k}}x_{\mathbf{k+q}} + z_{\mathbf{k}}z_{\mathbf{k+q}}\right) \frac{f_{\mathbf{k+q}} - f_{\mathbf{k}}}{\omega + i\Gamma + E_{\mathbf{k}} - E_{\mathbf{k+q}}} \\
&+ \frac{1}{N}\sum_{\mathbf{k}} \left(y_{\mathbf{k}}y_{\mathbf{k+q}} + z_{\mathbf{k}}z_{\mathbf{k+q}}\right) \frac{f_{-\mathbf{k}} - f_{-\mathbf{k-q}}}{\omega + i\Gamma - E_{-\mathbf{k}} + E_{-\mathbf{k-q}}} \\
&+ \frac{1}{N}\sum_{\mathbf{k}} \left(x_{\mathbf{k}}y_{\mathbf{k+q}} - z_{\mathbf{k}}z_{\mathbf{k+q}}\right) \frac{1 - f_{\mathbf{k}} - f_{-\mathbf{k-q}}}{\omega + i\Gamma + E_{-\mathbf{k}} + E_{-\mathbf{k-q}}} \\
&+ \frac{1}{N}\sum_{\mathbf{k}} \left(y_{\mathbf{k}}x_{\mathbf{k+q}} - z_{\mathbf{k}}z_{\mathbf{k+q}}\right) \frac{f_{-\mathbf{k}} + f_{\mathbf{k+q}} - 1}{\omega + i\Gamma - E_{-\mathbf{k}} - E_{\mathbf{k+q}}},
\end{aligned} \tag{38}$$

where $x_{\mathbf{k}} = u_{\mathbf{k}}^2$, $y_{\mathbf{k}} = v_{\mathbf{k}}^2$ and $z_{\mathbf{k}} = u_{\mathbf{k}}v_{\mathbf{k}}$. For the case $E_{\mathbf{k}} = E_{-\mathbf{k}}$ (i.e. taking into account the crystal symmetry) this expression agrees with that published previously by Bulut and Scalapino [13]. In their work they considered the susceptibility in the random–phase approximation (RPA) form

$$\chi\left(\mathbf{q},\omega\right) = \frac{\chi_0\left(\mathbf{q},\omega\right)}{1 - U_e\chi_0\left(\mathbf{q},\omega\right)}, \tag{39}$$

where $\chi_0\left(\mathbf{q},\omega\right)$ is the BCS susceptibility $\chi_0^{+-}(\mathbf{q},\omega)$ according to equation (38) and U_e is an effective interaction parameter. We will use this expression in Section 5 to study the possible pairing symmetries in high–T_c superconductors. Also note that the BCS susceptibility $\chi_0\left(\mathbf{q},\omega\right)$ appears in the susceptibility expression for the singlet–correlated band model in Section 3.4.4. For more information on the BCS susceptibility and the BCS theory see the textbook of Schrieffer [71].

3.4 Spin susceptibility in the singlet–correlated band model

In this section we turn our attention to the susceptibility in the singlet–correlated band model. In particular, we discuss the equation of motion for the composite operators as well as the gap function and the possible gap symmetries. Finally, we present the new analytical expression for the spin susceptibility in the framework of the singlet–correlated band model.

3.4.1 Equations of motion for composite operators

To linearize the equation of motion, we use the decoupling scheme introduced by Roth [49]. This method has been studied in numerous works and the quality of the approximation has been confirmed to be good by comparison with exact diagonalization methods [6]. The method consists of seeking the set of operators A_n, that are the most relevant for the excitations of the given system. Further it is assumed that the commutator can be written as

$$[A_n, \mathcal{H}] = \sum_m K_{mn} A_n. \tag{40}$$

Then the problem is reduced to finding the coefficients K_{mn} for a given Hamiltonian $\mathcal{H}$. This can be solved by building the anticommutators on both sides of equation (40) with each operator A_n and then taking the thermal average. In this way a set of linear equations is obtained and the coefficients K_{mn} can be extracted. In our case we take

$$\begin{aligned} i\hbar\frac{\partial\psi_l^{\uparrow,pd}}{\partial t} &= \left[\psi_l^{\uparrow,pd}, \mathcal{H}\right] \\ &= \sum_j t_{il}\left[\left(\psi_l^{\uparrow,\uparrow} + \psi_l^{pd,pd}\right)\psi_j^{\uparrow,pd} + \psi_l^{\uparrow,\downarrow}\psi_j^{\downarrow,pd}\right] \\ &+ \frac{1}{2}\sum_j J_{lj}\left(\psi_l^{\uparrow,pd}\psi_j^{\downarrow,\downarrow} - \psi_l^{\downarrow,pd}\psi_j^{\uparrow,\downarrow}\right) + \frac{1}{2}\sum_j G_{lj}\psi_l^{\uparrow,pd}\psi_j^{pd,pd} \\ &= \sum_m C_{lm}\psi_m^{\uparrow,pd} + \sum_m \Delta_{lm}\psi_m^{pd,\downarrow} \end{aligned} \tag{41}$$

where the second term will give us the energy gap. Now we build our anticommutators according to the decoupling scheme. Utilizing equation (28) on page 22 they can be obtained as

$$\begin{aligned}\left\langle\left\{\left[\psi_l^{\uparrow,pd},\mathcal{H}\right],\psi_j^{pd,\uparrow}\right\}\right\rangle &= C_{lj}\left\langle\left\{\psi_j^{\uparrow,pd},\psi_j^{pd,\uparrow}\right\}\right\rangle \\ &= PC_{lj} \\ \left\langle\left\{\left[\psi_l^{\uparrow,pd},\mathcal{H}\right],\psi_j^{\downarrow,pd}\right\}\right\rangle &= P\Delta_{lj}.\end{aligned} \tag{42}$$

We can then calculate these coefficients with the help of the commutator algebra and the relations given in Section 3.2.2 on page 18. They are calculated as

$$\begin{aligned}C_{lj} &= \frac{1}{P}t_{lj}\left[P^2+(\mathbf{S}_l\mathbf{S}_j)\right]-\frac{1}{2P}\left(J_{jl}+G_{jl}\right)\left\langle\psi_j^{pd,\uparrow}\psi_l^{\uparrow,pd}\right\rangle \\ \Delta_{lj} &= \frac{1}{2P}\left(2J_{lj}-G_{lj}\right)\left\langle\psi_j^{\uparrow,pd}\psi_l^{\downarrow,pd}\right\rangle.\end{aligned} \tag{43}$$

Fourier transformation of equation (41) yields

$$i\hbar\frac{\partial\psi_{\mathbf{k}}^{\uparrow,pd}}{\partial t}=\varepsilon_{\mathbf{k}}\psi_{\mathbf{k}}^{\uparrow,pd}+\Delta_{\mathbf{k}}\psi_{-\mathbf{k}}^{\downarrow,pd} \tag{44}$$

where

$$\Delta_{\mathbf{k}}=\frac{1}{2P}\sum_{\mathbf{k}'}\left(2J_{\mathbf{k}-\mathbf{k}'}-G_{\mathbf{k}-\mathbf{k}'}\right)\left\langle\psi_{\mathbf{k}'}^{\uparrow,pd}\psi_{-\mathbf{k}'}^{\downarrow,pd}\right\rangle \tag{45}$$

is obtained for the gap. The function $\varepsilon_{\mathbf{k}}$ is calculated as

$$\begin{aligned}\varepsilon_{\mathbf{k}} &= \sum_j t_{ij}\left(P+\frac{1}{P}\left\langle S_i^+S_j^-+S_i^zS_j^z\right\rangle\right)e^{-ikR_{ij}} \\ &- \sum_{\mathbf{k}'}\frac{1}{2P}\left(J_{\mathbf{k}'-\mathbf{k}}+G_{\mathbf{k}'-\mathbf{k}}\right)\left\langle\psi_{\mathbf{k}'}^{pd,\downarrow}\psi_{\mathbf{k}'}^{\downarrow,pd}\right\rangle.\end{aligned} \tag{46}$$

3.4.2 The gap equation

In this section we consider equation (45). With the help of the relation $\left\langle \alpha^{\dagger}_{\mathbf{k}\uparrow}\alpha_{\mathbf{k}\uparrow}\right\rangle = Pf(E_{\mathbf{k}})$ (the number of quasiparticles) we are able to rewrite this equation, utilizing Bogoliubov's quasiparticle operators in the following form

$$\begin{aligned}\left\langle \psi^{\uparrow,pd}_{\mathbf{k}'}\psi^{\downarrow,pd}_{-\mathbf{k}'}\right\rangle &= \left\langle \left(u_{\mathbf{k}}\alpha_{\mathbf{k}\uparrow} - v_{\mathbf{k}}\alpha^{\dagger}_{-\mathbf{k}\downarrow}\right)\left(u_{\mathbf{k}}\alpha_{-\mathbf{k}\downarrow} + v_{\mathbf{k}}\alpha^{\dagger}_{\mathbf{k}\uparrow}\right)\right\rangle \\ &= -v_{\mathbf{k}}u_{\mathbf{k}}Pf(E_{\mathbf{k}}) + u_{\mathbf{k}}v_{\mathbf{k}}P\left(1-f(E_{\mathbf{k}})\right) \\ &= P\frac{\Delta_{\mathbf{k}}}{2E_{\mathbf{k}}}\tanh\left(\beta\frac{E_{\mathbf{k}}}{2}\right).\end{aligned}$$

The gap equation becomes

$$\Delta_{\mathbf{k}} = \frac{1}{2}\sum_{\mathbf{k}'}\left(2J_{\mathbf{k}-\mathbf{k}'} - G_{\mathbf{k}-\mathbf{k}'}\right)\frac{\Delta_{\mathbf{k}'}}{2E_{\mathbf{k}'}}\tanh\left(\beta\frac{E_{\mathbf{k}'}}{2}\right). \tag{47}$$

This equation can be solved self–consistently by putting

$$E_{\mathbf{k}} = \sqrt{\left(\varepsilon_{\mathbf{k}} - \mu\right)^2 + \Delta^2_{\mathbf{k}}}.$$

The character of the solution of equation (47) strongly depends on the details of the Fourier transformed interaction $(2J_{\mathbf{k}-\mathbf{k}'} - G_{\mathbf{k}-\mathbf{k}'})$. The origin of this interaction, which causes the pairing in cuprates is still under debate. However, for all possible variants the temperature dependence can be approximated well by

$$\Delta(T) = \frac{\Delta_0}{2}\tanh\left(\alpha\sqrt{T_c/T - 1}\right), \tag{48}$$

with Δ_0 and α as parameters. Figure 10 shows a typical temperature dependence of the superconducting gap function.

Next we will discuss the possible gap symmetries of high-T_c superconductors. A good review on this topic is found in [83]. Since the discovery of the cuprate superconductors the pairing symmetry and mechanism was under discussion. Recently, experimental evidence pointed toward an unconventional pairing

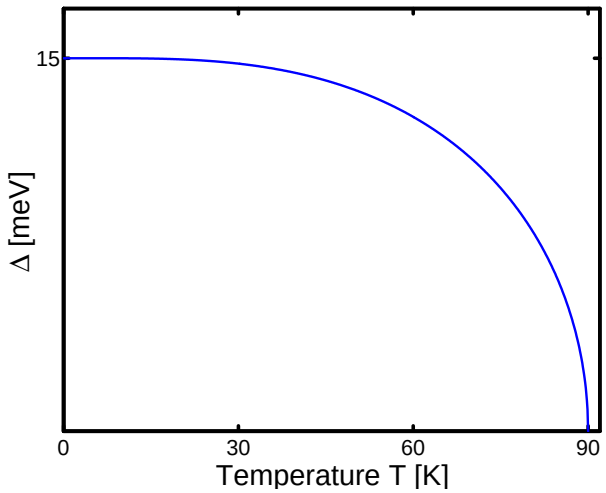

Figure 10: Temperature dependence of the superconducting gap.

state. The electronically active elements in cuprates, the tetragonal CuO_2–planes belong to the crystal point group $C_{4\nu}$. This indicates a fourfold axis of symmetry and three mirror planes. The symmetries of this structure will be reflected in the pair correlation function and the gap function. Possible pairing symmetries according to group theory are

$$\Delta_{\mathbf{k}} = \Delta_0 \tag{49}$$

$$\Delta_{\mathbf{k}} = \frac{\Delta_0}{2}\left(\cos k_x + \cos k_y\right) \tag{50}$$

$$\Delta_{\mathbf{k}} = \frac{\Delta_0}{2}\left(\cos k_x - \cos k_y\right) \tag{51}$$

$$\Delta_{\mathbf{k}} = \frac{\Delta_0}{2}\left(\sin k_x \sin k_y\right). \tag{52}$$

The first gap function is similar to the one in the original BCS theory. It is constant on the whole Brillouin zone and is denoted as "conventional s–wave gap". The second function is also constant under all possible symmetry transformations of the Brillouin zone, it is usually referred to as "extended s–wave". The last two functions exhibit unconventional symmetry, they change sign under $\pi/2$ rotations on the Brillouin zone. These are called "d–wave functions", because they have the same symmetry as an atomic spherical

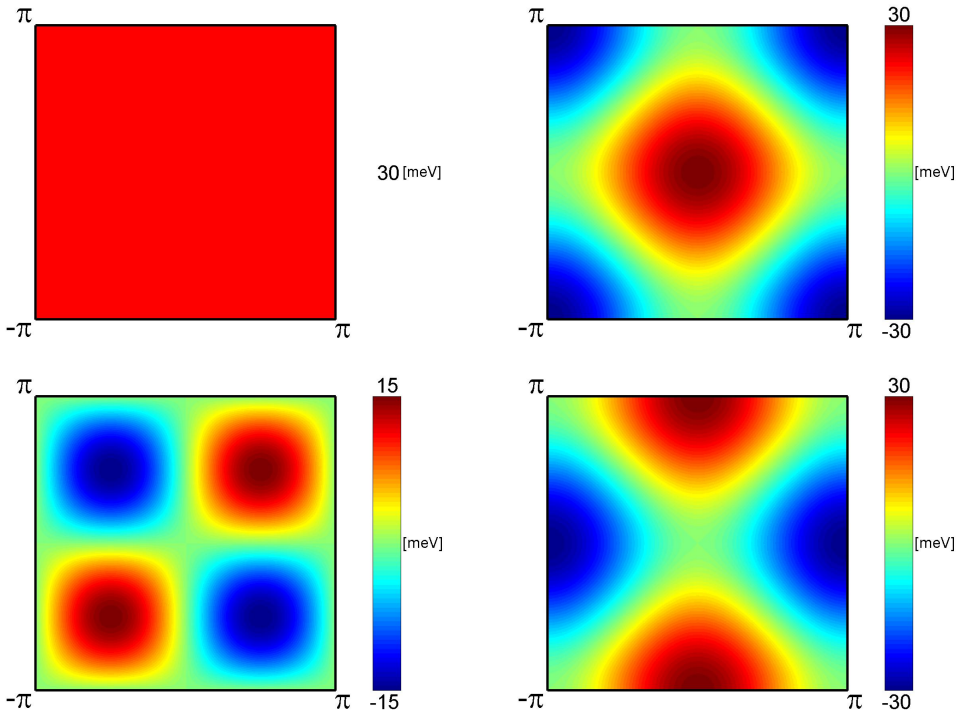

Figure 11: Possible gap functions in cuprate superconductors on the Brillouin zone at $T = 0$ K. The gap parameter is chosen to be $\Delta_0 = 30$ meV. The conventional s–wave gap function (top left) is a constant, the extended s–wave gap (top right) is constant under all symmetry operations and the d_{xy}–wave (lower left), $d_{x^2-y^2}$–wave gaps (lower right) change sign under 90°–rotation.

$d_{x^2-y^2}$ /d_{xy} wave. Figure 11 shows these four functions on the first Brillouin zone.

3.4.3 Chemical potential

If the lower Hubbard band is completely filled, the chemical potential can be determined by the number of quasiparticles in the upper Hubbard band (pd–band). The following equation holds (using relations (27) on page 21)

$$\frac{1}{2N}\sum_i \left(\psi_i^{pd,\uparrow}\psi_i^{\uparrow,pd} + \psi_i^{pd,\downarrow}\psi_i^{\downarrow,pd}\right) = \delta. \tag{53}$$

Fourier transformation results in

$$\frac{1}{2N}\sum_{\mathbf{k}}\left(\psi_{\mathbf{k}}^{pd,\uparrow}\psi_{\mathbf{k}}^{\uparrow,pd}+\psi_{\mathbf{k}}^{pd,\downarrow}\psi_{\mathbf{k}}^{\downarrow,pd}\right)=\delta. \tag{54}$$

Bogoliubov's transformation finally gives us

$$\frac{P}{N}\sum_{\mathbf{k}}\left\{\left(u_{\mathbf{k}}^2-v_{\mathbf{k}}^2\right)f(E_{\mathbf{k}})+v_{\mathbf{k}}^2\right\}=\delta. \tag{55}$$

The chemical potential can be determined self–consistently from this equation. In our calculations we will usually assume optimal doping, that is a half filled pd–band with $\delta \simeq 1/3$.

3.4.4 Spin susceptibility

The susceptibility in the singlet–correlated band model can be calculated from the expression

$$\chi^{+-}(\mathbf{q},\omega)=-2\pi i\left\langle\left\langle S_{\mathbf{q}}^{+}\left|S_{-\mathbf{q}}^{-}\right.\right\rangle\right\rangle,$$

where $S_{\mathbf{q}}^{+}$, $S_{-\mathbf{q}}^{-}$ are the spin density operators given by

$$S_{\mathbf{q}}^{+}=\sum_{\mathbf{k}}\psi_{\mathbf{k}+\mathbf{q}}^{\uparrow,pd}\psi_{\mathbf{k}}^{pd,\downarrow}\qquad S_{-\mathbf{q}}^{-}=\sum_{\mathbf{k}}\psi_{\mathbf{k}+\mathbf{q}}^{\downarrow,pd}\psi_{\mathbf{k}}^{pd,\uparrow}. \tag{56}$$

The susceptibility is derived by the following procedure. First, we write down a complete set of equations of motion using the composite copper–oxygen creation (annihilation) operators $\psi_i^{pd,\sigma}\left(\psi_i^{\sigma,pd}\right)$ of the copper–oxygen singlet states in the plane. Then, by means of a linear transformation we rearrange these equations via Bogoliubov's quasiparticle operators into new sets of equations, which finally will be solved. An expression for susceptibility was previously derived [22] by utilizing the method of Heisenberg equation of motion in a small magnetic field. The advantage of the Green's function method is that it allows to obtain a formula for the susceptibility which contains both the itinerant (or quasi Fermi–liquid) part and the local spin fluctuation part in one general expression. Details of this calculation are presented in Appendix A. The expression for the susceptibility is given as

$$\chi(\mathbf{q},\omega) = \frac{\chi_0(\mathbf{q},\omega)}{1 + J_{\mathbf{q}}\chi_0(\mathbf{q},\omega) + \Pi(\mathbf{q},\omega) + Z(\mathbf{q},\omega)}, \tag{57}$$

where the superexchange interaction between the copper spins is

$$J_{\mathbf{q}} = J_1 \left(\cos q_x + \cos q_y\right).$$

The functions $\chi_0(\mathbf{q},\omega)$, $\Pi(\mathbf{q},\omega)$ and $Z(\mathbf{q},\omega)$ are given as follows

$$\begin{aligned}
\chi_0(\mathbf{q},\omega) &= \frac{P}{N}\sum_{\mathbf{k}} \left(x_{\mathbf{k}}x_{\mathbf{k+q}} + y_{\mathbf{k}}y_{\mathbf{k+q}} + 2z_{\mathbf{k}}z_{\mathbf{k+q}}\right) \frac{f_{\mathbf{k+q}} - f_{\mathbf{k}}}{\omega + i\Gamma + E_{\mathbf{k}} - E_{\mathbf{k+q}}} \\
&+ \frac{P}{N}\sum_{\mathbf{k}} \left(x_{\mathbf{k}}y_{\mathbf{k+q}} - z_{\mathbf{k}}z_{\mathbf{k+q}}\right) \frac{1 - f_{\mathbf{k}} - f_{\mathbf{k+q}}}{\omega + i\Gamma + E_{\mathbf{k}} + E_{\mathbf{k+q}}} \\
&+ \frac{P}{N}\sum_{\mathbf{k}} \left(y_{\mathbf{k}}x_{\mathbf{k+q}} - z_{\mathbf{k}}z_{\mathbf{k+q}}\right) \frac{f_{\mathbf{k}} + f_{\mathbf{k+q}} - 1}{\omega + i\Gamma - E_{\mathbf{k}} - E_{\mathbf{k+q}}},
\end{aligned} \tag{58}$$

$$\begin{aligned}
\Pi(\mathbf{q},\omega) &= \frac{P}{N}\sum_{\mathbf{k}} \left(x_{\mathbf{k}}x_{\mathbf{k+q}} + z_{\mathbf{k}}z_{\mathbf{k+q}}\right) \frac{t_{\mathbf{k}}f_{\mathbf{k}} - t_{\mathbf{k+q}}f_{\mathbf{k+q}}}{\omega + i\Gamma + E_{\mathbf{k}} - E_{\mathbf{k+q}}} \\
&+ \frac{P}{N}\sum_{\mathbf{k}} \left(y_{\mathbf{k}}y_{\mathbf{k+q}} + z_{\mathbf{k}}z_{\mathbf{k+q}}\right) \frac{t_{\mathbf{k}}\left(1 - f_{\mathbf{k}}\right) - t_{\mathbf{k+q}}\left(1 - f_{\mathbf{k+q}}\right)}{\omega + i\Gamma - E_{\mathbf{k}} + E_{\mathbf{k+q}}} \\
&+ \frac{P}{N}\sum_{\mathbf{k}} \left(x_{\mathbf{k}}y_{\mathbf{k+q}} - z_{\mathbf{k}}z_{\mathbf{k+q}}\right) \frac{t_{\mathbf{k}}f_{\mathbf{k}} - t_{\mathbf{k+q}}\left(1 - f_{\mathbf{k+q}}\right)}{\omega + i\Gamma + E_{\mathbf{k}} + E_{\mathbf{k+q}}} \\
&+ \frac{P}{N}\sum_{\mathbf{k}} \left(y_{\mathbf{k}}x_{\mathbf{k+q}} - z_{\mathbf{k}}z_{\mathbf{k+q}}\right) \frac{t_{\mathbf{k}}\left(1 - f_{\mathbf{k}}\right) - t_{\mathbf{k+q}}f_{\mathbf{k+q}}}{\omega + i\Gamma - E_{\mathbf{k}} - E_{\mathbf{k+q}}},
\end{aligned} \tag{59}$$

and

$$\begin{aligned}
Z(\mathbf{q},\omega) &= \frac{1}{N}\sum_{\mathbf{k}} \left(Px_{\mathbf{k}}x_{\mathbf{k+q}} + (P-1)z_{\mathbf{k}}z_{\mathbf{k+q}}\right) \frac{\omega + i\Gamma}{\omega + i\Gamma + E_{\mathbf{k}} - E_{\mathbf{k+q}}} \\
&+ \frac{1}{N}\sum_{\mathbf{k}} \left(Py_{\mathbf{k}}y_{\mathbf{k+q}} + (P-1)z_{\mathbf{k}}z_{\mathbf{k+q}}\right) \frac{\omega + i\Gamma}{\omega + i\Gamma - E_{\mathbf{k}} + E_{\mathbf{k+q}}}
\end{aligned} \tag{60}$$

$$+ \quad \frac{1}{N}\sum_{\mathbf{k}} \left(P x_{\mathbf{k}} y_{\mathbf{k+q}} - (P-1) z_{\mathbf{k}} z_{\mathbf{k+q}}\right) \frac{\omega + i\Gamma}{\omega + i\Gamma + E_{\mathbf{k}} + E_{\mathbf{k+q}}}$$

$$+ \quad \frac{1}{N}\sum_{\mathbf{k}} \left(P y_{\mathbf{k}} x_{\mathbf{k+q}} - (P-1) z_{\mathbf{k}} z_{\mathbf{k+q}}\right) \frac{\omega + i\Gamma}{\omega + i\Gamma - E_{\mathbf{k}} - E_{\mathbf{k+q}}}.$$

Here we introduced

$$\begin{aligned} x_{\mathbf{k}} = u_{\mathbf{k}}^2 &= \frac{1}{2}\left(1 + \frac{\varepsilon_{\mathbf{k}}}{E_{\mathbf{k}}}\right) \\ y_{\mathbf{k}} = v_{\mathbf{k}}^2 &= \frac{1}{2}\left(1 - \frac{\varepsilon_{\mathbf{k}}}{E_{\mathbf{k}}}\right) \\ z_{\mathbf{k}} = u_{\mathbf{k}} v_{\mathbf{k}} &= \frac{\Delta_{\mathbf{k}}}{2E_{\mathbf{k}}}, \end{aligned} \tag{61}$$

for the sake of shortness. The functions $x_{\mathbf{k}}$, $y_{\mathbf{k}}$ and $z_{\mathbf{k}}$ are the same coherence factors as in the BCS theory. Furthermore $E_{\mathbf{k}} = \sqrt{(\varepsilon_{\mathbf{k}} - \mu)^2 - \Delta_{\mathbf{k}}^2}$ is the energy of Bogoliubov's quasiparticles in the superconducting state.

The first term in our formula $\chi_0(\mathbf{q}, \omega)$ agrees with that previously obtained in the BCS theory (equation (38)). However, as expected, different correction functions $\Pi(\mathbf{q}, \omega)$ and $Z(\mathbf{q}, \omega)$ appear in our formula, which both have a wave–vector and frequency dependence. These functions do not arise in the conventional Fermi liquid scenario. The function $\Pi(\mathbf{q}, \omega)$ originates from the new anticommutator rule (equation (28)), whereas the function $Z(\mathbf{q}, \omega)$ has its origin in the fast fluctuations of the local spins. Also, it is important, that every factor depends on the doping level δ. With the dynamical spin susceptibility several experiments regarding high–T_c superconductors can be modeled. In the next sections, we will discuss a number of different experimental techniques and their connection to the dynamical spin susceptibility $\chi(\mathbf{q}, \omega)$.

4 Experimental techniques for probing the spin susceptibility

4.1 Inelastic neutron scattering

In this section we wish to discuss the inelastic neutron scattering experimental technique and its connection to the spin susceptibility. For more detailed reviews on this topic see [31, 82] and the references therein.

Neutron scattering is a technique similar to X–ray or electron scattering. The elastic scattering produces neutron diffraction which reveals the structural properties of the sample, whereas the inelastic collisions can be used to study phonons or magnons in a crystalline material. Therefore, inelastic neutron scattering is a valuable tool for investigating magnetic fluctuations in high–temperature superconductors.

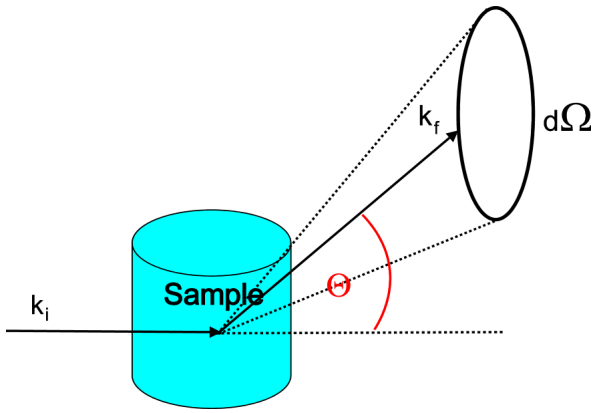

Figure 12: Illustration of neutron scattering in a solid.

Particles (neutrons) with wave vector $\mathbf{k}_i$ are scattered of a sample and are analyzed for momentum and energy both before and after scattering. This way the so–called partial differential cross section

$$\frac{d^2\sigma}{d\Omega dE_f} \tag{62}$$

can be measured. Let E_i,$\mathbf{k}_i$ (E_f,$\mathbf{k}_f$) be the energy and momentum of the

incoming (outgoing) particle. Energy and momentum conservation yields

$$\begin{aligned} E_f + \omega_{\mathbf{q}} &= E_i \\ \mathbf{k}_f + \mathbf{q} &= \mathbf{k}_i. \end{aligned} \tag{63}$$

Thus the momentum $\mathbf{q} = \mathbf{k}_i - \mathbf{k}_f$ and energy $\omega_{\mathbf{q}} = E_i - E_f$ have been transferred to the sample. The partial differential cross section can be derived with the help of Fermi's golden rule:

$$\frac{d^2\sigma}{d\Omega dE_f} = \frac{k_f}{k_i} \sum_{\lambda_i,\lambda_f} p_{\lambda_i} \left|\langle \mathbf{k}_f, \lambda_f \left|\mathbf{U}\right| \mathbf{k}_i, \lambda_i \rangle\right|^2 \delta\left(E_{\lambda_i} - E_{\lambda_f} + \hbar\omega\right), \tag{64}$$

where E_λ, $|\lambda\rangle$ are the eigenstates of the sample and p_λ is the probability of finding the system in the state $|\lambda\rangle$. $\mathbf{U}$ is the interaction operator between sample and the neutrons. The cross section provides the probability that a neutron with wave vector $\mathbf{k}_i$, after exchanging energy dE_f with the sample has wave vector $\mathbf{k}_f$ within a solid angle $d\Omega$. Figure 12 illustrates this scattering process.

Let us consider magnetic scattering. The magnetic interaction operator is given by

$$\mathbf{U} = \mu_n \mathbf{B}, \tag{65}$$

where $\mathbf{B}$ represents the magnetic field coming from the sample. Each unpaired electron moving with velocity v_e generates a field

$$\mathbf{B} = \underbrace{\nabla \times \left(\frac{\mu_e \times \mathbf{R}}{\mathbf{R}^3}\right)}_{Spin} - \underbrace{\frac{e}{c}\frac{v_e \times \mathbf{R}}{\mathbf{R}^3}}_{Orbital}, \tag{66}$$

where $\mathbf{R}$ is the position of the electron and μ_e represents its magnetic moment. Evaluation of the matrix element for the given interaction is covered in [31]. For unpolarized neutrons the cross section becomes

$$\frac{d^2\sigma}{d\Omega dE_f} = \frac{k_f}{k_i} \left(\gamma r_0 F(\mathbf{q})\right)^2 \sum_{\alpha,\beta} \left(\delta_{\alpha\beta} - Q_\alpha Q_\beta\right) S^{\alpha\beta}(\mathbf{q},\omega), \tag{67}$$

where $S(\mathbf{q},\omega)$ is the magnetic scattering function, which corresponds to the Fourier transform of the magnetic pair correlation function. It is given by

$$S^{\alpha\beta}(\mathbf{q},\omega) = \sum_{k,k'} e^{i\mathbf{q}(\mathbf{R}_k - \mathbf{R}_{k'})} \sum_{\lambda_i,\lambda_f} p_{\lambda_i} \langle \lambda_i | S^{\alpha}_{k'} | \lambda_f \rangle \left\langle \lambda_f \left| S^{\beta}_{k} \right| \lambda_i \right\rangle \delta\left(E_{\lambda_i} - E_{\lambda_f} + \hbar\omega\right). \tag{68}$$

Furthermore $F(\mathbf{q})$ is a dimensionless magnetic form factor, defined as the Fourier transform of the normalised spin density of the electrons, S^{α}_{i} ($\alpha = x, y, z$, Cartesian) is the spin operator of the i-th ion at site $\mathbf{R}_i$.

As we can see, inelastic neutron scattering allows the direct measurement of the magnetic scattering function $S(\mathbf{q},\omega)$. Most importantly, this function is related to the spin susceptibility through the fluctuation–dissipation theorem

$$S(\mathbf{q},\omega) \propto (1 - n(\omega)) Im\chi(\mathbf{q},\omega), \tag{69}$$

where $n(\omega)$ is the Boltzmann–function.

Therefore the measured susceptibility can be directly compared to our theoretical models. Magnetic inelastic neutron scattering experiments show a sharp resonance in the magnetic excitation spectrum of the optimally doped $YBa_2Cu_3O_7$ in the superconducting state, at a frequency $\omega \simeq 41$ meV, near the antiferromagnetic wave vector $\mathbf{Q}$ [8, 58]. Consequently, there should be a large peak in the imaginary part of the spin susceptibility $\chi(\mathbf{Q},\omega)$ at the same frequency.

4.2 Nuclear magnetic resonance

In this section we introduce the NMR measurement technique and its connection to the spin susceptibility. Reviews on the NMR experimental technique and its applications on high–T_c superconductors can be found in [7, 9, 69, 74].

4.2.1 NMR background

The magnetic resonance measurement technique was first applied in 1938 by Rabi to determine the magnetic moments in an atomic beam. Resonance experiments in solids were carried out by E. Zavoisky in 1944, with the help of microwave absorption. The first NMR experiments followed the year after

in the USA, conducted by different experimental groups. Today NMR is applied in many areas of science, most importantly in solid state physics.

A resonance experiment is performed by inducing magnetic dipole transitions between Zeeman energy levels. The sample is prepared in a large static magnetic field $\mathbf{H}_0$. By applying a radiofrequency field (RF), the magnetization can be turned in any direction. For example if we switch on a RF–field at the time $t = 0$ and keep it applied for the duration $t_{90^\circ} = \pi/\omega_L$, all spins will be flipped by 90°, where they precess perpendicular to $\mathbf{H}_0$. Such kind of pulse is referred to as a "90°–pulse". Similarly we can also apply a 180°–pulse, which results in the maximal energy absorption of the system. If we now turn our RF–field off, the magnetization decays back in its equilibrium state, through relaxation processes. The observation of this precession is mostly carried out by means of a coil. The induced voltage can be recorded as a function of time and will be Fourier–transformed. After the transformation we have our frequency spectrum. With this method the whole frequency spectrum can be mapped at once.

In a solid the nuclear spins are the subject of various couplings from their environment. The Hamiltonian can be written, for a nuclear spin $\mathbf{I}$ in an applied field $\mathbf{H}_0$, as follows:

$$\mathcal{H} = \mathcal{H}_{Zeeman} + \mathcal{H}_Q + \mathcal{H}_{Hf}, \tag{70}$$

here $\mathcal{H}_{Zeeman} = -\gamma_n \hbar \mathbf{H}_0 \mathbf{I}$ is the nuclear–Zeeman energy and $\mathcal{H}_Q$ denotes the coupling between the nuclear quadrupole–moment and the field gradient. Next we will consider in detail the hyperfine Hamiltonian $\mathcal{H}_{Hf}$.

The Hamilton operator, which describes the coupling between the nuclear– and electron spins, is the Mila–Rice Hamilton operator [55]. This operator describes a nuclear spin together with N electron spins coupled to it. The electron spins $\mathbf{S}_k$ at site k interact via the constant $\mathbf{A}_k$ with the nuclear spin $\mathbf{I}$, according to

$$\mathcal{H}_{Hf} = \sum_{k=1}^{N} \mathbf{A}_k \mathbf{I} \mathbf{S}_k. \tag{71}$$

Let us consider now the spin–Hamiltonian for nuclei in high–temperature superconductors. The nuclei in the CuO_2–plane are of particular interest.

For ^{63}Cu(2) in the CuO_2–plane the Hamilton operator can be expressed as

$$^{63}\mathcal{H} = {}^{63}\mathbf{I}\left[\mathbf{A}\mathbf{S}_0 + \sum_{k=1}^{4}\mathbf{B}\mathbf{S}_k\right]. \tag{72}$$

The summation with respect to k corresponds to the four nearest neighbouring (NN) Cu–nuclei. $\mathbf{A}$ stands for the coupling to the on–site electron ($d_{x^2-y^2}$ orbital). It is the sum of three parts: the dipole–part $\mathbf{A}_{dip}$, the spin–orbit part $\mathbf{A}_{so}$ and the isotropic nuclear polarisation $\mathbf{A}_{cp}$. Both $\mathbf{A}_{dip}$ and $\mathbf{A}_{so}$ are anisotropic and proportional to $\langle 1/r^3\rangle$. $\mathbf{B}$ is the isotropic coupling, which is transferred by the $Cu_{3d_{x^2-y^2}}$–O_{2p}–Cu_{4s} bands and has its origin in the four NN.

Analogously, for ^{17}O(2,3) in the CuO_2–plane we have

$$^{17}\mathcal{H} = {}^{17}\mathbf{I}\sum_{k=1}^{2}\mathbf{C}\mathbf{S}_k. \tag{73}$$

Here we only have a single anisotropic coupling $\mathbf{C}$ to the NN's. The reason is that the coupling to the next nearest neighbours (NNN) can be neglected for La_2CuO_4 as well as for $YBa_2Cu_3O_7$, see [54]. Furthermore, for ^{89}Y between two CuO_2–planes we can write

$$^{89}\mathcal{H} = {}^{89}\mathbf{I}\sum_{k=1}^{8}\mathbf{D}\mathbf{S}_k, \tag{74}$$

where the summation runs over the nearest neighbours. This coupling can be assumed isotropic. For the sake of completeness we also specify that for ^{63}Cu(1) in the CuO–chain we have

$$^{63}\mathcal{H} = {}^{63}\mathbf{I}\sum_{k=1}^{2}\mathbf{A}(1)\mathbf{S}_k, \tag{75}$$

where the k summation runs over the two Cu(2) nuclei in the neighbouring planes.

In the forthcoming sections we will discuss how we can use NMR to study and understand the behavior of the spin susceptibility $\chi(\mathbf{q},\omega)$.

4.2.2 Knight shift

W.D. Knight has found in 1949 that the resonance frequency ω_m in metals almost always exceeds ω_D in diamagnetic materials, i.e.,

$$\omega_m = \omega_D + \Delta\omega$$

holds. Furthermore, $\Delta\omega/\omega_D$ is independent of the magnetic field. In ordinary metals it is almost independent of the temperature and it increases with increasing nuclear charge. The origin of the Knight shift is the interaction between the nuclei and the spin of the conduction electrons. s–electrons have a non–vanishing probability density within the nucleus and interact with the nuclear moment. This interaction can be described by an isotropic Fermi–contact–interaction. The Hamiltonian is given as

$$\mathcal{H}_{Hf} \propto \left[-\frac{3(\mathbf{Sr})(\mathbf{Ir}) - (\mathbf{IS})r^2}{r^5} + |\psi(0)|^2 \, \mathbf{SI} \right]. \tag{76}$$

The first term in this formula represents the dipole–dipole interaction. In a strong magnetic field only the z–component S^z is non–vanishing. For the mean interaction energy we get

$$E \propto \left(-H_0 + A \left\langle S^z \right\rangle\right) I^z. \tag{77}$$

The first term originates from the interaction with the field H_0. The second term is the mean hyperfine interaction of the nucleus with the conduction electrons. A denotes the hyperfine interaction constant which can be written as

$$A \propto |\psi(0)|^2 . \tag{78}$$

In this relation $|\psi(0)|^2$ is the probability density of the electrons at the nucleus. E can be expressed as

$$E \propto -H_0 I^z \left(1 - \frac{A \left\langle S^z \right\rangle}{H_0}\right). \tag{79}$$

The Knight shift can be written as

$$K \propto \frac{A \left\langle S^z \right\rangle}{H_0} = \frac{\Delta H}{H_0} = \frac{\Delta\omega}{\omega}. \tag{80}$$

Using the spin susceptibility, we are now able to determine $\langle S^z \rangle$ as follows

$$\langle S^z \rangle = \chi(\mathbf{q} \to 0, \omega = 0) H_0. \tag{81}$$

Consequently, the Knight shift can be expressed in terms of the hyperfine coupling A and the spin susceptibility $\chi(\mathbf{q} \to 0, \omega = 0)$ as

$$K \propto A\chi(\mathbf{q} \to 0, \omega = 0). \tag{82}$$

Note that this actually refers to the spin contribution to the shift. In addition there is an orbital (chemical) shift which, however, is independent of the temperature.

Provided that we know the hyperfine coupling, the above relation implies that the Knight shift can be taken as a direct measure for the spin susceptibility $\chi(\mathbf{q} \to 0, \omega = 0)$. For a specific Hamiltonian, as described in Section 4.2.1, we obtain

$$\begin{aligned} {}^{63}K_\beta &= \frac{(A_\beta + 4B)\,\chi(\mathbf{q} \to 0, \omega = 0)}{{}^{63}\gamma_n \gamma_e \hbar^2}, \\ {}^{17}K_\beta &= \frac{2C_\beta \chi(\mathbf{q} \to 0, \omega = 0)}{{}^{17}\gamma_n \gamma_e \hbar^2}, \\ {}^{89}K &= \frac{8D\chi(\mathbf{q} \to 0, \omega = 0)}{{}^{89}\gamma_n \gamma_e \hbar^2}. \end{aligned} \tag{83}$$

Here γ_n denotes the gyromagnetic ratio of different nuclei, γ_e stands for the gyromagnetic ratio of the electron, and β is the field direction.

4.2.3 Spin–lattice relaxation rates

As we have seen in Section 4.2.2, $\chi(\mathbf{q} \to 0, \omega = 0)$ can be determined by measuring the Knight shift. The question arises how to determine the wave–vector dependence $\chi(\mathbf{q}, \omega = 0)$ of the spin susceptibility. A suitable way for investigating this dependence is to measure the spin–lattice relaxation. The nuclear spin–lattice relaxation time is the rate at which the magnetization decays into its thermal equilibrium state in an external magnetic field. This

rate originates in the fluctuations of the hyperfine field at the nucleus. For a detailed description see Section 4.2.1 on page 37. For the relation between the NMR spin–lattice relaxation T_1^{-1} and the imaginary part of the spin susceptibility $Im\chi(\mathbf{q},\omega)$ we have, according to Moriya [56]

$$ {}^{\alpha}T_{1\beta}^{-1} = \frac{k_B T}{2\mu_B^2 \hbar^2 \omega} \frac{1}{N} \sum_{\mathbf{q},\beta'} {}^{\alpha}F_{\beta'}(\mathbf{q}) Im\chi(\mathbf{q},\omega \to 0), \tag{84} $$

where β denotes the field direction, β' are the directions orthogonal to the field, N is the normalisation and α is the actual nucleus. The Fourier–transform of the spin susceptibility $\chi(\mathbf{q},\omega)$ gives us the response to an applied field of the form $\exp(i(\mathbf{qr}-\omega t))$. ${}^{\alpha}F_{\beta'}(\mathbf{q})$ is the Fourier transform of the hyperfine field.

4.2.4 Spin–spin relaxation rates

The magnetisation perpendicular to the field is the transversal magnetisation. To this corresponds a relaxation, the transverse relaxation. In most solids this relaxation rate is temperature–independent due to its dipole–dipole nature. However, in high–T_c superconductors this relaxation process is dominated by indirect relaxation due to the presence of the transferred hyperfine interaction. This relaxation process makes it possible to study the real part of the spin susceptibility $Re\chi(\mathbf{q},\omega=0)$. (For comparison, for the spin–lattice relaxation we had to deal with the imaginary part $Im\chi(\mathbf{q},\omega=0)$.) According to [81], the transverse relaxation for ^{63}Cu can be written as

$$ \left[\frac{1}{T_{2G}}\right]^2 = \frac{0.69}{128\hbar^2\mu_B^4} \left[\frac{1}{N}\sum_{\mathbf{q}} F(\mathbf{q})^2 Re\chi(\mathbf{q},\omega=0)^2 - \left(\frac{1}{N}\sum_{\mathbf{q}} F(\mathbf{q}) Re\chi(\mathbf{q},\omega=0)\right)^2\right]. \tag{85} $$

Here $Re\chi(\mathbf{q},\omega=0)$ means the real part of the susceptibility, N is the normalisation and $F(\mathbf{q})$ denotes the form factors. The factor 0.69 can be explained by the natural abundance of copper isotopes. T_{2G} is particularly important in the study of the behavior of the susceptibility near the antiferromagnetic wave vector $\mathbf{Q}$.

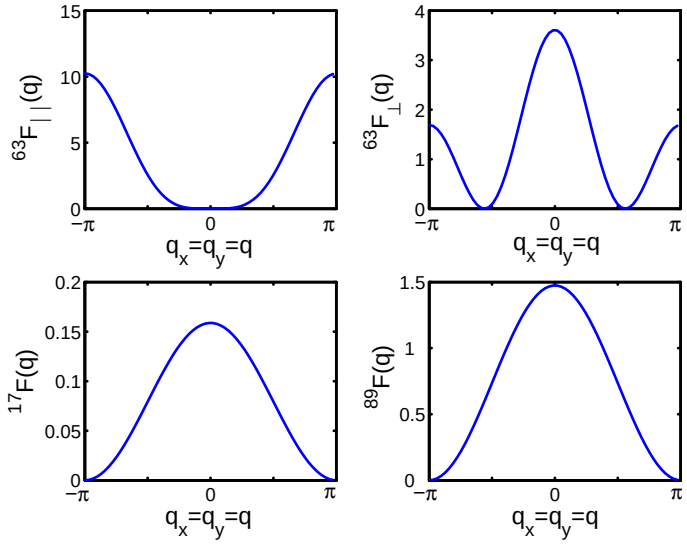

Figure 13: Form factors for different nuclei in $YBa_2Cu_3O_7$.

4.2.5 Form factors

The large deviation in the relaxation rates of different nuclei can be explained via the form factors ${}^{\alpha}F_{\beta}$. These are given as

$$\begin{aligned} {}^{63}F_{\beta}(\mathbf{q}) &= \left[A_{\beta} + 2B\left(\cos(q_x a) + \cos(q_y b)\right)\right]^2, \\ {}^{17}F_{\beta}(\mathbf{q}) &= 2\left(C_{\beta_1}^2 \cos^2(q_x a/2) + C_{\beta_2}^2 \cos^2(q_y b/2)\right), \\ {}^{89}F_{\beta}(\mathbf{q}) &= \left[8D_{\beta} \cos(q_x a/2)\cos(q_y b/2)\cos(q_z c/2)\right]^2. \end{aligned} \tag{86}$$

Here A, B, C, and D stand for the couplings as described in Section 4.2.1.

The meaning of this formula is that the different nuclei "see" different parts of the $\mathbf{q}$–space. For example, the O–nucleus does not see the $(\pi/a, \pi/a)$ part of the space, whereas ${}^{63}F_c$ has a peak exactly at that location. This considerations serve for trying to explain the differences in the relaxation of the Cu(2) and O(2,3) nuclei. Figure 13 shows the form factors, computed for the case $q_x = q_y$. For the calculation we have utilised the hyperfine coupling

constants of $YBa_2Cu_3O_7$. These are believed to be $A_\parallel \simeq -4B$, $A_\perp \simeq 0.75B$, $C_\parallel \simeq 0.6B$, $C_\perp \simeq 0.32B$ and $B \simeq 0.4$ μeV. The discussed characteristics of the hyperfine form factors are clearly recognisable in the figure.

5 Results in the RPA approach

In the forthcoming sections we will analyze neutron scattering and NMR experiments, performed in the superconducting state of cuprates, with the help of the susceptibility in the RPA approximation form. In the normal state the susceptibility is only weakly temperature dependent (Pauli spin susceptibility), therefore we have restricted ourselves to the analysis of the superconducting state $T<T_c$. We must keep in mind that strictly speaking the RPA approximation is only valid for $U \ll t$ (weak coupling limit). We will see that in order to obtain agreement with experiments, a rather large value $U \geq t$ is needed in contradiction with the assumption made before. Thus using this model to describe high–T_c superconductors is questionable. Previously this model was studied by different authors [14, 50]. However, in these works the parameters used to describe the band structure were introduced from scratch. Recent high–resolution angle–resolved photoemission experimental results gave us the idea to re–examine this RPA model, by utilizing parameter values extracted from Fermi surface measurements.

The model for the susceptibility is given by the formula

$$\chi(\mathbf{q},\omega) = \frac{\chi_0(\mathbf{q},\omega)}{1 - U_e\chi_0(\mathbf{q},\omega)},$$

where $\chi_0(\mathbf{q},\omega)$ is the susceptibility in the BCS theory according to equation (38) and U_e is an effective Coulomb interaction parameter (not to confuse it for Hubbard U!). The evaluation of the spin susceptibility expression was carried out numerically by a trapezoidal integration over the first Brillouin zone.

In our calculations we assume the Fermi surface as given from fits to photoemission data. Based on this we analyze neutron scattering experiments to determine the approximate values of the fit parameters in the model. Experimental data indicate a large peak in the imaginary part of the susceptibility at $\omega \simeq 41$ meV. The position of this peak is very sensitive to the parameter values. We use this to our advantage and extract our parameters by positioning the peak along the ω–axis. Then we move to NMR experiments and try to calculate the temperature dependences of Knight shift, spin–lattice relaxation and spin–spin relaxation rates, utilizing the parameter values obtained before. Thus in our calculations we try to establish a connection between the three different experiments.

	Set 1 [60]	Set 2 [60]	Set 3 [28]	Set 4 [29]
t_1 [eV]	0.147	0.1387	0.1645	0.147
t_2 [eV]	-0.0365	-0.0332	-0.0177	-0.024
t_3 [eV]	-0.0024	-0.0033	0.0366	0.0326
t_4 [eV]	0.0324	0.0462	0.0155	0.0126
t_5 [eV]	-0.0017	-0.0066	-0.0107	-0.0235
μ [eV]	-0.1197	-0.0879	-0.1129	-0.0989
δ	0.39	0.42	0.41	0.42

Table 2: Tight binding parameters for $YBa_2Cu_3O_7$ (sets 1–2) and for $Bi_2Sr_2CaCu_2O_8$ (sets 3–4).

5.1 Parameters for the calculation

In this section we will discuss the parameters, which are needed to perform our calculations. First we would like to consider the kinetic hopping terms. These parameters we will adopt from photoemission experiments [28, 29, 60]. They are summarized in Table 2. Note that the parameter sets 1–2 are fitted to the Fermi surface of $YBa_2Cu_3O_7$, whereas sets 3–4 to that of $Bi_2Sr_2CaCu_2O_8$.

The band structure for a two dimensional quadratic lattice and five hopping terms $t_1 ... t_5$ is determined by equation (5)

$$\begin{aligned} \varepsilon_{\mathbf{k}} &= -2t_1 (\cos k_x + \cos k_y) \\ &- 4t_2 (\cos k_x \cos k_y) \\ &- 2t_3 (\cos 2k_x + \cos 2k_y) \\ &- 2t_4 (\cos 2k_x \cos k_y + \cos 2k_y \cos k_x) \\ &- 4t_5 (\cos 2k_x \cos 2k_y) - \mu. \end{aligned}$$

Here we introduced the chemical potential μ to fix the particle number. The band structure corresponding to parameter set 1 for $YBa_2Cu_3O_7$ is shown in Figure 14.

The corresponding Fermi functions in the normal and superconducting states

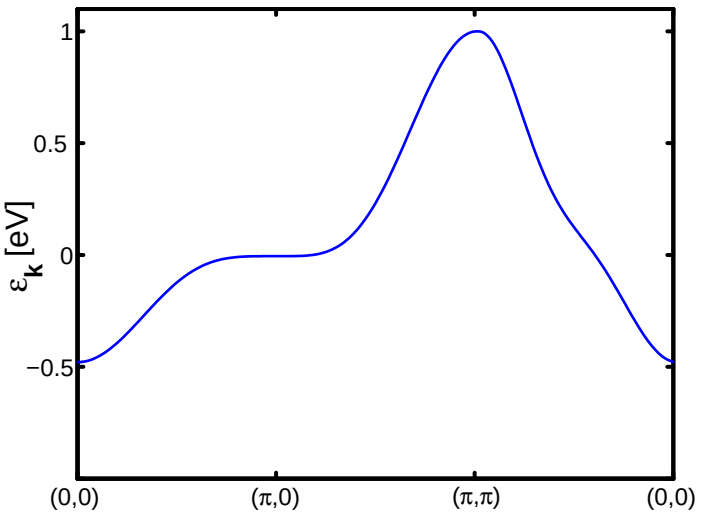

Figure 14: Tight binding band structure of $YBa_2Cu_3O_7$ according to photoemission experiments.

are given by

$$\begin{aligned} f(\varepsilon_{\mathbf{k}}) &= \frac{1}{\exp(\varepsilon_{\mathbf{k}}/k_B T)+1} \\ f(E_{\mathbf{k}}) &= \frac{1}{\exp(E_{\mathbf{k}}/k_B T)+1}, \end{aligned}$$

where $E_{\mathbf{k}} = \sqrt{(\varepsilon_{\mathbf{k}})^2 + |\Delta_{\mathbf{k}}|^2}$ is the energy of the quasiparticles with a wave vector dependent gap function $\Delta_{\mathbf{k}}$. Figure 15 shows the calculated two dimensional Fermi surfaces in the normal state (T= 90 K) for parameter sets 1–4. In Appendix B the behavior of the Fermi surfaces in the superconducting state is shown for different gap symmetries. The corresponding parameter to consider is the gap parameter Δ_0 from equation (48) on page 28. Estimates of this parameter indicate a value of $\Delta_0 \simeq 20 - 50$ meV. Next we consider the parameter Γ, which characterizes the lifetime of the quasiparticles. Bulut and Scalapino [14] found in their calculations that, in order to suppress the Hebel–Slichter peak in spin–lattice relaxation rates for the conventional s–wave, one needs to assume a large scattering rate Γ. In particular, they adopted a temperature dependent quasiparticle scattering rate

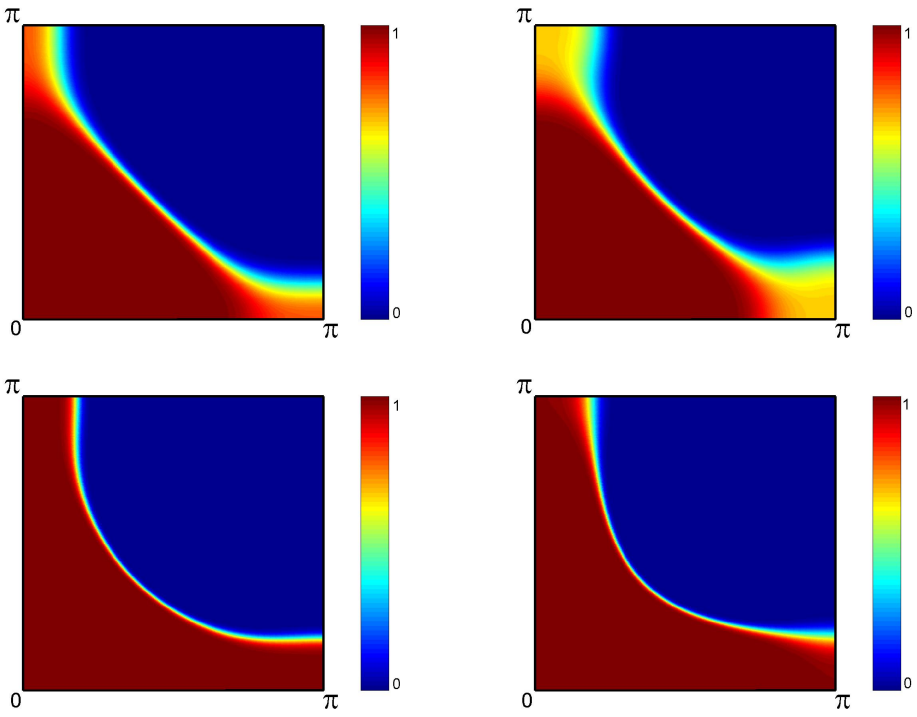

Figure 15: Fermi surfaces for $YBa_2Cu_3O_7$ (top) and $Bi_2Sr_2CaCu_2O_8$ (bottom) in the normal state, corresponding to parameter sets 1–4.

$\Gamma \simeq k_B T_c \, (T/T_c)^3$ [20, 66]. Later Thelen and Pines [81] discovered that such large values may not be compatible with spin–spin relaxation calculations. We will address this problem later in Section 5.3.2. For neutron scattering in the superconducting state, the quasiparticle scattering rate can be taken as constant. We will assume $\Gamma = 3$ meV in our calculations concerning neutron scattering. The last parameter to assess here is the renormalized Coulomb interaction U_e. This parameter will be considered as "free", since it cannot be directly extracted from experiments. We summarize our parameter selection:

- The hopping terms $t_1 ... t_5$ are taken from photoemission experiments.
- The gap parameter Δ_0 we allow to vary, but only within the values suggested by experiments, $\Delta_0 \simeq 20 - 50$ meV.

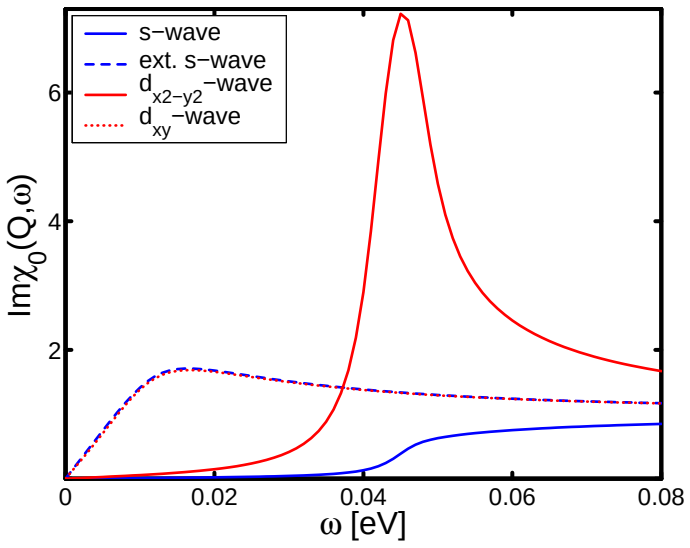

Figure 16: Imaginary part of the BCS susceptibility $Im\chi_0(\mathbf{Q},\omega)$ for different gap symmetries. The hopping parameters are taken from set 1, the gap parameter is chosen to be $\Delta_0 = 22$ meV.

- The quasiparticle scattering rate Γ will be taken as constant for the analysis of neutron scattering and temperature dependent for that of NMR calculations.
- The effective Coulomb interaction U_e is assumed as a free parameter.

5.2 Neutron scattering in $YBa_2Cu_3O_7$

5.2.1 General considerations

Magnetic inelastic neutron scattering experiments indicate a sharp resonance in the magnetic excitation spectrum of the optimally doped $YBa_2Cu_3O_7$ in the superconducting state, at a frequency $\omega \simeq 41$ meV, near the antiferromagnetic wave vector $\mathbf{Q}$ [8, 58]. Consequently, there should be a large peak in the imaginary part of the spin susceptibility $\chi(\mathbf{Q},\omega)$ at the same frequency. To understand how such a phenomenon can occur, we must study the behavior of the BCS susceptibility $\chi_0(\mathbf{Q},\omega)$.

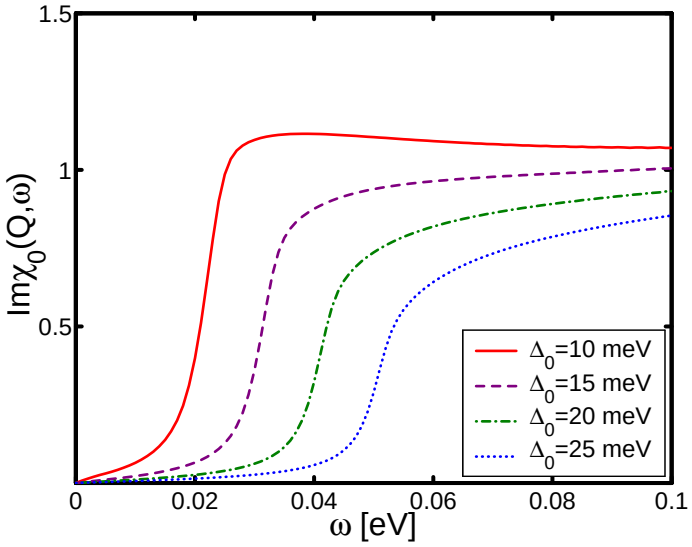

Figure 17: Imaginary part of the BCS susceptibility $Im\chi_0(\mathbf{Q},\omega)$ for the conventional s–wave gap. The hopping parameters are taken from set 1, the chosen values of the gap parameter are shown.

Figure 16 shows the BCS susceptibility for an average gap parameter value $\Delta_0 = 22$ meV, with hopping parameters taken from set 1 in Table 2. We notice that the frequency dependence of the BCS susceptibility is quite different for the various gap symmetries. The susceptibility with extended s–wave or d_{xy}–wave gap symmetry is increasing instantly at $\omega = 0$ and stays nearly constant at higher frequencies.

Contrary to this, the susceptibilities with conventional s–wave and $d_{x^2-y^2}$–wave gaps act quite differently. They exhibit a behavior which is a "window of transparency": the imaginary part of $\chi_0(\mathbf{Q},\omega)$ vanishes at low frequencies $\omega < 41$ meV. The ω–value, above which they increase, is determined by the magnitude of the gap parameter Δ_0. This feature is demonstrated in Figure 17, for the conventional s–wave gap.

In the region where the imaginary part of $\chi_0(\mathbf{Q},\omega)$ is small, the Stoner factor $(1 - U_e\chi_0(\mathbf{Q},\omega))$ can enhance the RPA susceptibility and creates a large peak as observed by neutron scattering experiments. By comparing the s–wave and $d_{x^2-y^2}$–wave cases we conclude that the transparency win-

dow has the same magnitude for a given value of the gap parameter Δ_0 (see Figure 16). More specifically, the transparency window is $\omega \simeq 2\Delta_0$. Consequently, for both the conventional s–wave and $d_{x^2-y^2}$–wave gap symmetries it is possible to obtain a peak in the imaginary part of the susceptibility at $\omega = 41$ meV. Considering the extended s–wave or d_{xy}–wave gap symmetries we conclude that it is impossible to produce any peak near the given frequency. The only region where the susceptibility can be enhanced is near $\omega = 0$, where $\chi_0(\mathbf{Q}, \omega)$ is small. This behavior was never observed in experiments, consequently these gap symmetries can be excluded from further analysis of neutron scattering measurements. Keeping in mind that our goal is to describe neutron scattering and NMR experiments simultaneously, we can also drop these gap symmetries for our NMR analysis.

5.2.2 Analysis of neutron scattering data

To analyze neutron scattering in $YBa_2Cu_3O_7$, we use the Fermi surfaces described by parameter sets 1 and 2. These sets yield very similar Fermi surfaces as it can be seen in Figure 15. In both cases almost identical neutron scattering peaks can be obtained, by variation of the fit parameters. This is demonstrated in Figure 18 for the d–wave symmetry. Thus in our analysis we will restrict ourselves to set 1.

Let us consider now how the position of the peak reacts to the change of parameters. As already described in Section 5.2.1, changing the gap parameter Δ_0 will result in reduction or increase of the transparency window. The other variable to consider is the effective Coulomb interaction U_e. Figure 19 shows the imaginary part of the BCS susceptibility $\chi_0(\mathbf{Q}, \omega)$ as well as the enhanced RPA susceptibility $\chi(\mathbf{Q}, \omega)$, for different values of U_e. By analysing the figure we observe that, upon rising the value of U_e, the peak shifts to lower frequencies and it increases due to the increasingly smaller values of $\chi_0(\mathbf{Q}, \omega)$.

Now let us consider the two remaining gap candidates, the conventional s–wave and the $d_{x^2-y^2}$–wave gap symmetries. Upon re–examination of Figure 16 and Figure 17 it is evident, that the minimum value of Δ_0 must be around 20 meV for both symmetries. Otherwise there would be no transparency window near $\omega = 41$ meV, thus no peak would appear there. Previous Knight shift calculations [13, 14, 16, 17] show us that, in order to obtain agreement with NMR experiments, the values of Δ_0 and U_e must be taken

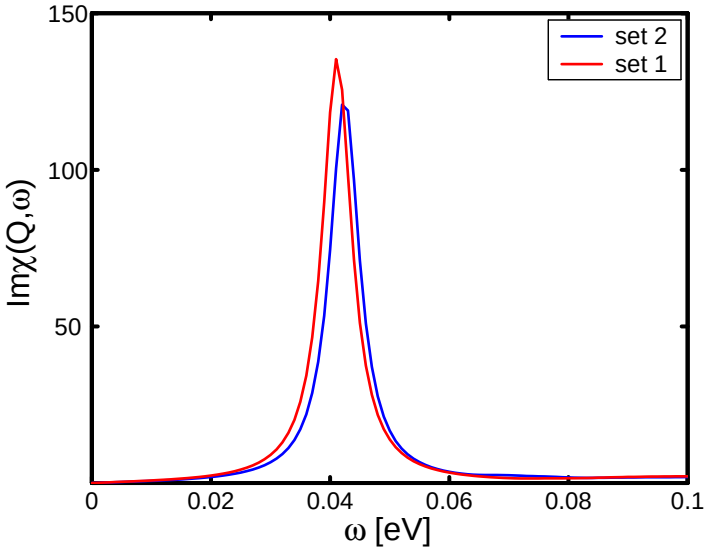

Figure 18: Imaginary part of the RPA susceptibility $Im\chi\left(\mathbf{Q},\omega\right)$ for parameter sets 1 and 2. The gap parameter is $\Delta_0 = 40$ meV, the effective Coulomb interaction is $U_e = 0.265$ eV for set 1 and $U_e = 0.172$ eV for set 2.

as small as possible. We will see that in the case of d–wave symmetry much smaller values of the interaction parameter will be needed ($U_e = 0.12$ eV). This will be crucial in the simultaneous explanation of neutron scattering and NMR experiments.

In Figure 20 we display our final results for the conventional s–wave and the $d_{x^2-y^2}$–wave symmetry, calculated in the framework of the RPA susceptibility. These results were determined with keeping in mind that the gap parameter Δ_0 should be the smallest possible. By examination of the figure we conclude that, both in the case of a conventional s–wave and a $d_{x^2-y^2}$–wave gap symmetry, it is possible to attain a clear peak in the imaginary part of the RPA spin susceptibility near the antiferromagnetic wave vector $\mathbf{Q}$, at the frequency $\omega \simeq 41$ meV.

Calculations show that for obtaining a peak in the d–wave case, the value of the interaction parameter U_e should exceed 0.1 eV. Contrary to this, for getting a peak in the s–wave case, the minimum value of U_e should be around 0.4 eV. Thus, the magnitude of the effective Coulomb interaction U_e must be rather large in order to obtain agreement with neutron scattering measure-

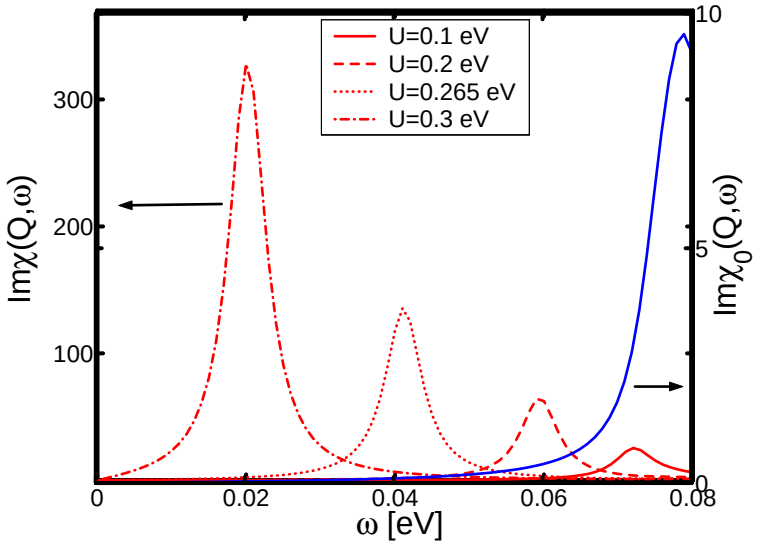

Figure 19: Imaginary part of the BCS $Im\chi_0(\mathbf{Q},\omega)$ (blue) and RPA $Im\chi(\mathbf{Q},\omega)$ (red) susceptibility for d–wave symmetry. The gap parameter is $\Delta_0 = 40$ meV, U_e values are shown.

ments. We will see in the forthcoming sections that such a large value of this parameter is incompatible with NMR experiments.

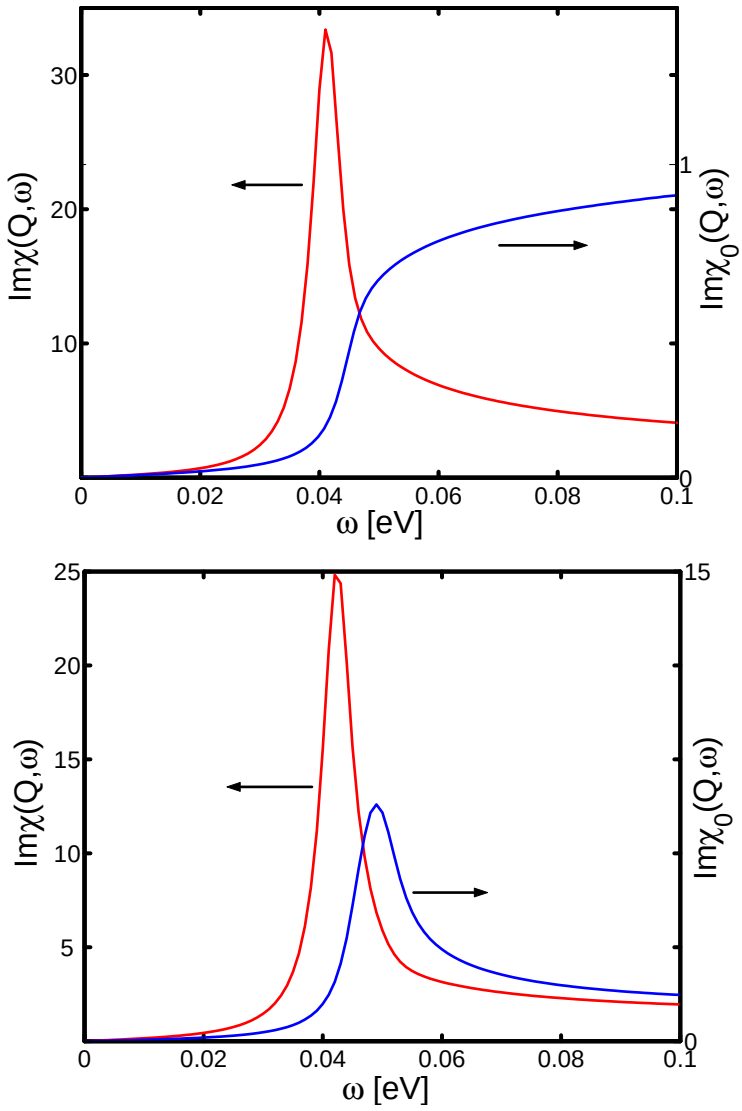

Figure 20: Imaginary part of the BCS $Im\chi_0(\mathbf{Q},\omega)$ (blue) and RPA $Im\chi(\mathbf{Q},\omega)$ (red) spin susceptibility for s–wave (top) and d–wave (bottom) gap symmetries. The parameters for the s–wave symmetry are $\Delta_0 = 22$ meV, $U_e = 0.4$ eV while in the d–wave case they are $\Delta_0 = 24$ meV and $U_e = 0.12$ eV.

5.3 NMR in $YBa_2Cu_3O_7$

5.3.1 Knight shift

In order to calculate the temperature dependence of the Knight shift we will utilize the Yosida function [85]. The real part of the susceptibility can be approximated in the limit $\mathbf{q} \to 0$, $\omega = 0$ by

$$\chi_0 \left(\mathbf{q} \to 0, \omega = 0 \right) \simeq \frac{\beta}{N} \sum_{\mathbf{k}} \frac{\partial f \left(E_{\mathbf{k}} \right)}{\partial E_{\mathbf{k}}}.$$

Then the RPA susceptibility takes the form

$$\chi \left(\mathbf{q} \to 0, \omega = 0 \right) = \frac{\chi_0 \left(\mathbf{q} \to 0, \omega = 0 \right)}{1 - U_e \chi_0 \left(\mathbf{q} \to 0, \omega = 0 \right)}.$$

With the help of this relation, the Knight shift can be calculated from equation (83) on page 41. We will calculate the temperature dependence of the normalized value $K_s(T)/K_s(T_c)$, where the index s indicates spin shifts, without orbital contribution. This way the hyperfine constants in equation (83) cancel, simplifying our calculations.

As a first step we consider the case of no interaction $U_e = 0$ eV. Figure 21 displays the calculated Knight shifts for the various gap symmetries. Since the extended s–wave and d_{xy}–wave gap symmetries could already be excluded by the analysis of neutron scattering experiments, the remaining pairing symmetries to consider are the conventional s–wave and the $d_{x^2-y^2}$–wave symmetries. By examination of the figure, we conclude that for the s–wave symmetry the magnitude of the gap parameter must be between $\Delta_0 = 15 - 20$ meV, whereas for d–wave symmetry it should be between $\Delta_0 = 20 - 30$ meV. This is in accordance with values obtained before for neutron scattering in Section 5.2.2, for both symmetries. However, we must keep in mind that we have set the interaction parameter $U_e = 0$ eV. Next we investigate the role of this parameter in our calculations.

In Figure 22 we show calculated Knight shifts for s–wave and d–wave gap symmetries for various values of U_e. By analyzing the figure we see that for s–wave pairing the corresponding values of U_e are much lower then those determined by the analysis of neutron scattering experiments (cf. Figure 20).

For the d–wave symmetry the magnitude of the fitting parameter U_e is about the same as for neutron scattering. Generally we can say that the temperature dependence of the Knight shifts in the superconducting state is most sensitive to variation of the gap parameter Δ_0. By adjusting the effective interaction U_e we can tune the progression of the Knight shift only slightly.

In Figure 23 we display our final result for the Knight shifts, calculated with the RPA susceptibility. These curves are adjusted to the experiments by the variation of both the gap parameter Δ_0 and U_e. We conclude that it is possible to get reasonable agreement with experiments both for s–wave and d–wave gap symmetries.

However, two points must be stressed here. First, at low temperatures only the d–wave gap symmetry gives satisfactory agreement to the data, because in the s–wave case the calculated Knight shift vanishes for temperatures $T \ll T_c$. Secondly, the values of the fitting parameters match those obtained for neutron scattering (cf. Figure 20) only for d–wave symmetry.

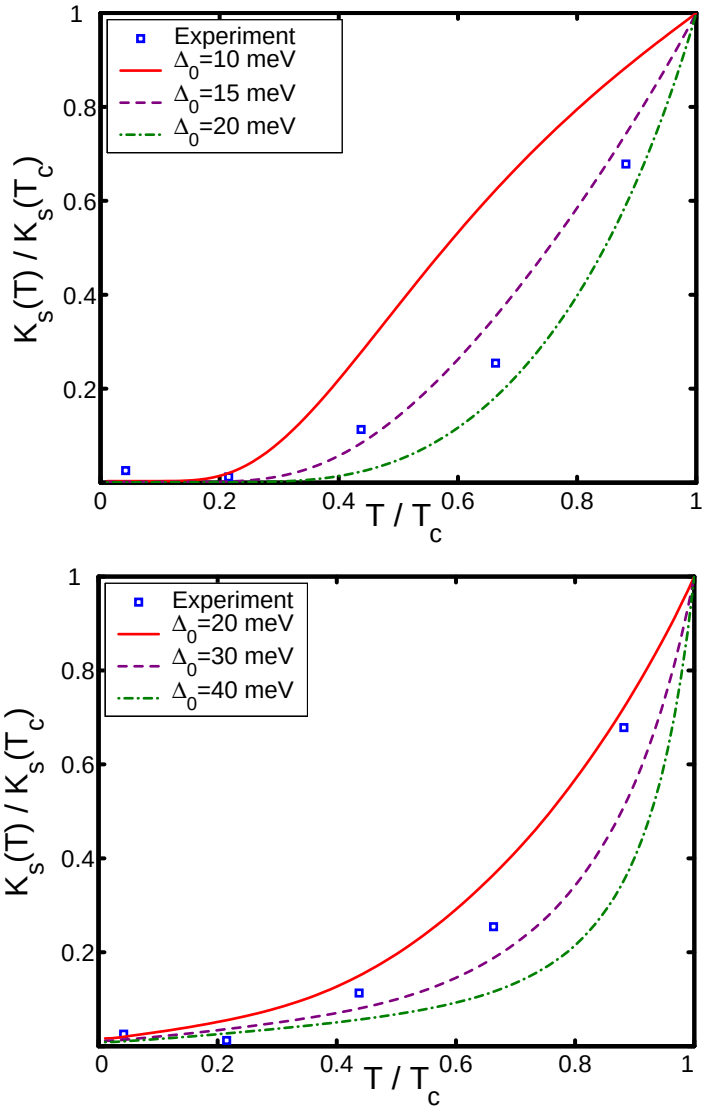

Figure 21: Spin shifts in the superconducting state of $YBa_2Cu_3O_7$ for no interaction $U_e = 0$ eV. Results for s–wave (top) and d–wave (bottom) symmetries are shown. The experimental points are taken from [3].

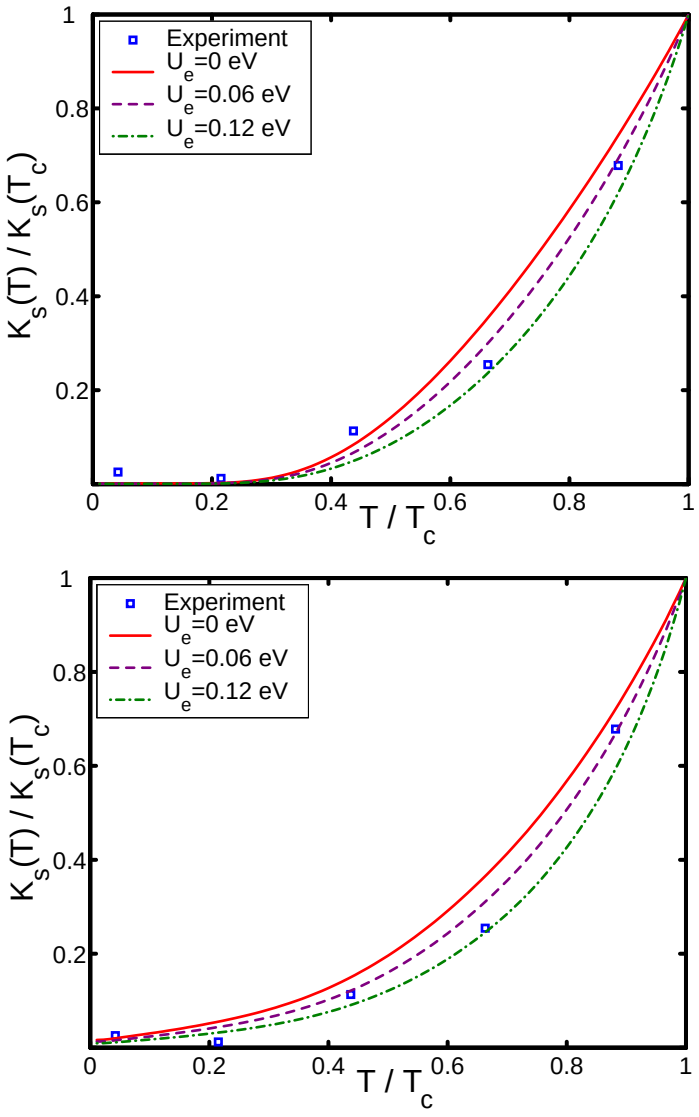

Figure 22: Spin shifts in the superconducting state of $YBa_2Cu_3O_7$ for various interaction parameters U_e. Results for s–wave (top) and d–wave (bottom) symmetries are shown. The gap parameter for the s–wave symmetry is taken as $\Delta_0 = 15$ meV, while in the d–wave case $\Delta_0 = 20$ meV. The experimental points are taken from [3].

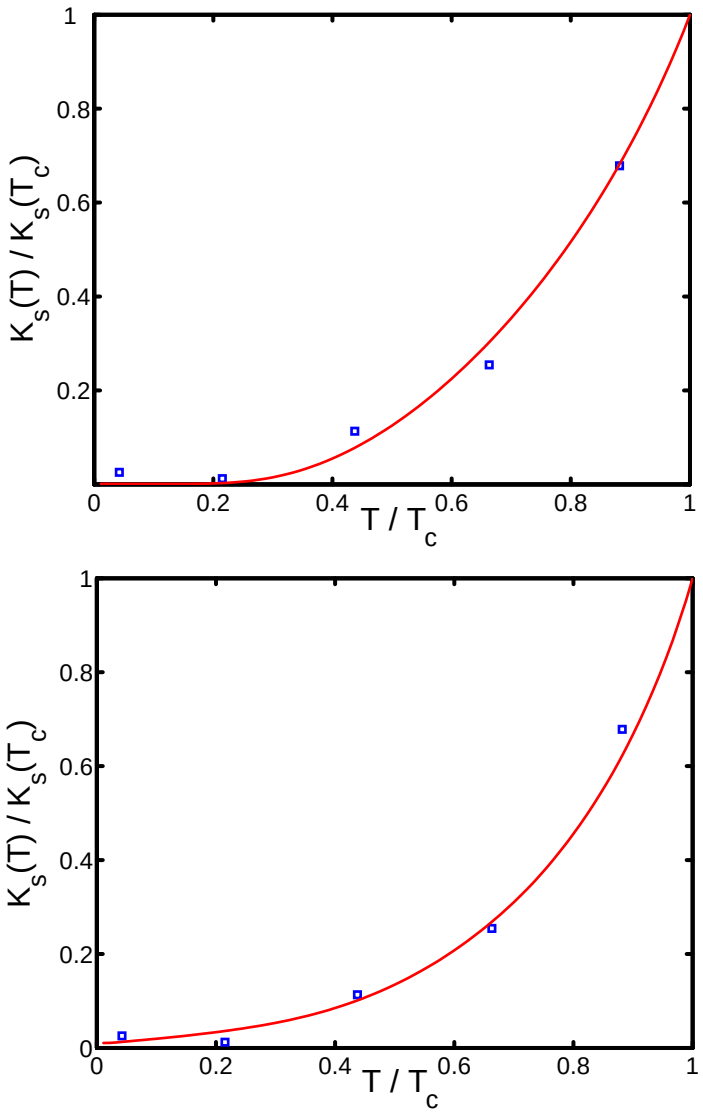

Figure 23: Spin shifts in the superconducting state of $YBa_2Cu_3O_7$ for s–wave (top) and d–wave (bottom) gap symmetries. The parameters for the s–wave symmetry are $\Delta_0 = 13$ meV, $U_e = 0.13$ eV while in the d–wave case $\Delta_0 = 20$ meV and $U_e = 0.1$ eV. The experimental points are taken from [3].

5.3.2 Spin–spin relaxation

The NMR spin–spin relaxation is calculated according to equation (85) on page 42. We will calculate the temperature dependence of the normalized spin–spin relaxation rate $T_{2G}^{-1}(T)/T_{2G}^{-1}(T_c)$ in the same way as we analyzed the Knight shifts. Thus the constants in equation (85) cancel, but the essential physics is preserved. The spin–spin relaxation time allows us to study the behavior of the real part of the spin susceptibility, near the antiferromagnetic wave vector $\mathbf{Q}$. In their phenomenological approach Zha, Barzykin and Pines [87] predicted that the spin–spin relaxation T_{2G}^{-1} can be approximated by taking the limit $\mathbf{q} = \mathbf{Q}$ in the susceptibility. We found that in microscopical models this is generally not true. However, the difference between performing the whole integration according to equation (85) and taking the limit $\mathbf{q} = \mathbf{Q}$ in the susceptibility is small (compare the dashed lines in Figure 24 with those in Figure 26). Thus in order to understand the behavior of the spin–spin relaxation in the superconducting state, we must first study the behavior of the real part of the susceptibility near the antiferromagnetic wave vector $\mathbf{Q}$.

In Figure 24 we display $Re\chi_0(\mathbf{Q}, \omega = 0)$ for s–wave and $d_{x^2-y^2}$–wave symmetries and for different values of the quasiparticle scattering rate Γ. We notice that the behavior of the BCS spin susceptibility $Re\chi_0(\mathbf{Q}, \omega = 0)$ differs substantially for s–wave and d–wave gap symmetries. For large values of Γ the susceptibility with d–wave gap symmetry increases upon entering the superconducting state near T_c. Subsequently at lower temperatures it decreases slightly. Contrary to this, the susceptibility with s–wave gap symmetry decreases immediately at T_c. We associate this difference to the different behavior of the coherence factors for the two symmetries.

Let us now consider how this effect depends on the wave–vector $\mathbf{q}$ for the d–wave gap. Figure 25 shows the temperature dependence of the susceptibility for different wave vectors. We see that the increase in the susceptibility is strongly related to the antiferromagnetic wave vector $\mathbf{Q}$. For small wave vectors the effect vanishes completely. If we switch on the effective interaction U_e, it enhances the susceptibility even more. This enhancement is also shown in Figure 25.

Now let us turn to the examination of the spin–spin relaxation time T_{2G}^{-1}. First we wish to consider the case of no interaction $U_e = 0$ eV. Figure 26 shows the calculated spin–spin relaxation rates for s–wave and d–wave gap

symmetries. We notice that for the hypothetical case of no interaction, both the s–wave and d–wave gap symmetry can account for the observed temperature dependence of the spin–spin relaxation rate T_{2G}^{-1} with appropriately chosen Δ_0. Note that the s–wave is in favour of a large scattering rate Γ, since it slows the rapid decrease of T_{2G}^{-1} (see dotted line in Figure 26). For the d–wave symmetry the large scattering rate results in an increase of T_{2G}^{-1} near T_c upon entering the superconducting state, which was never[2] observed in experiments.

Now we switch on the effective Coulomb interaction U_e. In Figure 27 we display the calculated spin–spin relaxation times for various values of the interaction parameter U_e. We observe that the results are not strikingly different from the non–interacting case. For large values of U_e the spin–spin relaxation times with an s–wave gap symmetry decrease rapidly upon entering the superconducting state and give no satisfactory agreement to the experiment. For the d–wave gap symmetry the anomalous behavior near T_c is still present if we assume a large quasiparticle scattering rate Γ.

Our final results are displayed in Figure 28. In order to fit the experiment with an s–wave gap, we must assume that the effective Coulomb interaction is $U_e = 0$ eV. This is in accordance with Knight shift calculations, but contradicts the values for the analysis of neutron scattering experiments. The quasiparticle scattering rate Γ is assumed large for the s–wave symmetry, since it helps to slow the rapid decrease of the spin–spin relaxation times. The relaxation rates calculated with a d–wave gap symmetry behave quite differently. They fit the experimental data for the same set of parameters as neutron scattering and Knight shift. However, the quasiparticle scattering rate must be taken as negligible. For a large scattering rate, the results do not agree with experiments (see dotted line in Figure 28). This contradicts previous quasiparticle scattering rate estimates and calculations [20, 66].

[2]The only experiment to date, which indicate such behavior was preformed in the compound $HgBa_2CuO_{4+\delta}$ [45], but was never confirmed in any other high–T_c superconductor.

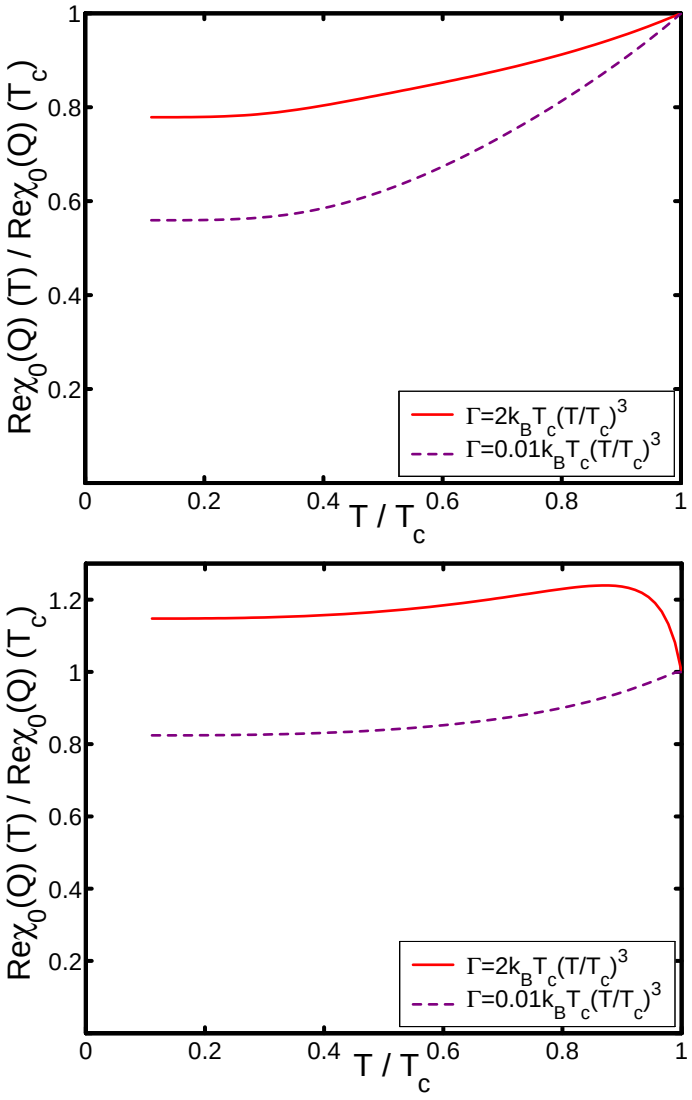

Figure 24: Real part of the BCS spin susceptibility $Re\chi_0\left(\mathbf{Q},\omega=0\right)$ for different quasiparticle scattering rates Γ. Results for s–wave (top) and d–wave (bottom) symmetries are shown. The superconducting gap parameter is chosen to be $\Delta_0 = 15$ meV for the s–wave and $\Delta_0 = 30$ meV for the d–wave symmetry.

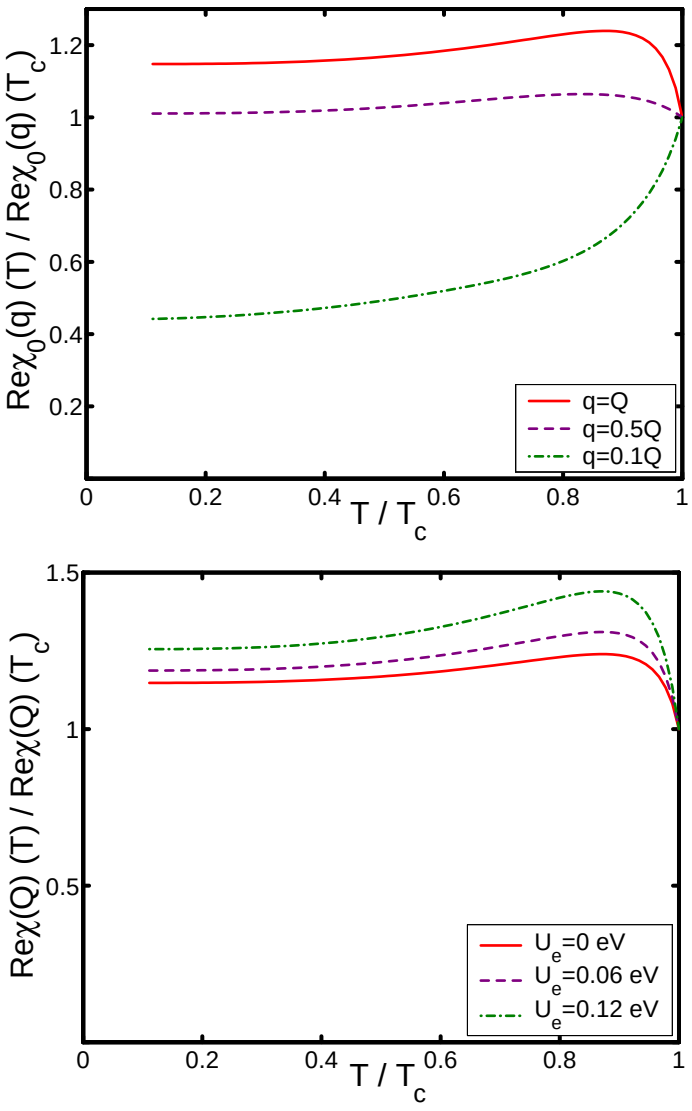

Figure 25: Real part of the spin susceptibility for d–wave gap symmetry. The wave–vector dependence of the BCS susceptibility $Re\chi_0\left(\mathbf{q},\omega=0\right)$ (top) and the RPA susceptibility $Re\chi\left(\mathbf{Q},\omega=0\right)$ with effective interaction U_e (bottom) is shown. The quasiparticle scattering rate is assumed as $\Gamma = 2k_BT_c\left(T/T_c\right)^3$ and the gap parameter is taken as $\Delta_0 = 30$ meV.

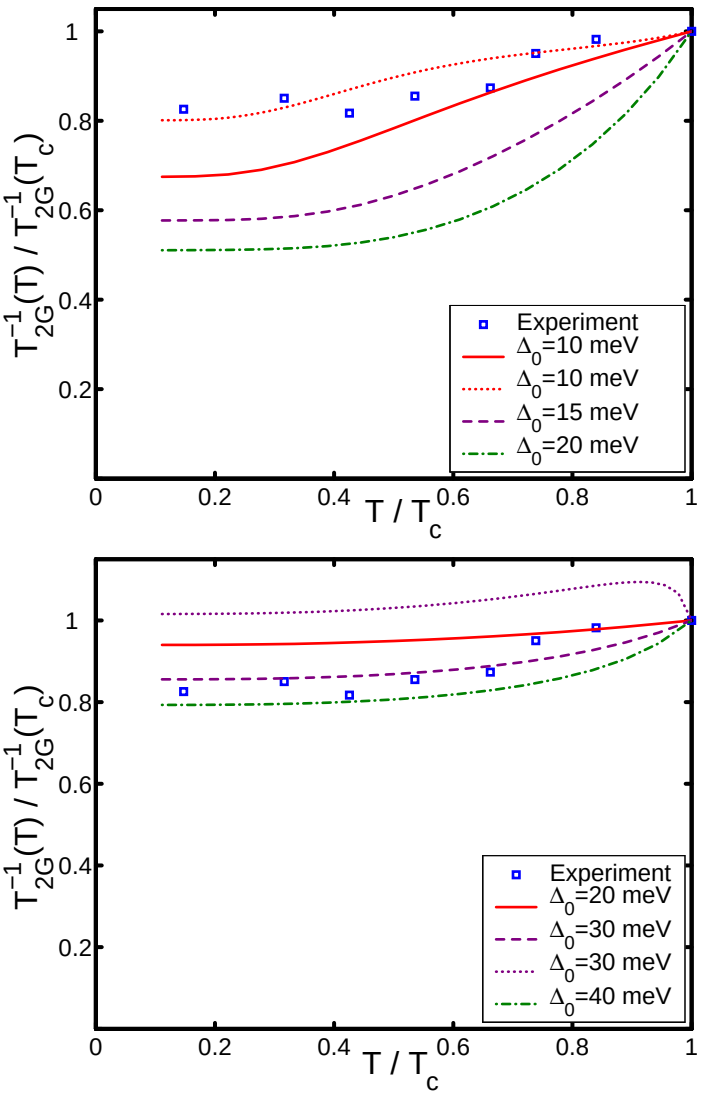

Figure 26: Spin–spin relaxation rates in the superconducting state of $YBa_2Cu_3O_7$ for no interaction $U_e = 0$ eV. Results for s–wave (top) and d–wave (bottom) gap symmetries are shown. The quasiparticle scattering rate is taken as negligible, except for the dotted lines which correspond to large quasiparticle scattering rates $\Gamma = k_B T_c \, (T/T_c)^3$. The experimental points are taken from [75].

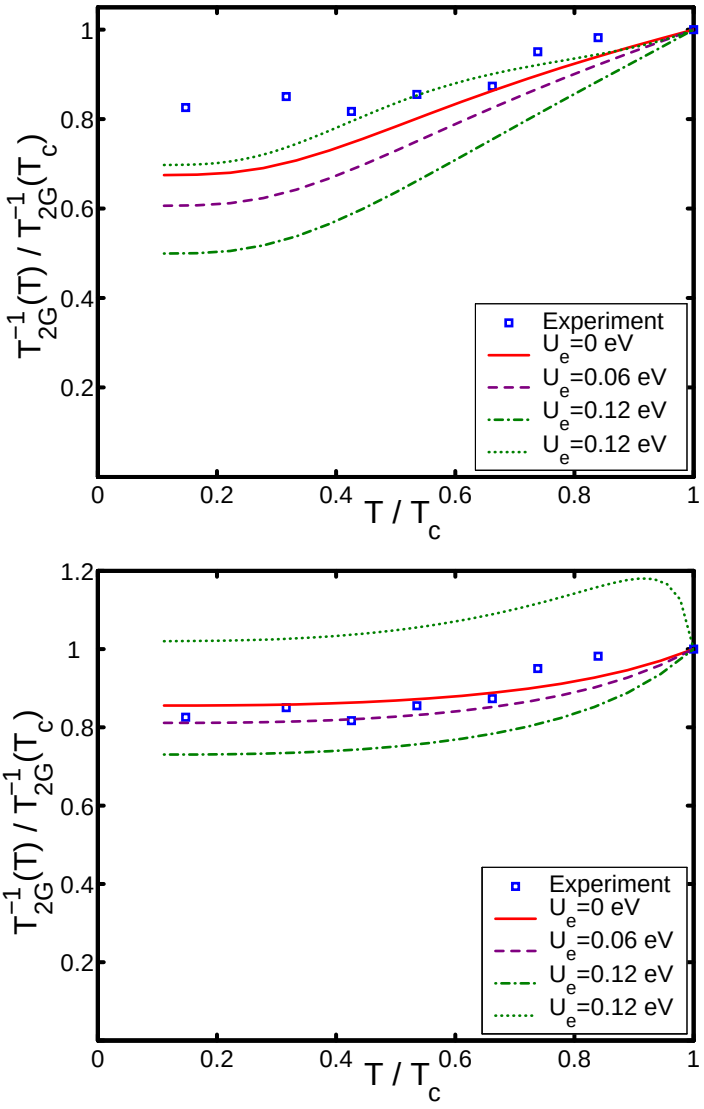

Figure 27: Spin–spin relaxation rates in the superconducting state of $YBa_2Cu_3O_7$ for various values of U_e. Results for s–wave (top) and d–wave (bottom) symmetries are shown. The gap parameter is $\Delta_0 = 10$ meV for the s–wave symmetry and $\Delta_0 = 30$ meV for the d–wave case. The quasiparticle scattering rate is taken as negligible, except for the dotted lines which correspond to a large quasiparticle scattering rates $\Gamma = k_B T_c \, (T/T_c)^3$. The experimental points are taken from [75].

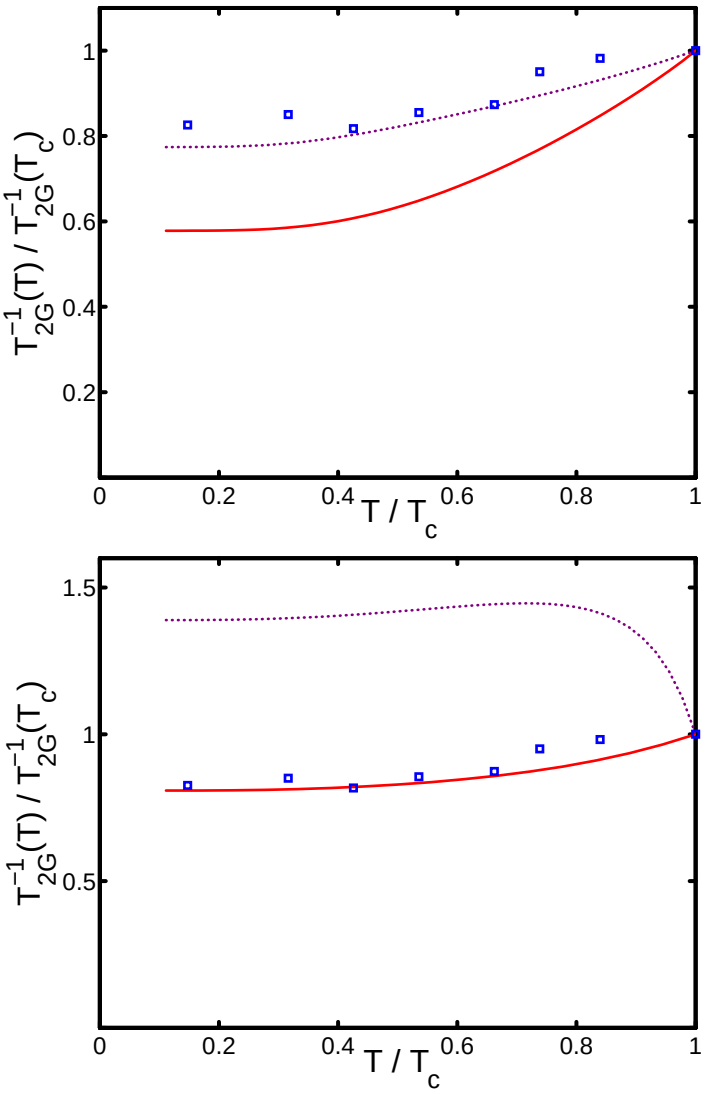

Figure 28: Spin–spin relaxation rates in the superconducting state of $YBa_2Cu_3O_7$ calculated for s–wave (top) and d–wave (bottom) symmetries. The parameters for the s–wave symmetry are $\Delta_0 = 15$ meV and $U_e = 0$ eV whereas for the d–wave case they are $\Delta_0 = 24$ meV and $U_e = 0.12$ eV. The quasiparticle scattering rate is taken as negligible except for the dotted lines which correspond to a large quasiparticle scattering rates $\Gamma = 2k_B T_c \, (T/T_c)^3$. The experimental points are taken from [75].

5.3.3 Spin–lattice relaxation

The nuclear spin–lattice relaxation is calculated according to equation (84) on page 42. As in the previous sections, we will calculate the temperature dependence of the normalized relaxation rates $T_1^{-1}(T)/T_1^{-1}(T_c)$. Similarly to the spin–spin relaxation rates, it is of interest to study the behavior of the susceptibility near the antiferromagnetic wave vector $\mathbf{Q}$, for different quasiparticle scattering rates Γ. The temperature dependence of the imaginary part of the susceptibility $Im\chi(\mathbf{Q},\omega)$ will ultimately be reflected in the behavior of the spin–lattice relaxation time ${}^{63}T_{1c,ab}^{-1}(T)$.

In Figure 29 we display the temperature dependence of $Im\chi(\mathbf{Q},\omega)$ for s–wave and d–wave gap symmetries. By examination of the figure we see that the imaginary part of the susceptibility near the antiferromagnetic wave vector $\mathbf{Q}$ behaves quite differently for s–wave and d–wave gap symmetries. For small quasiparticle scattering rates the susceptibility with s–wave symmetry shows a Hebel–Slichter like behavior: its value is increased upon entering the superconducting state near T_c. Contrary to this, the susceptibility with d–wave gap symmetry shows no such peak for small scattering rate Γ. In the case of large scattering rate the situation is reversed. The Hebel–Slichter peak for s–wave gap symmetry is destroyed, while for d–wave symmetry a clear peak appears. In high–T_c superconductors a Hebel–Slichter peak was never observed in NMR experiments. Thus we conclude that the imaginary part of the spin susceptibility and therefore the spin–lattice relaxation ${}^{63}T_{1c,ab}^{-1}(T)$ is in favor of a large quasiparticle scattering rate for conventional s–wave gap symmetry, while for d–wave symmetry the scattering rate must be rather small.

Let us now turn to the direct examination of spin–lattice relaxation rates. According to Moriya [56] the nuclear spin–lattice relaxation is calculated by taking the limit $\omega \to 0$ in equation (84). For the BCS susceptibility however, one arrives at

$$\lim_{\omega\to 0} \frac{Im\chi_0(\mathbf{q},\omega)}{\omega} \to \infty.$$

This problem can be addressed phenomenologically. One possibility is to interpret the limit $\omega \to 0$ as $\omega \to \Gamma$. This way the quantity $Im\chi_0(\mathbf{q},\omega)/\omega$ is no longer infinite and the essential physics (the temperature dependence of $Im\chi_0(\mathbf{q},\omega)$) is preserved.

In our calculations we proceed as before and first try to calculate the temperature dependence of the spin–lattice relaxation times in the non–interacting case $U_e = 0$ eV. We assume large quasiparticle scattering rates for the s–wave gap and small scattering rates for the d–wave symmetry.

Figure 30 shows the calculated spin–lattice relaxation rates. We see, that it is possible to account for the observed temperature dependence with a non–interacting susceptibility in both cases by choosing appropriate values for Δ_0. In general, the calculated spin–lattice relaxation rate with d–wave gap symmetry fits the experimental data better, than the s–wave.

Let us now discuss how the spin–lattice relaxation rates depend on the interaction parameter U_e. In Figure 31 we display the calculated spin–lattice relaxation rates. We notice that the interaction parameter U_e has less influence on the temperature dependence of the spin–lattice relaxation rates, than the gap parameter Δ_0. With the variation of U_e we can tune the temperature dependence of the spin–lattice relaxation rates only slightly.

In Figure 32 we depict our final result for the spin–lattice relaxation rate ${}^{63}T_{1c}^{-1}(T)$. We see that it is possible to describe the experimental results with both s–wave gap and d–wave gap symmetries. However there are significant differences in the choices of parameters in both cases. The calculated spin–lattice relaxation rates with s–wave gap symmetry favour very large quasiparticle scattering rates. This behavior we already observed by the calculation of the spin–spin relaxation times (see Figure 28 on page 66). Furthermore, the interaction parameter U_e plays no significant role for the s–wave, it can be set to zero in agreement with Knight shift and spin–spin relaxation calculations. Contrary to this, the calculated spin–lattice relaxation rates with d–wave symmetry behave differently. They favour smaller quasiparticle scattering rates and the interaction parameter is $U_e = 0.12$ eV, in agreement with previous calculations.

Next we would like to calculate the spin–lattice relaxation rates for other nuclei and other field directions. In particular, we are interested in the anisotropy ratios ${}^{63}T_{1ab}^{-1}/{}^{63}T_{1c}^{-1}$ and ${}^{63}T_{1c}^{-1}/{}^{17}T_{1c}^{-1}$. Experimental evidence [2, 51, 78] points toward a field dependence of these quantities. In particular, large anisotropies were reported in weak external fields. We would like to see if our calculations can account for the observed temperature dependence of these anisotropies.

In Figure 33 we display the calculated anisotropy ratios ${}^{63}T_{1ab}^{-1}/{}^{63}T_{1c}^{-1}$ for s–

wave and d–wave gap symmetries. We observe that the calculated anisotropy ratio with a d–wave symmetry match the experimental observation qualitatively. For the s–wave gap symmetry no agreement could be found with the experiments.

The anisotropy ratio between the relaxation rates of the copper and oxygen nuclei is shown in Figure 34. It is evident from the figure that it is not possible to explain the temperature dependence of the anisotropy ratio ${}^{63}T_{1c}^{-1}/{}^{17}T_{1c}^{-1}$ within the framework of this model. The calculated anisotropy ratios disagree with weak field experiments for both symmetries.

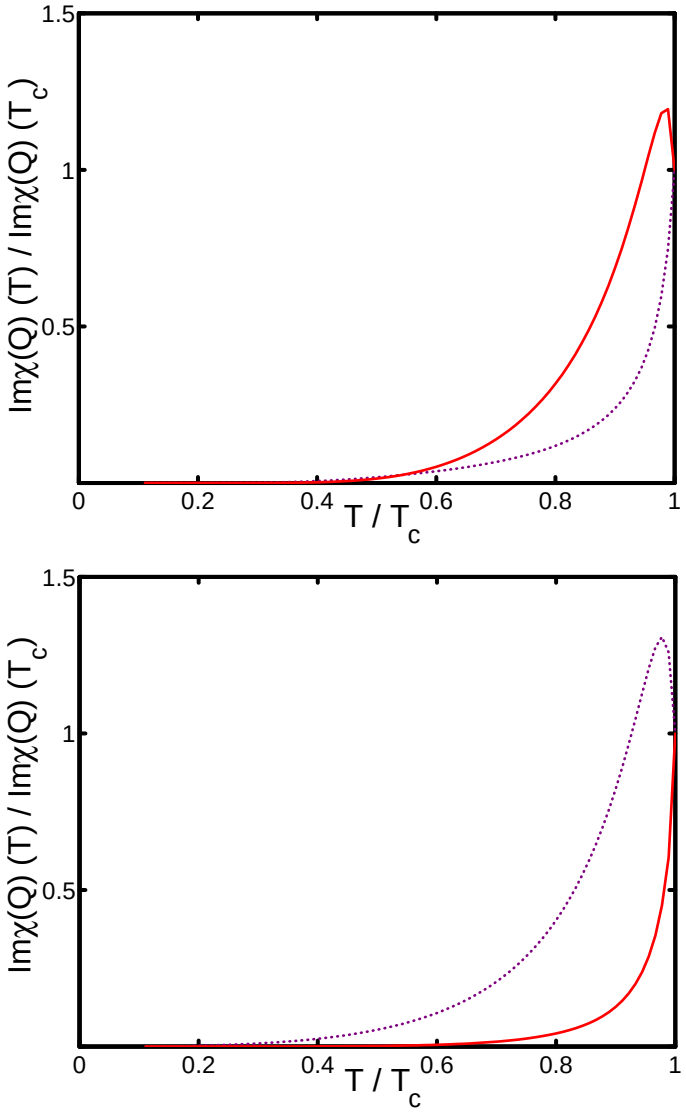

Figure 29: Temperature dependence of the imaginary part of the RPA susceptibility $Im\chi(\mathbf{Q},\omega)$ for s–wave (top) and d–wave (bottom) gap symmetries. The parameters are $\Delta_0 = 30$ meV, $U_e = 0.1$ eV and $\omega = 1$ meV. The solid lines correspond to small quasiparticle scattering rates $\Gamma = 0.1 k_B T_c (T/T_c)^3$, for the dotted lines the quasiparticle scattering rate is large $\Gamma = 2 k_B T_c (T/T_c)^3$.

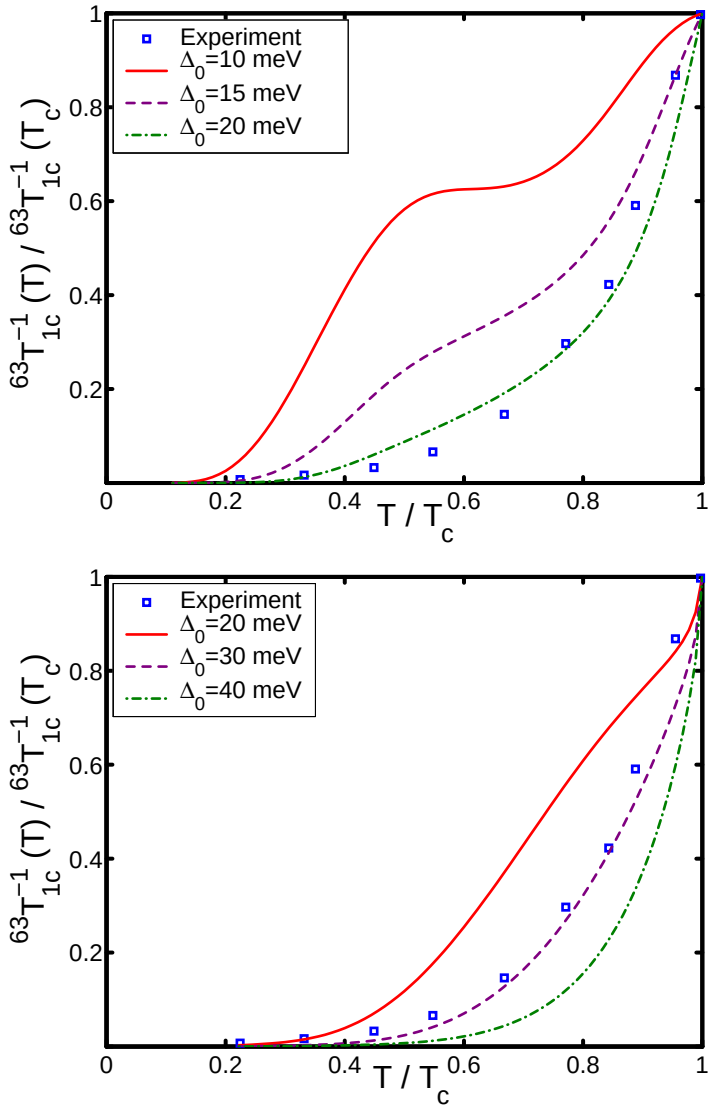

Figure 30: Spin–lattice relaxation rate in the superconducting state of $YBa_2Cu_3O_7$ for no interaction $U_e = 0$ eV. Results for s–wave (top) and d–wave (bottom) gap symmetries are shown. The quasiparticle scattering rate is large for the s–wave gap and small in the d–wave gap case. The experimental points are taken from [79].

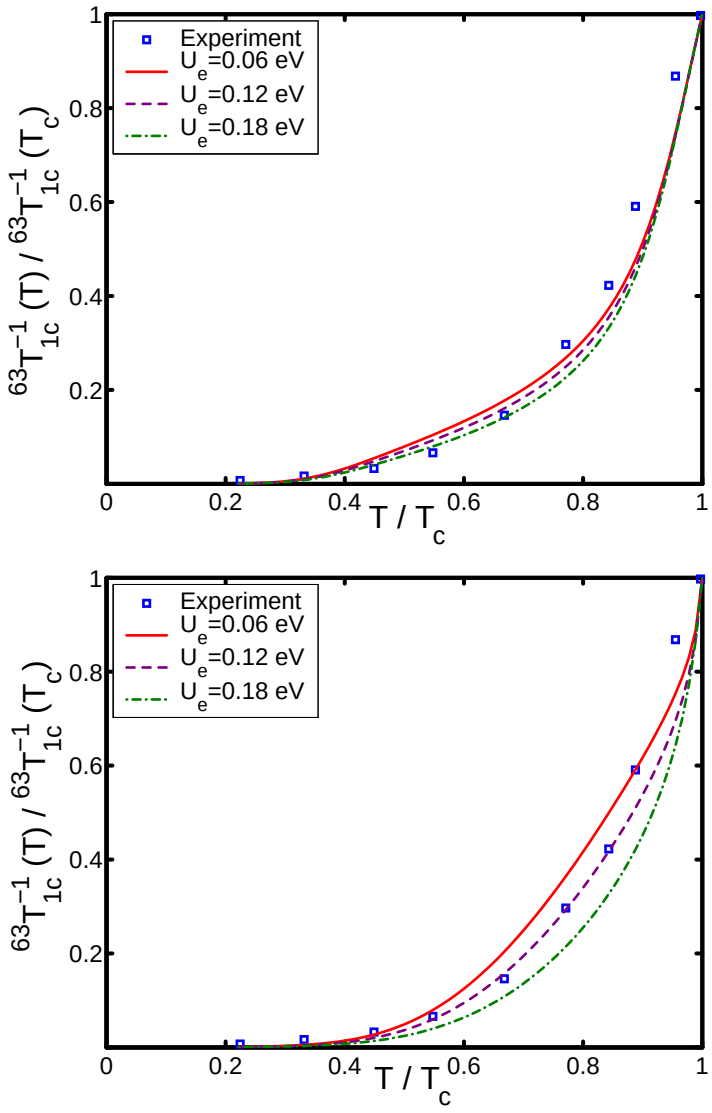

Figure 31: Spin–lattice relaxation rate in the superconducting state of $YBa_2Cu_3O_7$ for various values of U_e. Results for s–wave (top) and d–wave (bottom) gap symmetries are shown. The gap parameter is $\Delta_0 = 20$ meV for the s–wave and $\Delta_0 = 24$ meV for the d–wave symmetry. The quasiparticle scattering rate is large for the s–wave gap and small in the d–wave gap case. The experimental points are taken from [79].

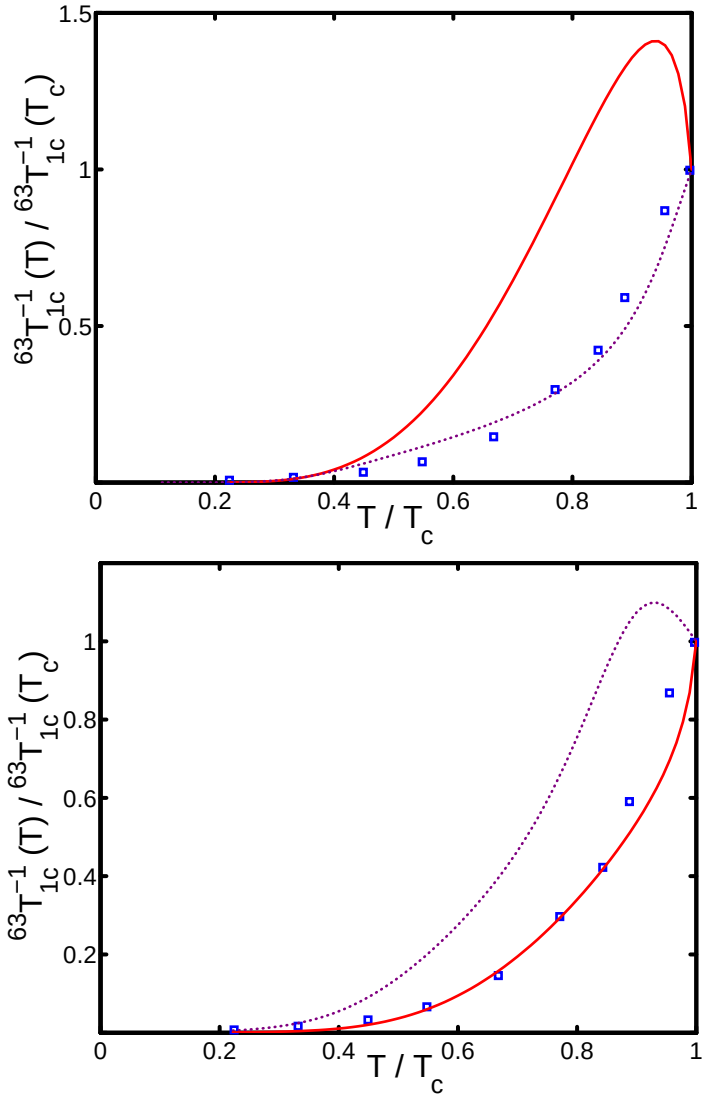

Figure 32: Spin–lattice relaxation rate in the superconducting state of $YBa_2Cu_3O_7$ for s–wave (top) and d–wave (bottom) gap symmetries. The parameters are $\Delta_0 = 20$ meV, $U_e = 0$ eV for the s–wave and $\Delta_0 = 24$ meV, $U_e = 0.12$ eV for the d–wave case. Furthermore the solid lines correspond to small scattering rates $\Gamma \simeq 0.4 k_B T_c \, (T/T_c)^3$, whereas the dotted lines to large values $\Gamma \simeq 2.5 k_B T_c \, (T/T_c)^3$. The experimental points are taken from [79].

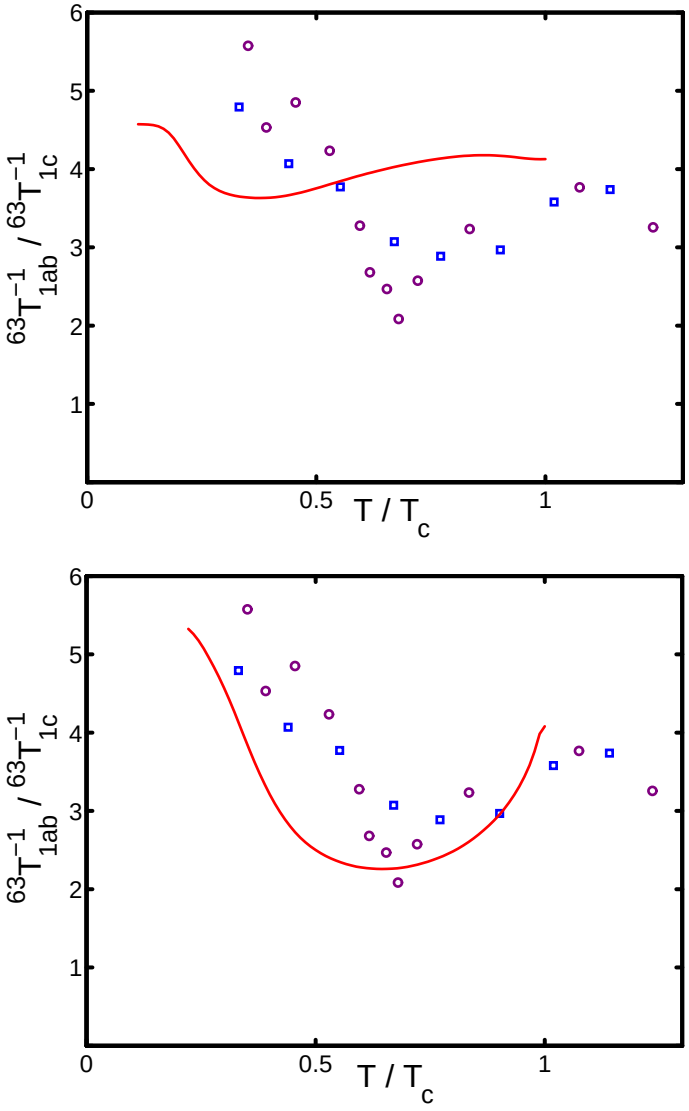

Figure 33: Temperature dependence of the anisotropy ratio ${}^{63}T_{1ab}^{-1}/{}^{63}T_{1c}^{-1}$ for s–wave (top) and d–wave (bottom) gap symmetries. The experimental points are taken from [78] for $YBa_2Cu_3O_7$ (squares) and [2] for $YBa_2Cu_4O_8$ (circles).

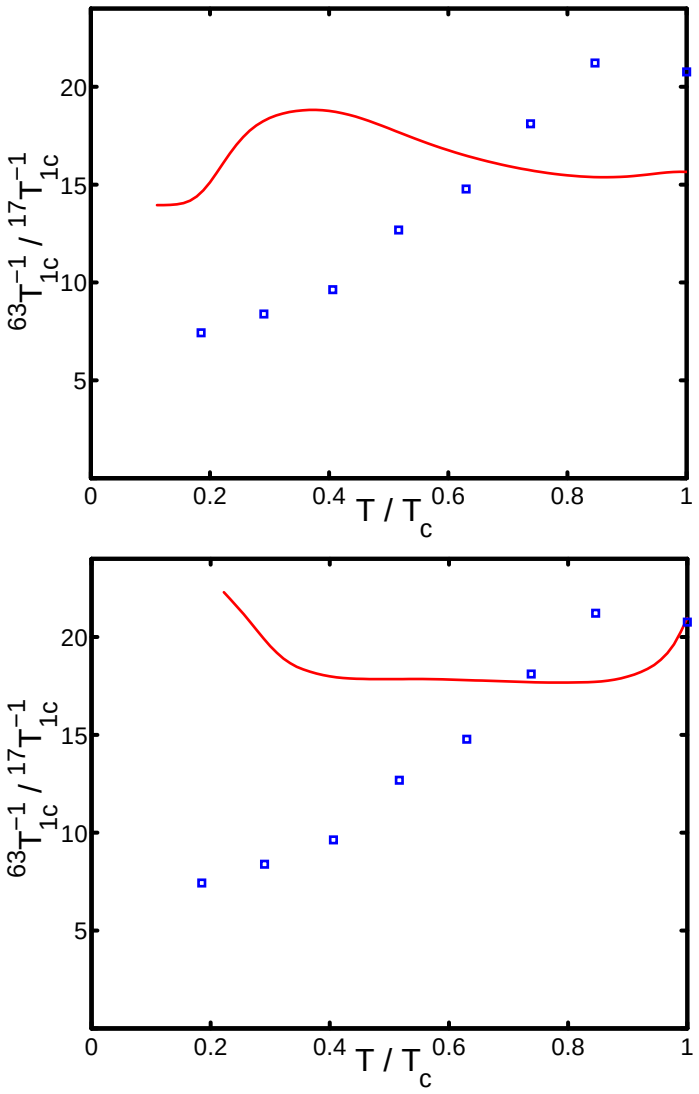

Figure 34: Temperature dependence of the anisotropy ratio ${}^{63}T_{1c}^{-1}/{}^{17}T_{1c}^{-1}$ in $YBa_2Cu_3O_7$ for s–wave (top) and d–wave (bottom) gap symmetries. The experimental points are taken from [51].

5.4 Summary of results for the RPA approximation

In Figures 35 and 36 we summarize our results for the RPA susceptibility with s–wave and d–wave gap symmetries.

First we would like to consider the conventional s–wave gap symmetry. By examination of Figure 35 we observe that it is possible to account for most of the experimental results with an s–wave gap symmetry. However, there are many problems and inconsistencies which must be addressed. First of all, to account for the neutron scattering experiments, a large effective interaction $U_e \simeq 0.4$ eV must be assumed. This is in contrast with NMR results, which seems to suggest a near zero effective interaction U_e. The second problem lies in the choice of the quasiparticle scattering rate Γ. To account for the observed experimental results one must assume a very large value for the quasiparticle scattering rate. Such large values are inconsistent both with experiments and with theoretical estimates of this quantity [20, 66]. For small values of the scattering rate, a Hebel–Slichter peak in the spin–lattice relaxation rate appears and the spin–spin relaxation rate decreases rapidly upon entering the superconducting state. Such behavior is in contradiction with experimental results. Furthermore we found it impossible to account for both the observed field direction ${}^{63}T_{1ab}^{-1}/{}^{63}T_{1c}^{-1}$ and nuclei anisotropies ${}^{63}T_{1c}^{-1}/{}^{17}T_{1c}^{-1}$, utilizing the conventional s–wave gap symmetry.

Let us now turn to the examination of the results, obtained with a d–wave gap symmetry (Figure 36). We conclude that it is possible to account for all of the observed experimental phenomena, save the large anisotropy ${}^{63}T_{1c}^{-1}/{}^{17}T_{1c}^{-1}$. Contrary to the s–wave gap case, we could fit all the experiments with one set of parameters. These are $\Delta_0 = 22$ meV ($\pm 10\%$) and $U_e = 0.11$ eV ($\pm 10\%$). For this optimal set of parameters, both neutron scattering and NMR experiments can be explained simultaneously. However, the quasiparticle scattering rate must be assumed as rather small. We would like to point out that such small values of the scattering rate also contradict previous estimates of this parameter [20, 66]. In these works an estimated value of $\Gamma = k_B T_c (T/T_c)^3$ was found. In our calculation we determined that Γ should be approximately a magnitude smaller to account for the experiments. Unfortunately, direct measurement of the scattering rate is not possible, therefore we simply cannot know the real value of this quantity.

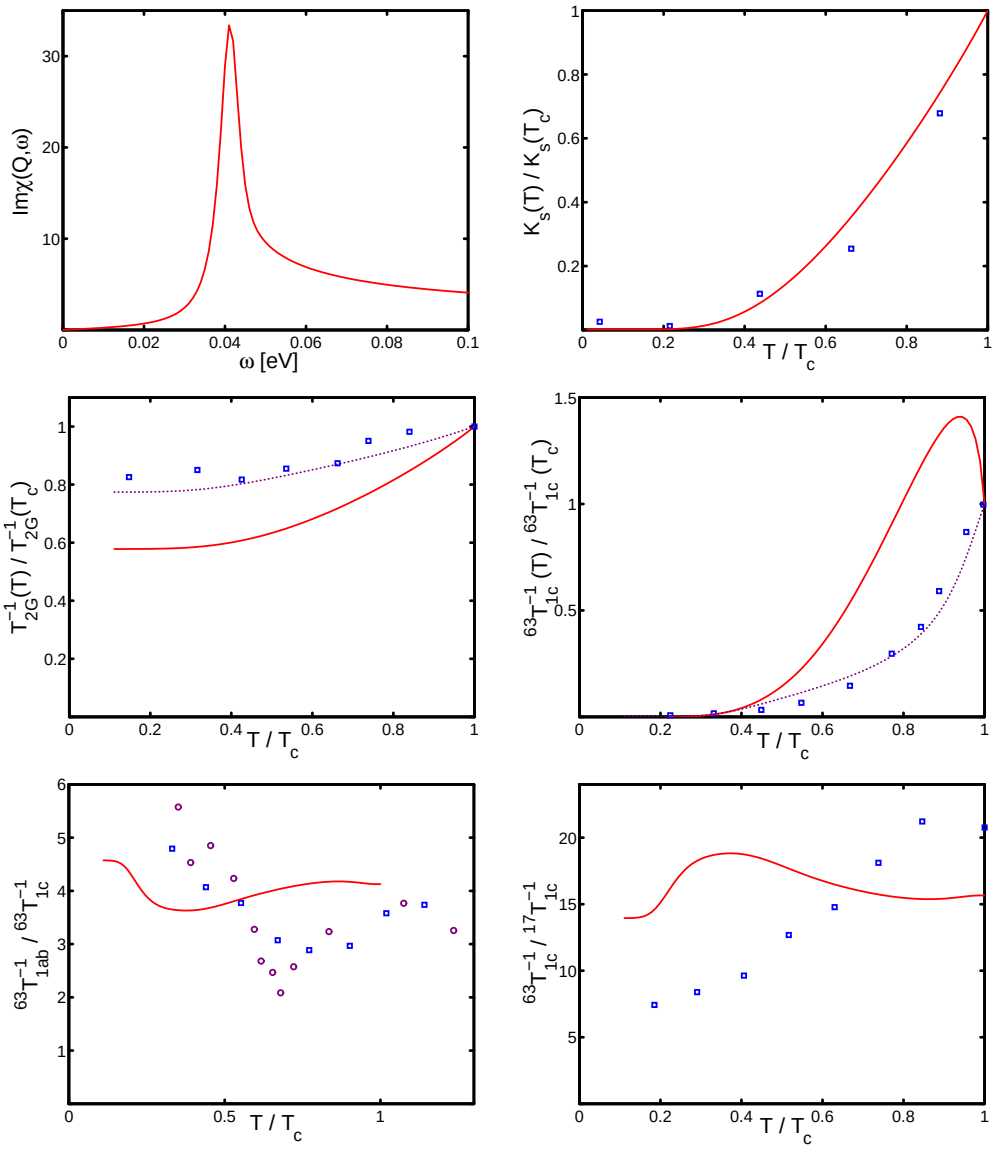

Figure 35: Summary of results, RPA susceptibility with a conventional s–wave gap symmetry. The experiments could not be fitted with the same set of parameters, therefore for each experiment the best fit result is shown. The dotted lines correspond to large quasiparticle scattering rates.

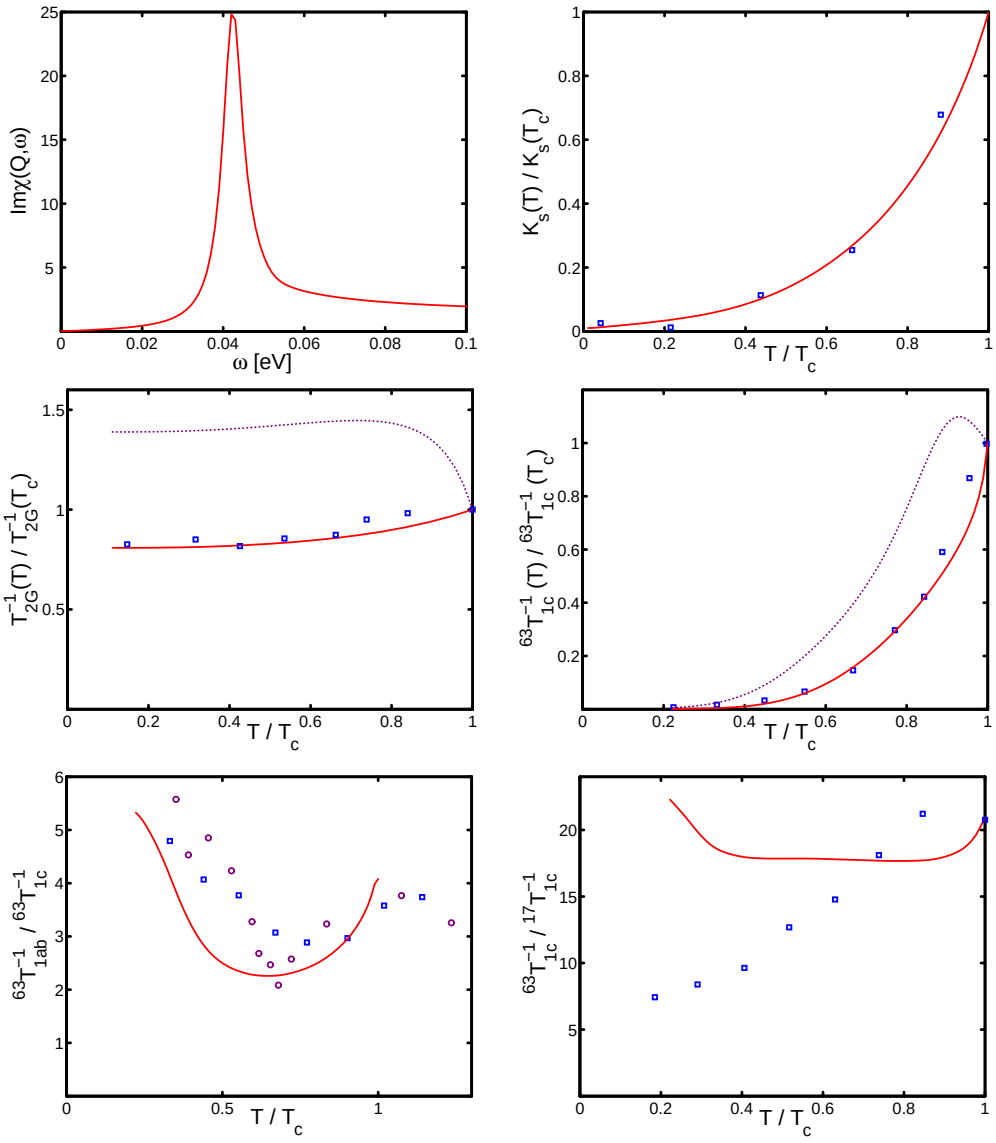

Figure 36: Summary of results, RPA susceptibility with d–wave gap symmetry. The common parameters are $\Delta_0 = 22$ meV ($\pm 10\%$) and $U_e = 0.11$ eV ($\pm 10\%$). The dotted lines correspond to large quasiparticle scattering rates.

6 Results for the singlet–band model

In the forthcoming sections we will analyze neutron scattering and NMR experiments with the help of the susceptibility determined in the singlet–correlated band model. The expression for the susceptibility is given as

$$\chi(\mathbf{q},\omega) = \frac{\chi_0(\mathbf{q},\omega)}{1 + J_{\mathbf{q}}\chi_0(\mathbf{q},\omega) + \Pi(\mathbf{q},\omega) + Z(\mathbf{q},\omega)},$$

where $\chi_0(\mathbf{q},\omega)$ is the susceptibility in the BCS theory according to equation (38), $\Pi(\mathbf{q},\omega)$ and $Z(\mathbf{q},\omega)$ are functions which correspond to strong correlation effects. Furthermore, the superexchange interaction of the copper spins is given by $J_{\mathbf{q}} = J_1(\cos q_x + \cos q_y)$. The evaluation of the spin susceptibility expression was carried out numerically by a trapezoidal integration over the first Brillouin zone.

In our analysis we will proceed similarly as for the RPA susceptibility. We assume the Fermi surface as given from fits to photoemission data. Then as before, we analyze neutron scattering experiments in order to determine the approximate values of the fit parameters in the model. Finally, we move to NMR experiments and try to calculate the temperature dependence of Knight shift, spin–lattice relaxation and spin–spin relaxation rates. Generally, we expect our results to be similar to those obtained before in the RPA approximation. In particular, the new expression for the susceptibility closely resembles the formula in the random–phase approximation scheme. The numerator contains the BCS susceptibility and the denominator is an enhancement term. The role of the factor $U_e\chi_0(\mathbf{q},\omega)$ in the RPA expression is taken over by $(J_{\mathbf{q}}\chi_0(\mathbf{q},\omega) + \Pi(\mathbf{q},\omega) + Z(\mathbf{q},\omega))$, where the effective interaction parameter U_e is replaced by the superexchange interaction $J_{\mathbf{q}}$. Our analysis of the RPA susceptibility showed that in order to describe neutron scattering and NMR simultaneously, a $d_{x^2-y^2}$–wave gap symmetry must be assumed. Consequently, we will consider only the $d_{x^2-y^2}$–wave gap symmetry in our following calculations, since all the other possible gap symmetries could already be excluded by the analysis of the RPA susceptibility.

6.1 Parameters for the calculation

In this section we reconsider the parameters, which are needed to perform our calculations. First we would like to discuss the parameters which determine

	Set 1 [60]	Set 2 [60]	Set 3 [28]	Set 4 [29]
t_1 [eV]	0.21	0.1981	0.235	0.211
t_2 [eV]	-0.0522	-0.0473	-0.0252	-0.0343
t_3 [eV]	-0.0034	-0.0047	0.0523	0.0466
t_4 [eV]	0.0463	0.066	0.0221	0.0181
t_5 [eV]	-0.0025	-0.0094	-0.0153	-0.0335
μ [eV]	0.1197	0.0879	0.1129	0.0989
δ	0.42	0.4	0.41	0.4

Table 3: Tight binding parameters for the singlet–band model.

the band structure. Similarly to the RPA susceptibility before, our tight binding band structure is given as

$$\begin{aligned}
\varepsilon_{\mathbf{k}} &= P2t_1\left(\cos k_x + \cos k_y\right) \\
&+ P4t_2\left(\cos k_x \cos k_y\right) \\
&+ P2t_3\left(\cos 2k_x + \cos 2k_y\right) \\
&+ P2t_4\left(\cos 2k_x \cos k_y + \cos 2k_y \cos k_x\right) \\
&+ P4t_5\left(\cos 2k_x \cos 2k_y\right) - \mu,
\end{aligned}$$

where in comparison to the RPA theory a new doping dependent factor $P = (1+\delta)/2$ appears. Furthermore, since we are in the hole representation the sign of the kinetic energy is changed (see Section 3.1.3). The parameters $t_1 ... t_5$ are taken from photoemission experiments [28, 29, 60]. They are summarized in Table 3. By comparison with the parameters given before in Table 2 on page 46 we see that the absolute values of the hopping terms are slightly changed, due to the factor P. These parameters still describe the same Fermi surface topology as before, however now for the holes, instead of the electrons. The corresponding band structures are given in Figure 37.

Next we would like to comment on the gap parameter Δ_0. The value of this parameter is not affected by the change of the band structure, thus we take $\Delta_0 \simeq 20 - 50$ meV. The renormalized Coulomb interaction parameter U_e from the RPA approximation is not present in the singlet–band model. Instead, we have the superexchange interaction of the copper spins

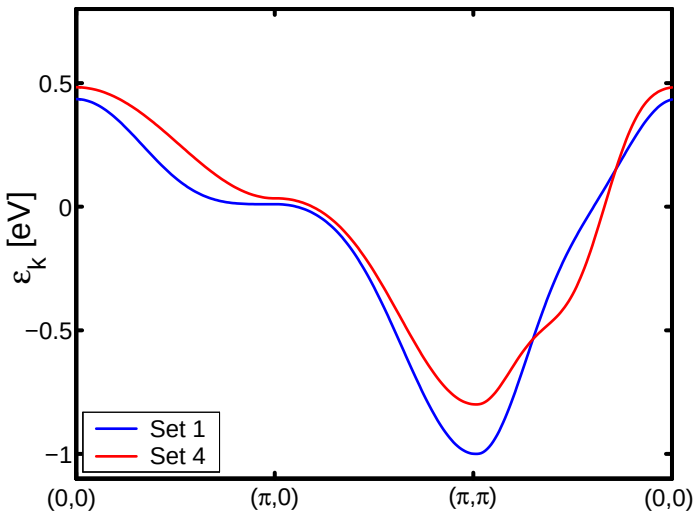

Figure 37: Band structures of $YBa_2Cu_3O_7$ (set 1, blue) and $Bi_2Sr_2CaCu_2O_8$ (set 4, red) according to photoemission experiments.

$J_{\mathbf{q}} = J_1 (\cos q_x + \cos q_y)$, where $J_1 \simeq 0 - 400$ meV. Previously in the RPA approach we used a temperature dependent quasiparticle scattering rate $\Gamma \simeq k_B T_c (T/T_c)^3$ adopted following the assumption of Bulut and Scalapino [14]. This strong temperature dependence leads to a value of Γ smaller than 0.1 meV, for which the imaginary parts of $\Pi(\mathbf{q}, \omega)$ and $Z(\mathbf{q}, \omega)$ could not be evaluated because of convergence problems. Thus in our calculations we take a small constant broadening $\Gamma \simeq 1 - 3$ meV.

We summarize our choices for the parameters:

- The hopping terms $t_1 ... t_5$ are taken from the same photoemission experiments as for the RPA susceptibility.
- The gap parameter Δ_0 is allowed to vary, within the values of $\Delta_0 \simeq 20 - 50$ meV.
- The quasiparticle scattering rate Γ will be taken as a constant broadening $\Gamma \simeq 1 - 3$ meV.
- The superexchange interaction parameter is assumed as $J_1 \simeq 0 - 400$ meV.

6.2 Neutron scattering in $YBa_2Cu_3O_7$

In order to describe neutron scattering in $YBa_2Cu_3O_7$, we remind on the conclusions we have reached previously for the BCS susceptibility in Section 3.1.1. We are interested in these results because in the numerator of the new singlet–band susceptibility expression, the BCS susceptibility $\chi_0(\mathbf{q},\omega)$ appears.

In the region where the imaginary part of $\chi_0(\mathbf{Q},\omega)$ is small, the factor $(1 + J_{\mathbf{q}}\chi_0(\mathbf{q},\omega) + \Pi(\mathbf{q},\omega) + Z(\mathbf{q},\omega))$ can enhance the singlet–band susceptibility and creates a large peak as observed by inelastic neutron scattering experiments [8, 58]. For the extended s–wave and d_{xy}–wave gap symmetries there is no transparency window in $\chi_0(\mathbf{q},\omega)$, thus the susceptibility cannot be enhanced. For both the conventional s–wave and the $d_{x^2-y^2}$–wave gap symmetries, however, a neutron resonance peak can be obtained by adjustment of the parameter values. Analysis of NMR experiments (see Figure 36 on page 78) shows that the gap parameter Δ_0 should be the smallest possible. Keeping this in mind we begin our calculation of the neutron resonance peak in $YBa_2Cu_3O_7$, utilizing a $d_{x^2-y^2}$–wave gap symmetry. For simplicity we take the same hopping parameters as for the RPA susceptibility, i.e. set 1 from Table 3.

In Figure 38 the imaginary part of the singlet–band susceptibility is shown at the antiferromagnetic wave vector $\mathbf{Q}$, for different values of the superexchange interaction parameter J_1. We observe that the position of the peak depends on the parameter J_1 in a similar manner as for U_e in case of the RPA susceptibility. Upon increasing the value of J_1, the peak shifts to lower frequencies and enhances due to the increasingly smaller values of the BCS susceptibility $\chi_0(\mathbf{Q},\omega)$. Comparison with Figure 19 on page 53 shows that the position of the peak is less sensitive to the parameter J_1 than it was to U_e in the weak coupling limit. We associate this behavior to the strong correlation functions $\Pi(\mathbf{q},\omega)$ and $Z(\mathbf{q},\omega)$ in the denominator of the susceptibility. We also note that, contrary to the RPA susceptibility, a small enhancement exists even if $J_1 \simeq 0$ eV, due to the presence of the strong correlation functions.

Let us now turn to the examination of the behavior of the imaginary part of the susceptibility for frequencies $\omega < 41$ meV. In Figure 39 we display the imaginary part of the susceptibility near the antiferromagnetic wave vector $\mathbf{Q}$, calculated for different frequencies. We observe that, upon decreasing the

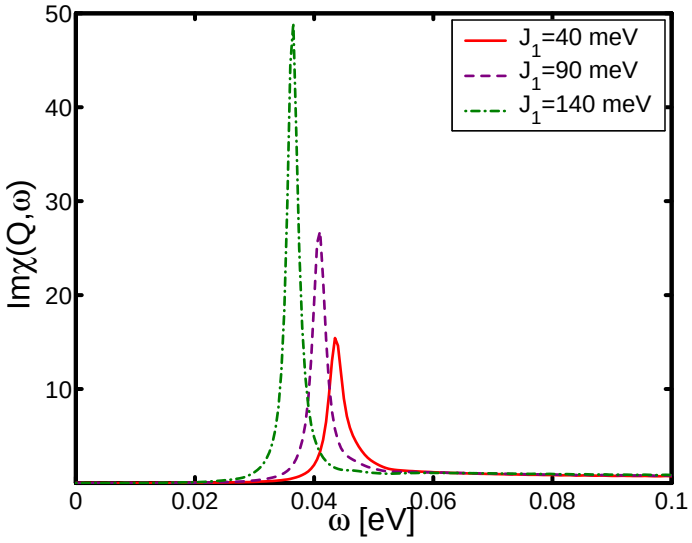

Figure 38: Imaginary part of the susceptibility $Im\chi\left(\mathbf{Q},\omega\right)$ for various values of J_1. The gap parameter is $\Delta_0 = 24$ meV and the damping is $\Gamma = 1.5$ meV.

frequency ω, the peak which was originally located at $\mathbf{Q}$ is shifted and separated into four distinct parts. This behavior is consistent with experimental observations [35, 84].

In Figure 40 we display our best fit result for neutron scattering in the framework of the singlet–band susceptibility. Our fit parameters are determined to be $\Delta_0 = 24$ meV and $J_1 = 0.09$ eV. In the figure we also display $Im\chi\left(\left(q_x,\pi\right),\omega\right)$ as a function of q_x and ω. The experimentally reported downward dispersion branch [68] with respect to ω is clearly recognizable in the figure. We would like to point out that for the conventional s–wave gap symmetry and generally for the RPA susceptibility this dispersion branch is completely missing.

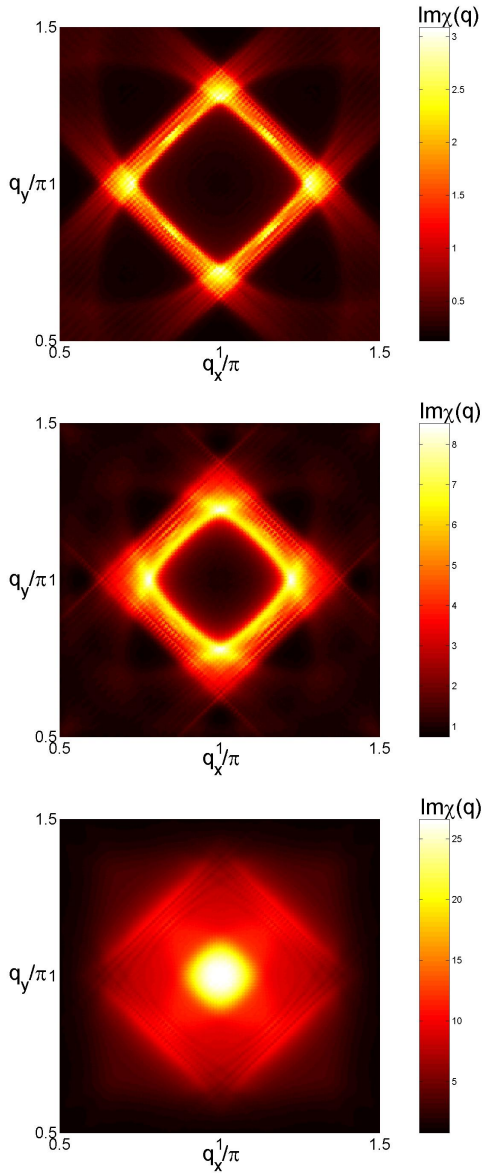

Figure 39: Imaginary part of the susceptibility $Im\chi\left(\mathbf{q},\omega\right)$ around the antiferromagnetic wave vector $\mathbf{Q}$ for $YBa_2Cu_3O_7$. Results for different frequencies $\omega = 29$, 35, 41 meV (top to bottom) are shown.

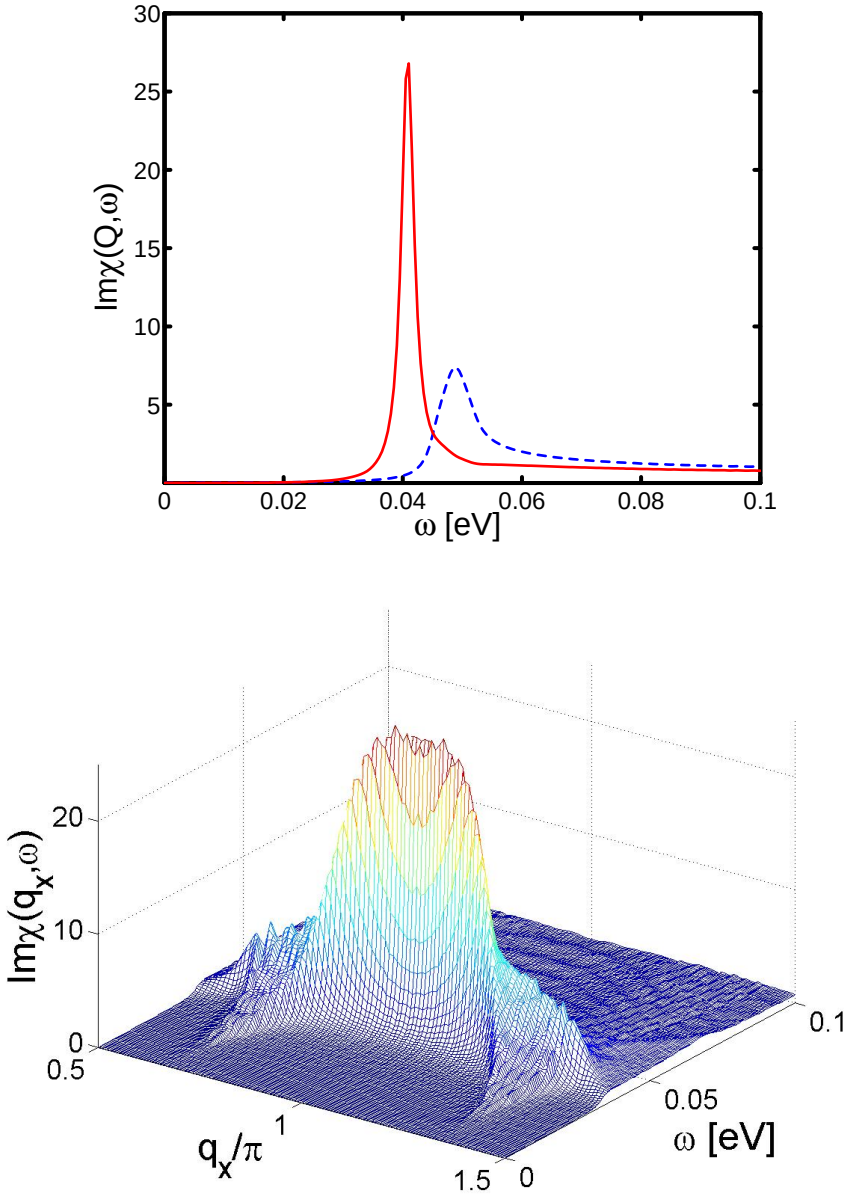

Figure 40: Imaginary part of the susceptibility $Im\chi\left(\mathbf{q},\omega\right)$ near the antiferromagnetic wave vector $\mathbf{Q}$ for $YBa_2Cu_3O_7$. The parameters are $\Delta_0 = 24$ meV and $J_1 = 0.09$ eV. In the figure on top the imaginary part of the BCS susceptibility $\chi_0\left(\mathbf{Q},\omega\right)$ is also shown (dotted blue line).

6.3 Neutron scattering in $Bi_2Sr_2CaCu_2O_8$

In this section we present the results of our calculations concerning the neutron scattering resonance peak in the material $Bi_2Sr_2CaCu_2O_8$. Unfortunately, the NMR data available for this material is very sparse, making a complete analysis of this high–T_c superconductor impossible. Nevertheless, we try to analyse the available data.

Neutron scattering experimental results indicate a similar behavior as in $YBa_2Cu_3O_7$. The observed magnetic fluctuations are peaked near the antiferromagnetic wave vector $\mathbf{Q}$ [30, 33]. Thus as in $YBa_2Cu_3O_7$, in the imaginary part of the susceptibility $Im\chi(\mathbf{Q},\omega)$ a large peak appears near the frequency $\omega \simeq 40$ meV. In our analysis we proceeded in a similar manner as for $YBa_2Cu_3O_7$ in Section 6.2. We position the peak in $Im\chi(\mathbf{Q},\omega)$ along the ω–axis, by adjusting our fit parameters. Then later we will try to calculate the temperature dependence of the available NMR data in the superconducting state. For our calculation we will use the Fermi surface described by set 4 in Table 3 on page 80. Similar results can be obtained by utilizing set 3.

The behavior of the imaginary part of the susceptibility for frequencies $\omega < 40$ meV is shown in Figure 41. By examination of the figure it is evident that the neutron resonance peak is not separated into four distinct parts at low frequencies as it is in $YBa_2Cu_3O_7$ (cf. Figure 39). To our knowledge[3] the low frequency behaviour of the magnetic excitations has not been measured in $Bi_2Sr_2CaCu_2O_8$, thus we have no basis for comparison with experiments, yet.

In Figure 42 we show the calculated imaginary part of the susceptibility at the antiferromagnetic wave vector $\mathbf{Q}$. We observe a large peak near the frequency $\omega \simeq 40$ meV. The fit parameters are determined as $\Delta_0 = 26$ meV and $J_1 = 300$ meV. These parameters are quite different from those we used to fit the experiments in $YBa_2Cu_3O_7$. In particular, the value of the superexchange interaction parameter $J_1 = 300$ meV is approximately three times larger than that for $YBa_2Cu_3O_7$. We associate this difference to the different Fermi surface topology of these two materials (see Figure 15 on page 48). Furthermore we would like to point out that the experimentally reported and in our model reproduced downward dispersion branch [68] of $YBa_2Cu_3O_7$ is no longer found when applying our model to $Bi_2Sr_2CaCu_2O_8$.

[3] The only known measurement [57] is inconclusive due to experimental difficulty.

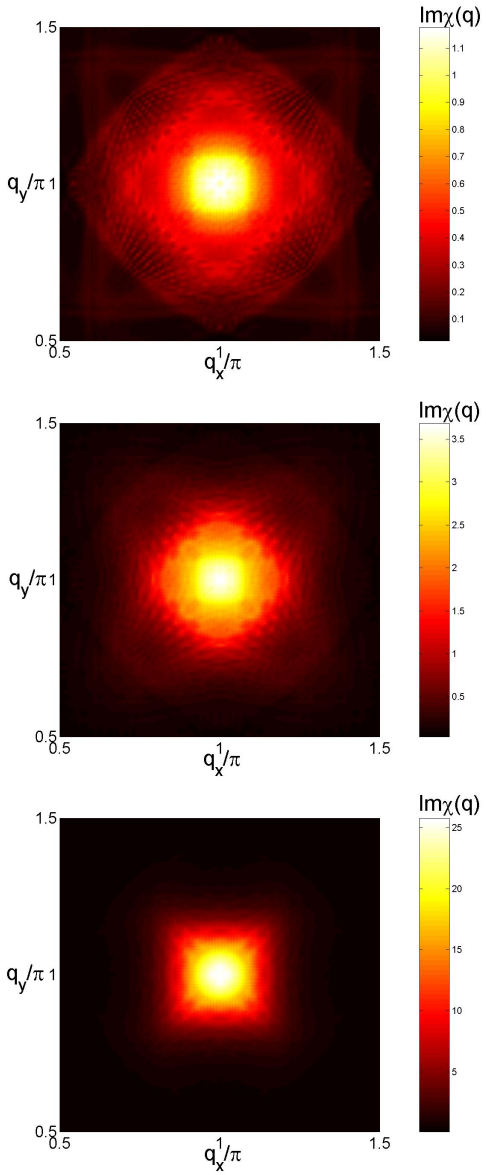

Figure 41: Imaginary part of the susceptibility $Im\chi(\mathbf{q},\omega)$ around the antiferromagnetic wave vector $\mathbf{Q}$ for $Bi_2Sr_2CaCu_2O_8$. Results for different frequencies $\omega = 30$, 35, 40 meV (top to bottom) are shown.

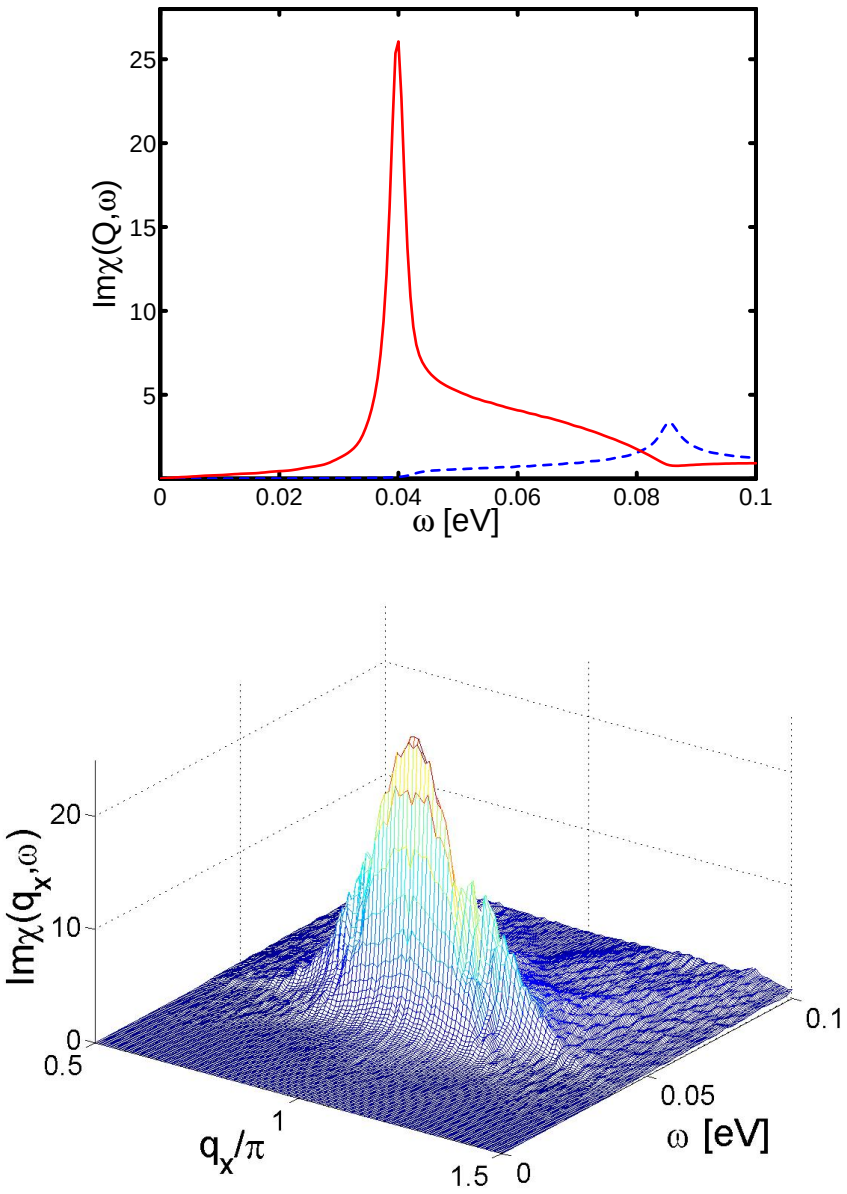

Figure 42: Imaginary part of the spin susceptibility $Im\chi\left(\mathbf{q},\omega\right)$ near the antiferromagnetic wave vector $\mathbf{Q}$ for $Bi_2Sr_2CaCu_2O_8$. In the figure on top the imaginary part of the BCS susceptibility $\chi_0\left(\mathbf{Q},\omega\right)$ is also shown (dotted blue line). The parameters used for the calculation are $\Delta_0 = 26$ meV and $J_1 = 300$ meV.

6.4 NMR in $YBa_2Cu_3O_7$

6.4.1 Knight shift

In order to calculate the Knight shift in the superconducting state we need to approximate the susceptibility in the limit $\mathbf{q} \to 0$, $\omega = 0$. The BCS susceptibility $\chi_0(\mathbf{q}, \omega)$ converts to the Yosida [85] result

$$\chi_0(\mathbf{q} \to 0, \omega = 0) \simeq \frac{P\beta}{N} \sum_{\mathbf{k}} \frac{\partial f(E_{\mathbf{k}})}{\partial E_{\mathbf{k}}}.$$

The functions $\Pi(\mathbf{q}, \omega)$ and $Z(\mathbf{q}, \omega)$ are approximated as

$$\begin{aligned} \Pi(\mathbf{q} \to 0, \omega = 0) &\simeq \frac{1}{N} \sum_{\mathbf{k}} f(E_{\mathbf{k}}) - \frac{P\beta}{N} \sum_{\mathbf{k}} t_{\mathbf{k}} \frac{\partial f(E_{\mathbf{k}})}{\partial E_{\mathbf{k}}} \\ &\simeq \frac{\delta}{P} - \frac{P\beta}{N} \sum_{\mathbf{k}} t_{\mathbf{k}} \frac{\partial f(E_{\mathbf{k}})}{\partial E_{\mathbf{k}}} \end{aligned}$$

and

$$Z(\mathbf{q} \to 0, \omega = 0) \simeq P.$$

The susceptibility converts to the simple expression

$$\chi(\mathbf{q} \to 0, \omega = 0) = \frac{\chi_0(\mathbf{q} \to 0, \omega = 0)}{1 + P + \frac{\delta}{P} + \left(2J_1 - \frac{\mu}{P}\right) \chi_0(\mathbf{q} \to 0, \omega = 0)}.$$

With the help of this expression the Knight shift can be calculated according to equation (83) on page 41. Similarly to the RPA case before, we calculate the temperature dependence of the normalized spin shift $K_s(T)/K_s(T_c)$.

In Figure 43 we display the calculated temperature dependence of the spin shifts for no superexchange interaction $J_1 = 0$ eV and different values of the gap parameter Δ_0. We observe that below T_c the spin shifts depend strongly on the magnitude of the gap parameter Δ_0. This behavior has also been found for the RPA susceptibility (cf. Figure 21 on page 57).

Let us now consider how the spin shift depends on the superexchange interaction $J_{\mathbf{q}}$. In Figure 44 we display calculated Knight shifts for different values

of the superexchange interaction parameter J_1. We see that the temperature dependence of the Knight shift does not significantly change by adjusting the parameter J_1. Also, contrary to the RPA scenario, the parameter J_1 reduces the rapid decrease of the Knight shift. By analysis of the figure we conclude that the optimal set of parameters to describe the experimentally observed temperature dependence of the Knight shift is $\Delta_0 = 24$ meV and $J_1 = 90$ meV for the given Fermi surface. We notice that these values are the same as the fit parameters used to describe neutron scattering in the previous section.

We see that it is possible to account for both the neutron scattering resonance peak and the temperature dependence of the Knight shift in the superconducting state within the same set of parameters. Next, we calculate the temperature dependence of dynamical NMR quantities, the spin–spin and spin–lattice relaxation times.

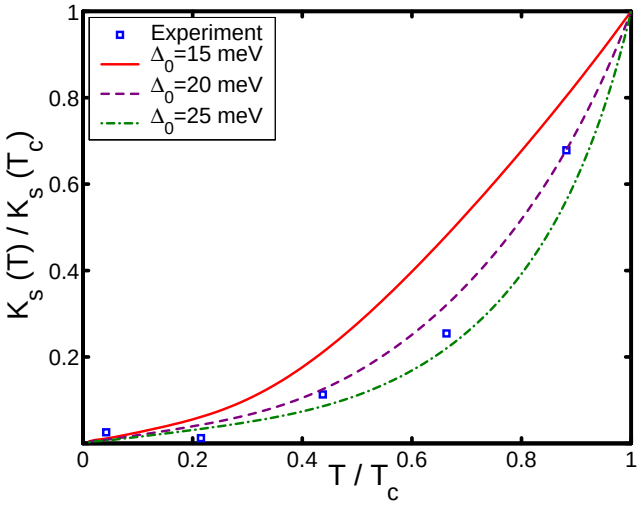

Figure 43: Spin shifts in the superconducting state of $YBa_2Cu_3O_7$ for different values of the gap parameter Δ_0. The experimental points are taken from [3].

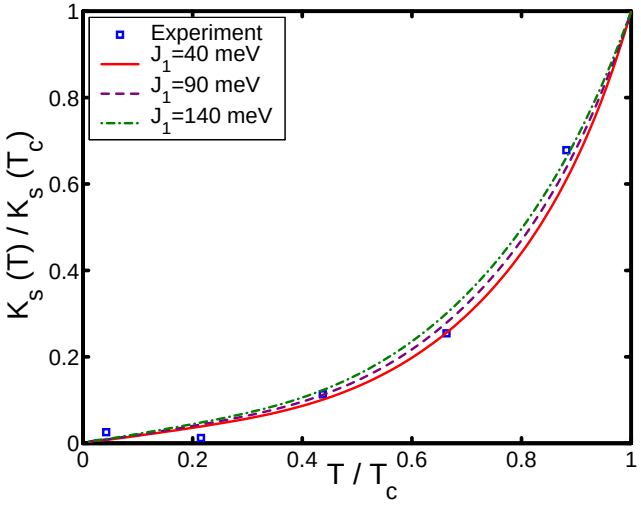

Figure 44: Spin shifts in the superconducting state of $YBa_2Cu_3O_7$ for different values of the superexchange interaction parameter J_1. The gap parameter is $\Delta_0 = 24$ meV. The experimental points are taken from [3].

6.4.2 Spin–spin relaxation

The nuclear spin–spin relaxation rate is calculated according to equation (85) on page 42

$$T_{2G}^{-2} \propto \left[\frac{1}{N} \sum_{\mathbf{q}} F(\mathbf{q})^2 Re\chi(\mathbf{q}, \omega = 0)^2 - \left(\frac{1}{N} \sum_{\mathbf{q}} F(\mathbf{q}) Re\chi(\mathbf{q}, \omega = 0) \right)^2 \right],$$

where $F(\mathbf{q})$ denotes the hyperfine form factors. The values of the hyperfine coupling constants are taken as $A_{\parallel} \simeq -4B$ and $B \simeq 0.4\ \mu$eV. For the calculation of the spin–spin relaxation rate we need to calculate the real part of the susceptibility $Re\chi(\mathbf{q}, \omega = 0)$. We proceed similarly as for the Knight shifts and take the quasiparticle damping $\Gamma \to 0^+$. Otherwise, due to the behavior of the coherence factors, in the spin–spin relaxation rate a large increase near T_c occurs upon entering the superconducting state, see Figure 28 on page 66 or [81].

In Figure 45 we display the calculated spin–spin relaxation rates for no superexchange interaction $J_1 = 0$ eV. We observe that the results show a similar temperature dependence as in the RPA approach (cf. Figure 26 on page 64). Generally, the spin–spin relaxation rate is less sensitive to the change of the gap parameter than the Knight shift or the spin–lattice relaxation. Next we wish to study the behavior of the spin–spin relaxation for different values of the superexchange interaction parameter J_1.

In Figure 46 the temperature dependence of the spin–spin relaxation rate is shown, for various values of the superexchange interaction parameter J_1. We see that we get a reasonable agreement with experimental observation using the parameter values $\Delta_0 = 22$ meV and $J_1 = 90$ meV. The magnitudes of these parameters are in agreement with those obtained by the analysis of neutron scattering experiments in Section 6.2.

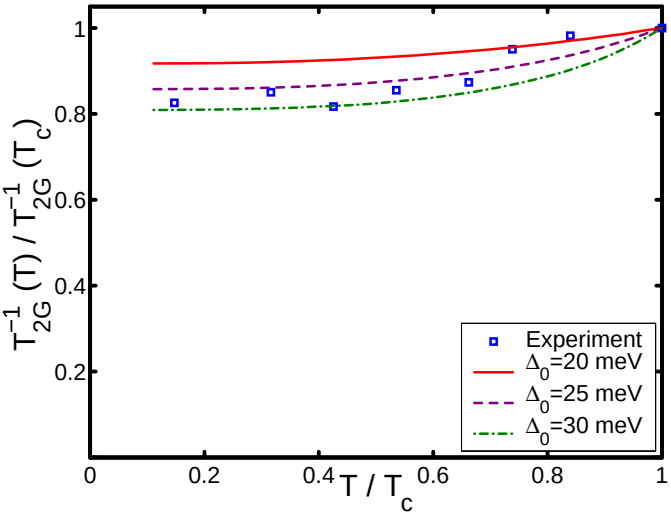

Figure 45: Spin–spin relaxation rate in the superconducting state of $YBa_2Cu_3O_7$ for different values of the gap parameter Δ_0. The experimental points are taken from [75].

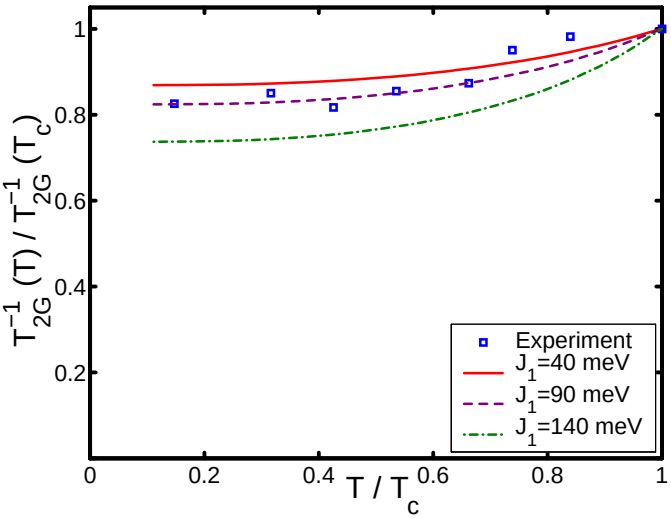

Figure 46: Spin–spin relaxation rate in the superconducting state of $YBa_2Cu_3O_7$ for different values of the superexchange parameter J_1. The gap parameter is $\Delta_0 = 22$ meV. The experimental points are taken from [75].

6.4.3 Spin–lattice relaxation

The nuclear spin–lattice relaxation rate is calculated according to equation (84) on page 42

$$ {}^{\alpha}T_{1\beta}^{-1} \propto \frac{T}{N} \sum_{\mathbf{q},\beta'} {}^{\alpha}F_{\beta'}(\mathbf{q}) \lim_{\omega \to 0} \frac{Im\chi(\mathbf{q},\omega)}{\omega}. $$

In order to calculate the imaginary part of the susceptibility $Im\chi(\mathbf{q}, \omega \to 0)$, a finite quasiparticle broadening was introduced. We take a similar value as for neutron scattering calculations $\Gamma = 2$ meV. The values of the hyperfine coupling constants are taken as $A_{\parallel} \simeq -4B$, $A_{\perp} \simeq 0.75B$, $C_{\parallel} \simeq 0.6B$, $C_{\perp} \simeq 0.32B$ and $B \simeq 0.4$ μeV. The values of these constants are under debate [43, 67, 87], therefore we assume an uncertainty of 20% for these values.

In Figure 47 we display the calculated spin–lattice relaxation rates for no superexchange interaction $J_1 = 0$ eV. We observe that the temperature dependence varies strongly when adjusting the gap parameter Δ_0. This is in accordance with RPA results (cf. Figure 30 on page 71).

Next we switch on the superexchange parameter J_1. In Figure 48 the spin–lattice relaxation rate is shown for different values of J_1. We see that upon changing the values of J_1 the spin–lattice relaxation rate T_{1c}^{-1} acts the same way as in the RPA case for the parameter U_e (cf. Figure 31 on page 72). Namely, the parameter J_1 has no significant impact on the temperature dependence of the spin–lattice relaxation rate in the superconducting state. Upon further examination of the figure we see that we get a reasonable agreement with experimental observation using the parameter values $\Delta_0 = 22$ meV and $J_1 = 90$ meV. These parameters agree with our previous calculations.

We are also interested in the anisotropy ratios ${}^{63}T_{1ab}^{-1}/{}^{63}T_{1c}^{-1}$ and ${}^{63}T_{1c}^{-1}/{}^{17}T_{1c}^{-1}$. Experimental evidence points toward a field dependence of these quantities. In particular, large anisotropies were reported in weak external fields. We display the calculated anisotropy ratios in Figure 49. We see that one can account for the anisotropy ratio ${}^{63}T_{1ab}^{-1}/{}^{63}T_{1c}^{-1}$, but it is not possible to reproduce the temperature dependence of the anisotropy ratio ${}^{63}T_{1c}^{-1}/{}^{17}T_{1c}^{-1}$. These results also agree with RPA calculations (see Figure 33 on page 74 and Figure 34 on page 75).

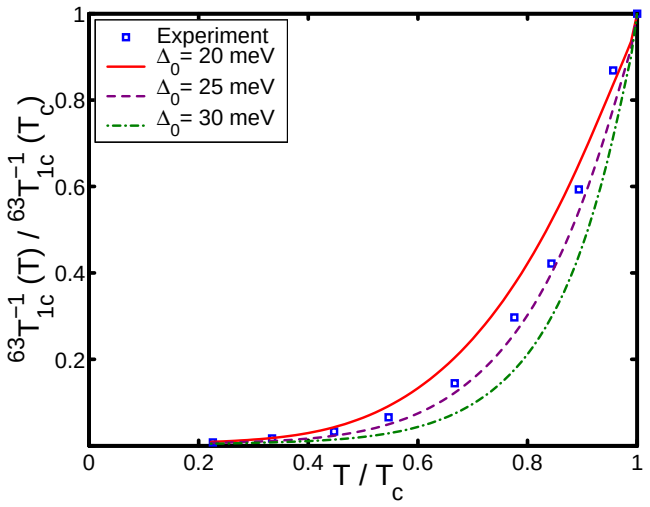

Figure 47: Spin–lattice relaxation rate in the superconducting state of $YBa_2Cu_3O_7$ for no interaction $J_1 = 0$ eV. The quasiparticle scattering rate is $\Gamma = 2$ meV. The experimental points are taken from [79].

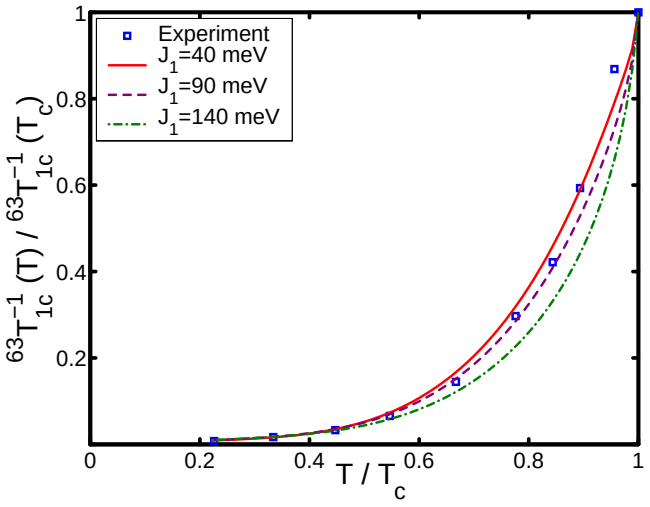

Figure 48: Spin–lattice relaxation rate in the superconducting state of $YBa_2Cu_3O_7$ for different values of the superexchange interaction parameter J_1. The gap parameter is $\Delta_0 = 22$ meV and the quasiparticle scattering rate is $\Gamma = 2$ meV. The experimental points are taken from [79].

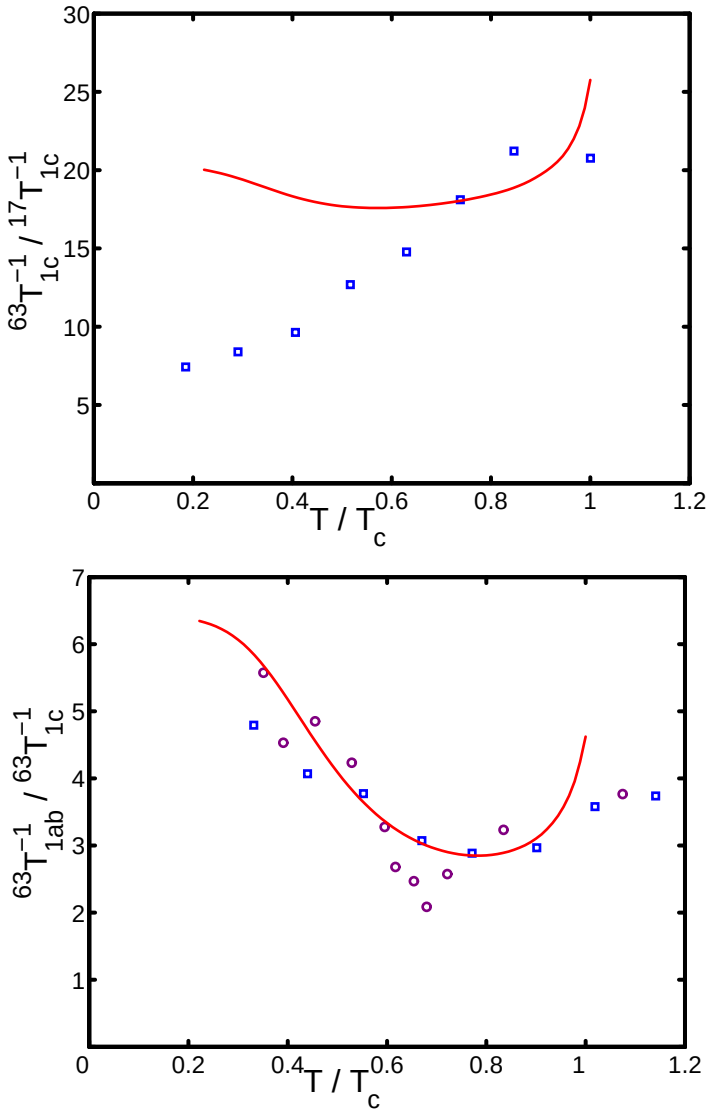

Figure 49: Temperature dependence of the anisotropy ratios ${}^{63}T_{1c}^{-1}/{}^{17}T_{1c}^{-1}$ and ${}^{63}T_{1ab}^{-1}/{}^{63}T_{1c}^{-1}$ in $YBa_2Cu_3O_7$. The experimental points for ${}^{63}T_{1c}^{-1}/{}^{17}T_{1c}^{-1}$ are taken from [51], whereas for ${}^{63}T_{1ab}^{-1}/{}^{63}T_{1c}^{-1}$ they are taken from [78] for $YBa_2Cu_3O_7$ (squares) and from [2] for $YBa_2Cu_4O_8$ (circles). The parameters are $\Delta_0 = 22$ meV and $J_1 = 90$ meV.

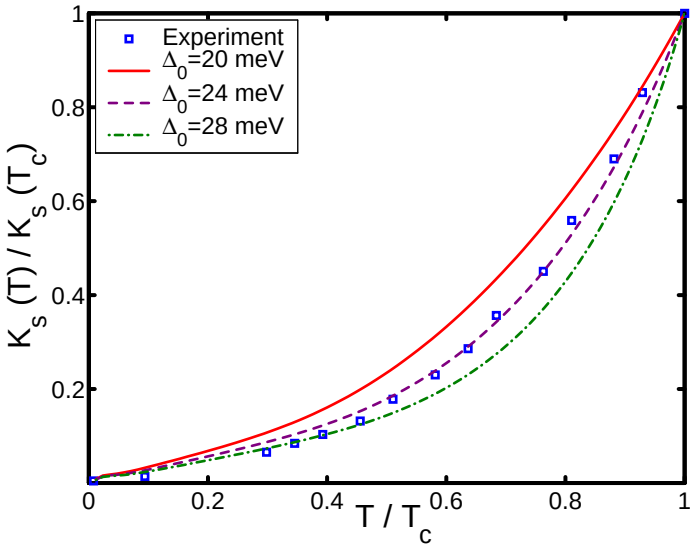

Figure 50: Spin shifts in the superconducting state of $Bi_2Sr_2CaCu_2O_8$. The superexchange parameter is $J_1 = 300$ meV. The experimental points are taken from [44].

6.5 NMR in $Bi_2Sr_2CaCu_2O_8$

6.5.1 Knight shift

In order to calculate the Knight shift in $Bi_2Sr_2CaCu_2O_8$ we use the approximations obtained in Section 6.4.1. The calculated spin shifts are shown in Figure 50. We see that we get a reasonable fit to data by using almost the same parameter set as for neutron scattering (cf. Figure 42 on page 88). These fit parameters are given by $\Delta_0 = 24$ meV and $J_1 = 300$ meV. By examination of the figure we observe that, similarly to $YBa_2Cu_3O_7$, the gap parameter Δ_0 has a considerable influence on the temperature dependence of the Knight shift. Furthermore we conclude that with the chosen set of parameters the calculated Knight shifts fit the experimental results nicely, even at low temperatures T$<$ 20 K.

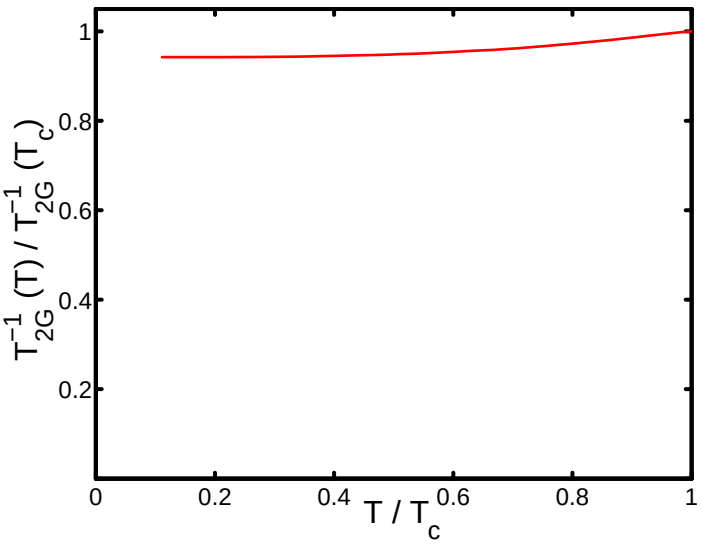

Figure 51: Spin–spin relaxation rate in the superconducting state of $Bi_2Sr_2CaCu_2O_8$. The parameters are $\Delta_0 = 24$ meV and $J_1 = 300$ meV.

6.5.2 Spin–spin relaxation

To our knowledge the spin–spin relaxation rate in $Bi_2Sr_2CaCu_2O_8$ has not yet been measured. Here we present a theoretical result based on the parameter values determined by the analysis of Knight shift experiments. These are given as $\Delta_0 = 24$ meV and $J_1 = 300$ meV. The calculated spin–spin relaxation rate is shown in Figure 51. We see that there is little difference with respect to the calculated spin–spin relaxation rate in $YBa_2Cu_3O_7$ (cf. Figure 46 on page 93).

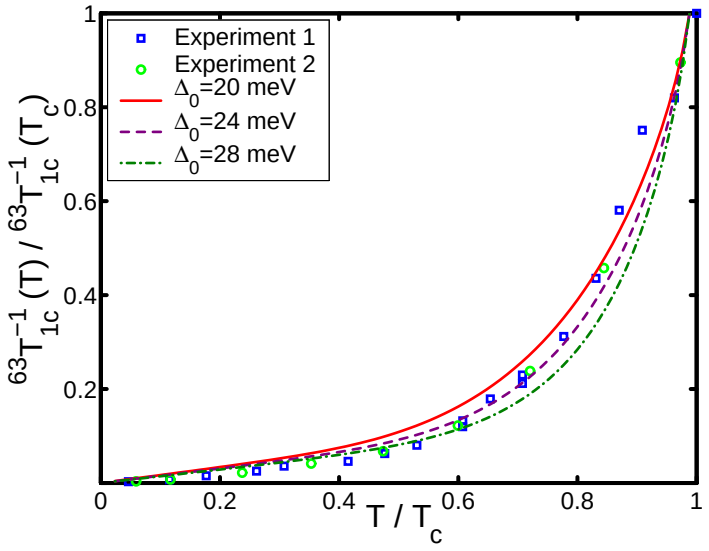

Figure 52: Spin–lattice relaxation rate in the superconducting state of $Bi_2Sr_2CaCu_2O_8$. The superexchange interaction parameter is $J_1 = 300$ meV and the quasiparticle scattering rate is $\Gamma = 2$ meV. The two sets of experimental points are taken from [44, 77].

6.5.3 Spin–lattice relaxation

The spin–lattice relaxation rate has been calculated in a similar manner than for $YBa_2Cu_3O_7$ in Section 6.4.3. We assume that the hyperfine fields are the same for both materials. In Figure 52 we display the calculated spin–lattice relaxation rates for $Bi_2Sr_2CaCu_2O_8$. We see that the calculated spin–lattice relaxation gives an acceptable fit to the experiments. The best fit parameters are $\Delta_0 = 24$ meV and $J_1 = 300$ meV. Particularly interesting is the low temperature behavior of the spin–lattice relaxation confirmed in two independent experiments (see the figure). Contrary to $YBa_2Cu_3O_7$ (cf. Figure 48 on page 95), for which the spin–lattice relaxation rate practically vanishes at low temperatures, the relaxation in $Bi_2Sr_2CaCu_2O_8$ has a small value even at T=10 K. By closer examination of the figure we see that the calculated spin–lattice relaxation rates match the experimental observation.

6.6 Summary of results for the singlet–band model

In Figures 53 and 54 we summarize our findings for the singlet–band susceptibility with $d_{x^2-y^2}$–wave gap symmetry.

First we would like to discuss the results for $YBa_2Cu_3O_7$. By examination of Figure 53 we observe that it is possible to account for most of the experimental results with a d–wave gap symmetry. The calculated temperature dependence of the Knight shift, spin–spin and spin–lattice relaxation rates as well as inelastic neutron scattering all give satisfactory agreement to the experimental data. The optimal set of parameters (OSP) is determined as $\Delta_0 = 23$ meV ($\pm 5\%$) , $J_1 = 90$ meV. We see that it is possible to account for the experimental observations, within 5% accuracy of the fit parameters. The parameter Γ, which characterizes the lifetime of the quasiparticles is assumed as constant $\Gamma \simeq 1 - 2$ meV.

Let us now turn to the examination of the results obtained for the material $Bi_2Sr_2CaCu_2O_8$, see Figure 54. The available experimental data, i.e. neutron scattering data, Knight shift data and spin–lattice relaxation data all could be fitted within the same set of parameters, using a d–wave gap symmetry and a parametrized Fermi surface from photoemission experiments. Note that our neutron scattering calculations indicate that, in comparison with $YBa_2Cu_3O_7$, the downward dispersion branch is missing (compare Figure 40 on page 85 with Figure 42 on page 88) and that the magnetic excitations remain peaked exactly at $\mathbf{Q} = (\pi, \pi)$ even at low frequencies (compare Figure 39 on page 84 with Figure 41 on page 87). These results could be further tested experimentally.

A particularly interesting feature can be found when comparing the spin–lattice relaxation rates in $YBa_2Cu_3O_7$ and $Bi_2Sr_2CaCu_2O_8$ at low temperatures. A close inspection of the corresponding figures (bottom left panels in Figure 53 and 54) shows that in the former case ${}^{63}T_{1c}^{-1}(T)$ vanishes at temperatures T$<$20 K, while in the latter case the relaxation rate seems to vanish only at T$\simeq$ 0 K. Note that both of these dependences are reproduced by the model calculations. In Figure 54 we also display our theoretical predictions for the spin–spin relaxation rate as well as the anisotropy ratio ${}^{63}T_{1ab}^{-1}/{}^{63}T_{1c}^{-1}$. The spin–spin relaxation rate exhibit a similar behavior as in $YBa_2Cu_3O_7$, whereas the temperature dependence of the anisotropy ratio ${}^{63}T_{1ab}^{-1}/{}^{63}T_{1c}^{-1}$ is less pronounced. The OSP for this material is found to be $\Delta_0 = 25$ meV ($\pm 5\%$) , $J_1 = 300$ meV.

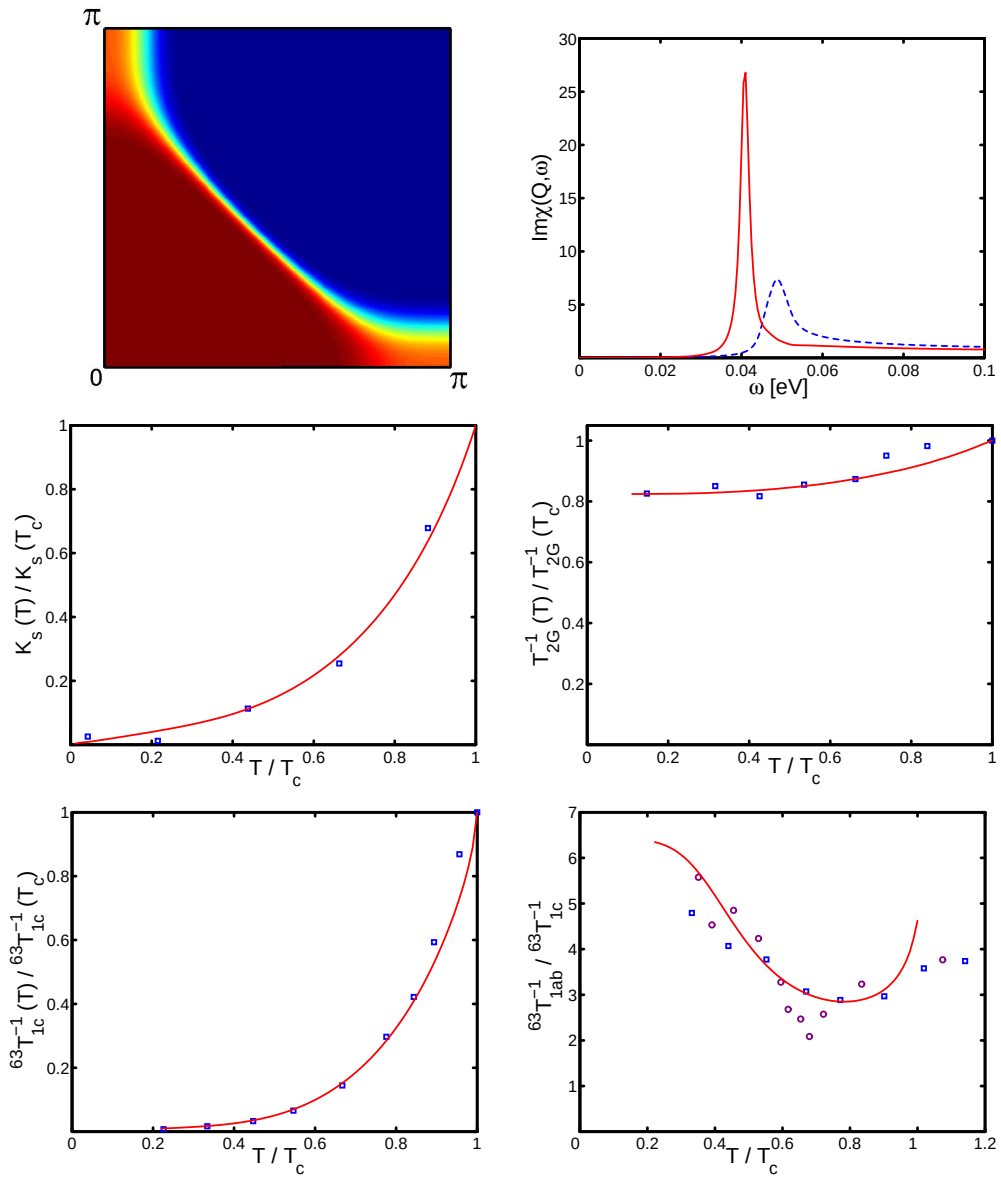

Figure 53: Summary of results for $YBa_2Cu_3O_7$, the common parameters are $\Delta_0 = 23$ meV ($\pm 5\%$) , $J_1 = 90$ meV.

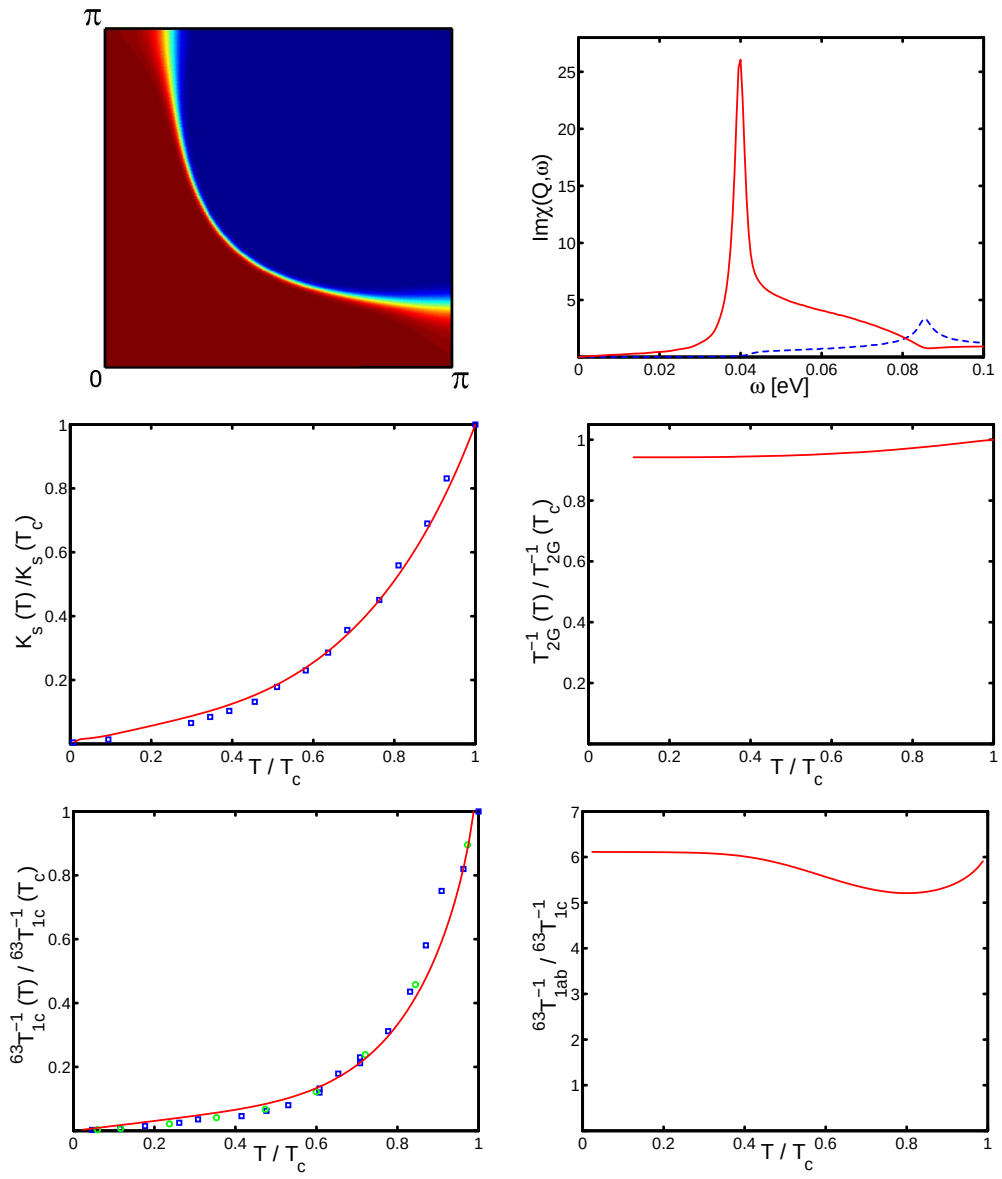

Figure 54: Summary of results for $Bi_2Sr_2CaCu_2O_8$, the common parameters are $\Delta_0 = 25$ meV ($\pm 5\%$) , $J_1 = 300$ meV.

7 Summary and Conclusions

In the first part of this work a special Hubbard model proposed by M. Eremin for cuprate superconductors was introduced and discussed. It has been found that the susceptibility in the strong coupling limit is different from the standard Pauli–Lindhard formula. In particular, two correction functions were determined in the superconducting state. The first one, $\Pi(\mathbf{q},\omega)$, originates from the anticommutator rule which is modified due to the Coulomb repulsion (equation (28)) and was already found by Hubbard and Jain [42] in the normal state, whereas the function $Z(\mathbf{q},\omega)$ has its origin in the fast fluctuations of the localized spins and was previously discussed by Zavidonov and Brinkmann [86] for the normal state.

In the second part we analyzed neutron scattering and NMR data in the superconducting state of $YBa_2Cu_3O_7$, by utilizing the spin susceptibility in the conventional RPA form. All of the basic pairing symmetries that are allowed by group theory were discussed, including conventional s–wave, extended s–wave, d_{xy}–wave and $d_{x^2-y^2}$–wave gap symmetries. By comparison with experiments it has been found that all of the possible gap symmetries can be discarded, save the $d_{x^2-y^2}$–wave symmetry. In particular, the extended s–wave and the d_{xy}–wave symmetries could be excluded by the analysis of inelastic neutron scattering experiments in the superconducting state.

As concerns the conventional s–wave pairing symmetry it was shown that theoretically it is possible to account for some of the experimental data utilizing a very special set of parameters. However, there are several problems associated with this particular symmetry. In the case of neutron scattering we found it possible to account for the experimental observation of a large peak in the imaginary part of the susceptibility at $\omega \simeq 41$ meV. On the other hand, special experimental features like the downward dispersion with respect to ω, could not be reproduced. For the case of NMR it was also possible to account for most of the experimental results. However, there were many problems and inconsistencies. The calculated Knight shift with conventional s–wave symmetry vanishes at low temperatures in contradiction with experiments. The experimentally measured temperature dependence of the nuclear spin–spin and spin–lattice relaxation could only be reproduced by assuming a very large value of the quasiparticle lifetime. The temperature dependence of the anisotropy ratios could not be explained at all. Also the parameter set for which the NMR experiments could be fitted does not match the values

obtained for neutron scattering. All these inconsistencies have lead us to the conclusion that the analysis of all experimental data within the present model strongly favor a pairing with $d_{x^2-y^2}$–wave symmetry.

In the third part of this work the spin susceptibility in the strong coupling limit was evaluated, assuming a $d_{x^2-y^2}$–wave gap symmetry. Neutron scattering and NMR data for the materials $YBa_2Cu_3O_7$ and $Bi_2Sr_2CaCu_2O_8$ were analyzed. We found that on the whole the results with strong coupling and weak coupling limit agree with each other. Based on our results we conclude that strong correlation effects, i.e. the effect of the functions $\Pi(\mathbf{q},\omega)$, $Z(\mathbf{q},\omega)$ on the susceptibility can be included in the weak coupling approach by an appropriate redefinition [23, 24] of the effective Coulomb interaction parameter U_e.

We found it possible to describe the available experimental data in the optimally doped $YBa_2Cu_3O_7$ and $Bi_2Sr_2CaCu_2O_8$ with one set of model parameters for each material and with taking into account the Fermi surface topology of these compounds.

Unit [eV]	t_1	t_2	t_3	t_4	t_5	$\Delta_0 \pm 5\%$	J_1
$YBa_2Cu_3O_7$	0.21	−0.0522	−0.0034	0.0463	−0.0025	0.023	0.09
$Bi_2Sr_2CaCu_2O_8$	0.211	−0.0343	0.0466	0.0181	−0.0335	0.025	0.3

Table 4: Optimal set of parameters for $YBa_2Cu_3O_7$ and $Bi_2Sr_2CaCu_2O_8$.

These optimal sets of parameters are summarized in Table 4. The difference in the parameter values are related to the very different Fermi surfaces of these two materials. The most important parameter in our calculations turned out to be the gap parameter Δ_0. In particular, for inelastic neutron scattering this parameter determines the scale of the transparency window in the BCS susceptibility, thus the possible position of the experimentally observed large peak in the imaginary part of the susceptibility near $\omega \simeq 41$ meV. In NMR the calculated temperature dependences of the Knight shift, spin–spin and spin–lattice relaxation rate all depend very strongly on the gap parameter. We would also like to point out that our fitted values for the gap parameter agree with estimates made by means of analysis of photoemission experiments [46].

In conclusion we have determined the spin susceptibility in cuprates within a

special Hubbard model which includes strong correlation effects. We analyzed inelastic neutron scattering and NMR data in the superconducting state of the optimally doped high–T_c superconductors $YBa_2Cu_3O_7$ and $Bi_2Sr_2CaCu_2O_8$. In our analysis we have taken into account the experimentally measured topology of the Fermi surface, which is quite different for these two materials. The remarkable fact that by utilizing the measured Fermi surface, all these experiments can be explained within almost the same values of the fit parameters in both $YBa_2Cu_3O_7$ and $Bi_2Sr_2CaCu_2O_8$ indicates that a very interesting connection has been found between surface and bulk experiments.

Selected Notations

$c^{\dagger}_{\mathbf{k},\sigma}$ $(c_{\mathbf{k},\sigma})$	:	creation (annihilation) operator for an electron in the Hubbard model.
$d^{\dagger}_{\mathbf{k},\sigma}$ $(d_{\mathbf{k},\sigma})$	:	creation (annihilation) operator for a hole in the Hubbard model.
$a^{\dagger}_{\mathbf{k},\sigma}$ $(a_{\mathbf{k},\sigma})$	:	creation (annihilation) operator for an electron in the BCS theory.
$\psi^{pd,\sigma}_{\mathbf{k}}\left(\psi^{\sigma,pd}_{\mathbf{k}}\right)$	:	composite creation (annihilation) operator for copper–oxygen singlet states.
$\alpha^{\dagger}_{\mathbf{k},\sigma}$ $(\alpha_{\mathbf{k},\sigma})$	:	Bogoliubov's quasiparticle operator.
$X^{\alpha,\beta}$	:	Hubbard projection operator.
P	:	doping dependent factor in the singlet–band model.
U	:	Coulomb repulsion in the Hubbard model.
U_e	:	effective Coulomb interaction parameter in the RPA approach.
$J_{\mathbf{q}}$	:	superexchange interaction of the copper spins.
Δ_0	:	gap parameter in the superconducting state.
$\chi_0(\mathbf{q},\omega)$	:	dynamical spin susceptibility in the BCS theory.
$\chi(\mathbf{q},\omega)$	:	dynamical spin susceptibility.

Appendix A

The derivation of the susceptibility is organized as follows. First, we write down a complete set of equations of motion using the composite copper–oxygen creation (annihilation) operators $\psi_i^{pd,\sigma}\left(\psi_i^{\sigma,pd}\right)$ of the copper–oxygen singlet states in the plane. Then, by means of a linear transformation we rearrange these equations via Bogoliubov's quasiparticle operators into new sets of equations, which finally will be solved. An expression for the susceptibility was previously derived [22] by utilizing the method of the Heisenberg equation of motion in a small magnetic field. The advantage of the Green's function method is that it allows to obtain a formula for the susceptibility which contains both the itinerant (or quasi Fermi–liquid) part and the local spin fluctuation part in one general expression. The spin operator for the singlet–correlated band is written as

$$S_{\mathbf{q}}^{+}=\sum_{\mathbf{k}}S_{\mathbf{k},\mathbf{q}}^{+}=\sum_{\mathbf{k}}\left(\psi_{\mathbf{k}}^{\uparrow,0}+\psi_{\mathbf{k}}^{pd,\downarrow}\right)\left(\psi_{\mathbf{k+q}}^{0,\downarrow}-\psi_{\mathbf{k+q}}^{\uparrow,pd}\right)\simeq-\sum_{\mathbf{k}}\psi_{\mathbf{k}}^{pd,\downarrow}\psi_{\mathbf{k+q}}^{\uparrow,pd}.$$

Here we have neglected all the quasiparticle operators corresponding to the low Hubbard sub–band, because it is assumed to be completely filled.

The starting equation for the Green's function in the normal state T>T_c is written as [25]

$$\begin{aligned}\omega\left\langle\left\langle-\psi_{\mathbf{k}}^{pd,\downarrow}\psi_{\mathbf{k+q}}^{\uparrow,pd}\left|S_{-\mathbf{q}}^{-}\right.\right\rangle\right\rangle=\frac{i}{2\pi}\left(\left\langle\psi_{\mathbf{k}}^{pd,\downarrow}\psi_{\mathbf{k}}^{\downarrow,pd}\right\rangle-\left\langle\psi_{\mathbf{k+q}}^{pd,\uparrow}\psi_{\mathbf{k+q}}^{\uparrow,pd}\right\rangle\right)\\-\left(\varepsilon_{\mathbf{k}}-\varepsilon_{\mathbf{k+q}}\right)\left\langle\left\langle-\psi_{\mathbf{k}}^{pd,\downarrow}\psi_{\mathbf{k+q}}^{\uparrow,pd}\left|S_{-\mathbf{q}}^{-}\right.\right\rangle\right\rangle\\+\frac{1}{N}\left\{\left(J_{\mathbf{q}}-t_{\mathbf{k}}\right)\left\langle\psi_{\mathbf{k}}^{\downarrow,pd}\psi_{\mathbf{k}}^{pd,\downarrow}\right\rangle\right.\\\left.-\left(J_{\mathbf{q}}-t_{\mathbf{k+q}}\right)\left\langle\psi_{\mathbf{k+q}}^{pd,\uparrow}\psi_{\mathbf{k+q}}^{\uparrow,pd}\right\rangle\right\}\left\langle\left\langle S_{\mathbf{q}}^{+}\left|S_{-\mathbf{q}}^{-}\right.\right\rangle\right\rangle\\+\frac{P}{N}\sum_{\mathbf{k}'}\left(t_{\mathbf{k}'+\mathbf{q}}-t_{\mathbf{k}'}\right)\left\langle\left\langle\psi_{\mathbf{k}'}^{pd,\downarrow}\psi_{\mathbf{k}'+\mathbf{q}}^{\uparrow,pd}\left|S_{-\mathbf{q}}^{-}\right.\right\rangle\right\rangle,\end{aligned}\tag{87}$$

where $J_{\mathbf{q}}=J_1\left(\cos q_x+\cos q_y\right)$.

In addition to equation (87) we write the following equation

$$\omega\left\langle\left\langle S_{\mathbf{q}}^{+}\left|S_{-\mathbf{q}}^{-}\right.\right\rangle\right\rangle=\sum_{\mathbf{k}'}\left(t_{\mathbf{k}'}-t_{\mathbf{k}'+\mathbf{q}}\right)\left\langle\left\langle\psi_{\mathbf{k}'}^{pd,\downarrow}\psi_{\mathbf{k}'+\mathbf{q}}^{\uparrow,pd}\left|S_{-\mathbf{q}}^{-}\right.\right\rangle\right\rangle\tag{88}$$

$$+\sum_{\mathbf{k}'}\left(t_{\mathbf{k}'+\mathbf{q}}-t_{\mathbf{k}'}\right)\left\langle\left\langle\psi^{\uparrow,0}_{\mathbf{k}'}\psi^{0,\downarrow}_{\mathbf{k}'+\mathbf{q}}\left|S^{-}_{-\mathbf{q}}\right.\right\rangle\right\rangle$$
$$+\sum_{i,l}J_{il}e^{-i\mathbf{q}\mathbf{R}}\left\langle\left\langle S^{+}_{l}S^{z}_{i}-S^{z}_{l}S^{+}_{i}\left|S^{-}_{-\mathbf{q}}\right.\right\rangle\right\rangle.$$

By the decoupling

$$\left\langle\left\langle S^{+}_{l}S^{z}_{i}\left|S^{-}_{-\mathbf{q}}\right.\right\rangle\right\rangle\simeq\left\langle S^{z}_{i}\right\rangle\left\langle\left\langle S^{+}_{l}\left|S^{-}_{-\mathbf{q}}\right.\right\rangle\right\rangle=0,$$

it is possible to prove that $\left\langle\left\langle\psi^{\uparrow,0}_{\mathbf{k}'}\psi^{0,\downarrow}_{\mathbf{k}'+\mathbf{q}}\left|S^{-}_{-\mathbf{q}}\right.\right\rangle\right\rangle\simeq 0.$

Then if we combine equation (87) and equation (88) we get

$$\begin{aligned}\omega\left\langle\left\langle-\psi^{pd,\downarrow}_{\mathbf{k}}\psi^{\uparrow,pd}_{\mathbf{k}+\mathbf{q}}\left|S^{-}_{-\mathbf{q}}\right.\right\rangle\right\rangle=\frac{i}{2\pi}\left(\left\langle\psi^{pd,\downarrow}_{\mathbf{k}}\psi^{\downarrow,pd}_{\mathbf{k}}\right\rangle-\left\langle\psi^{pd,\uparrow}_{\mathbf{k}+\mathbf{q}}\psi^{\uparrow,pd}_{\mathbf{k}+\mathbf{q}}\right\rangle\right)\\-\left(\varepsilon_{\mathbf{k}}-\varepsilon_{\mathbf{k}+\mathbf{q}}\right)\left\langle\left\langle-\psi^{pd,\downarrow}_{\mathbf{k}}\psi^{\uparrow,pd}_{\mathbf{k}+\mathbf{q}}\left|S^{-}_{-\mathbf{q}}\right.\right\rangle\right\rangle\\+\frac{1}{N}\left\{\left(J_{\mathbf{q}}-t_{\mathbf{k}}\right)\left\langle\psi^{\downarrow,pd}_{\mathbf{k}}\psi^{pd,\downarrow}_{\mathbf{k}}\right\rangle\right.\\\left.-\left(J_{\mathbf{q}}-t_{\mathbf{k}+\mathbf{q}}\right)\left\langle\psi^{pd,\uparrow}_{\mathbf{k}+\mathbf{q}}\psi^{\uparrow,pd}_{\mathbf{k}+\mathbf{q}}\right\rangle\right\}\left\langle\left\langle S^{+}_{\mathbf{q}}\left|S^{-}_{-\mathbf{q}}\right.\right\rangle\right\rangle\\-\frac{P}{N}\omega\left\langle\left\langle S^{+}_{\mathbf{q}}\left|S^{-}_{-\mathbf{q}}\right.\right\rangle\right\rangle.\end{aligned}\tag{89}$$

The equation of motion (89) allows to derive the expression of the susceptibility in the normal state. For the superconducting state we need to construct additionally other equations, which are determined by Bogoliubov's transformation

$$\begin{aligned}\alpha^{pd,\downarrow}_{\mathbf{k}}&=u_{\mathbf{k}}\psi^{pd,\downarrow}_{\mathbf{k}}-v_{\mathbf{k}}\psi^{\uparrow,pd}_{-\mathbf{k}}\\\alpha^{pd,\uparrow}_{\mathbf{k}}&=u_{\mathbf{k}}\psi^{pd,\uparrow}_{\mathbf{k}}+v_{\mathbf{k}}\psi^{\downarrow,pd}_{-\mathbf{k}}.\end{aligned}$$

The spin operator will be written as

$$\begin{aligned}S^{+}_{\mathbf{q}}&=\sum_{\mathbf{k}}S^{+}_{\mathbf{k},\mathbf{q}}\\&=-\sum_{\mathbf{k}}\left(u_{\mathbf{k}+\mathbf{q}}u_{\mathbf{k}}\alpha^{pd,\downarrow}_{\mathbf{k}}\alpha^{\uparrow,pd}_{\mathbf{k}+\mathbf{q}}+v_{\mathbf{k}}u_{\mathbf{k}+\mathbf{q}}\alpha^{\uparrow,pd}_{-\mathbf{k}}\alpha^{\uparrow,pd}_{\mathbf{k}+\mathbf{q}}\right)\\&-\sum_{\mathbf{k}}\left(-u_{\mathbf{k}}v_{\mathbf{k}+\mathbf{q}}\alpha^{pd,\downarrow}_{\mathbf{k}}\alpha^{pd,\downarrow}_{-\mathbf{k}-\mathbf{q}}-v_{\mathbf{k}}v_{\mathbf{k}+\mathbf{q}}\alpha^{\uparrow,pd}_{-\mathbf{k}}\alpha^{pd,\downarrow}_{-\mathbf{k}-\mathbf{q}}\right),\end{aligned}\tag{90}$$

therefore in the superconducting state we need to calculate the following Green's functions

$$\left\langle\left\langle -\alpha_{\mathbf{k}}^{pd,\downarrow}\alpha_{\mathbf{k+q}}^{\uparrow,pd}\left|S_{-\mathbf{q}}^{-}\right.\right\rangle\right\rangle$$
$$\left\langle\left\langle -\alpha_{-\mathbf{k}}^{\uparrow,pd}\alpha_{\mathbf{k+q}}^{\uparrow,pd}\left|S_{-\mathbf{q}}^{-}\right.\right\rangle\right\rangle$$
$$\left\langle\left\langle \alpha_{\mathbf{k}}^{pd,\downarrow}\alpha_{-\mathbf{k-q}}^{pd,\downarrow}\left|S_{-\mathbf{q}}^{-}\right.\right\rangle\right\rangle$$
$$\left\langle\left\langle \alpha_{-\mathbf{k}}^{\uparrow,pd}\alpha_{-\mathbf{k-q}}^{pd,\downarrow}\left|S_{-\mathbf{q}}^{-}\right.\right\rangle\right\rangle.$$

Each one of them we have to express via the $\psi_{\mathbf{k}}^{pd,\sigma}$ operators, for example

$$\begin{aligned}\left\langle\left\langle -\alpha_{\mathbf{k}}^{pd,\downarrow}\alpha_{\mathbf{k+q}}^{\uparrow,pd}\left|S_{-\mathbf{q}}^{-}\right.\right\rangle\right\rangle = \\ -u_{\mathbf{k}}u_{\mathbf{k+q}}\left\langle\left\langle\psi_{\mathbf{k}}^{pd,\downarrow}\psi_{\mathbf{k+q}}^{\uparrow,pd}\right\rangle\right\rangle + v_{\mathbf{k}}u_{\mathbf{k+q}}\left\langle\left\langle\psi_{-\mathbf{k}}^{\uparrow,pd}\psi_{\mathbf{k+q}}^{\uparrow,pd}\right\rangle\right\rangle \\ -u_{\mathbf{k}}v_{\mathbf{k+q}}\left\langle\left\langle\psi_{\mathbf{k}}^{pd,\downarrow}\psi_{-\mathbf{k-q}}^{pd,\downarrow}\right\rangle\right\rangle + v_{\mathbf{k}}v_{\mathbf{k+q}}\left\langle\left\langle\psi_{-\mathbf{k}}^{\uparrow,pd}\psi_{-\mathbf{k-q}}^{pd,\downarrow}\right\rangle\right\rangle.\end{aligned} \tag{91}$$

Doing so we write

$$\begin{aligned}\omega\left\langle\left\langle -\psi_{\mathbf{k}}^{pd,\downarrow}\psi_{\mathbf{k+q}}^{\uparrow,pd}\left|S_{-\mathbf{q}}^{-}\right.\right\rangle\right\rangle = \frac{i}{2\pi}\left(\left\langle\psi_{\mathbf{k}}^{pd,\downarrow}\psi_{\mathbf{k}}^{\downarrow,pd}\right\rangle - \left\langle\psi_{\mathbf{k+q}}^{pd,\uparrow}\psi_{\mathbf{k+q}}^{\uparrow,pd}\right\rangle\right) \\ +\left\langle\left\langle\left[\psi_{-\mathbf{k}}^{pd,\downarrow}\psi_{\mathbf{k+q}}^{\uparrow,pd},H\right]\left|S_{-\mathbf{q}}^{-}\right.\right\rangle\right\rangle_{tr} \\ +\frac{1}{N}\left\{\left(J_{\mathbf{q}}-t_{\mathbf{k}}\right)\left\langle\psi_{\mathbf{k}}^{\downarrow,pd}\psi_{\mathbf{k}}^{pd,\downarrow}\right\rangle\right. \\ \left.-\left(J_{\mathbf{q}}-t_{\mathbf{k+q}}\right)\left\langle\psi_{\mathbf{k+q}}^{pd,\uparrow}\psi_{\mathbf{k+q}}^{\uparrow,pd}\right\rangle\right\}\left\langle\left\langle S_{\mathbf{q}}^{+}\left|S_{-\mathbf{q}}^{-}\right.\right\rangle\right\rangle \\ -\frac{P}{N}\omega\left\langle\left\langle S_{\mathbf{q}}^{+}\left|S_{-\mathbf{q}}^{-}\right.\right\rangle\right\rangle.\end{aligned} \tag{92}$$

This equation has the same form as in the normal state (equation (89)), but now it contains a gap function. Note that a part of the derivation is the same as in the conventional Fermi–liquid theory, were the anticommutator rule is written as $c_{\mathbf{k}\sigma}c_{\mathbf{k}\sigma}^{\dagger} + c_{\mathbf{k}\sigma}^{\dagger}c_{\mathbf{k}\sigma} = 1$. For this reason we write down only the new terms, which appeared on the right hand side of equation (92), due to the spin modulation $S_{\mathbf{q}}^{+}$. The truncated Green's function

$\left\langle\left\langle\left[\psi^{\uparrow,pd}_{\mathbf{k+q}}\psi^{pd,\downarrow}_{\mathbf{k}},H\right]\left|S^{-}_{-\mathbf{q}}\right.\right\rangle\right\rangle_{tr}$ contains all terms, which are present in the weak coupling Fermi–liquid approach, including a gap function. We will calculate them later, after Bogoliubov's transformation in the superconducting state. The next three equations are written as

$$\begin{aligned}\omega\left\langle\left\langle\psi^{\uparrow,pd}_{-\mathbf{k}}\psi^{\uparrow,pd}_{\mathbf{k+q}}\left|S^{-}_{-\mathbf{q}}\right.\right\rangle\right\rangle &= \frac{i}{2\pi}\left(\left\langle\psi^{\uparrow,pd}_{\mathbf{k+q}}\psi^{\downarrow,pd}_{-\mathbf{k-q}}\right\rangle+\left\langle\psi^{\downarrow,pd}_{\mathbf{k}}\psi^{\uparrow,pd}_{-\mathbf{k}}\right\rangle\right)\\ &+\left\langle\left\langle\left[\psi^{\uparrow,pd}_{-\mathbf{k}}\psi^{\uparrow,pd}_{\mathbf{k+q}},H\right]\left|S^{-}_{-\mathbf{q}}\right.\right\rangle\right\rangle_{tr}\\ &-\frac{1}{N}\left\{\left(J_{\mathbf{q}}-t_{\mathbf{k}}\right)\left\langle\psi^{\uparrow,pd}_{-\mathbf{k}}\psi^{\downarrow,pd}_{\mathbf{k}}\right\rangle\right.\\ &\left.+\left(J_{\mathbf{q}}-t_{\mathbf{k+q}}\right)\left\langle\psi^{\downarrow,pd}_{-\mathbf{k-q}}\psi^{\uparrow,pd}_{\mathbf{k+q}}\right\rangle\right\}\left\langle\left\langle S^{+}_{\mathbf{q}}\left|S^{-}_{-\mathbf{q}}\right.\right\rangle\right\rangle\end{aligned}\tag{93}$$

$$\begin{aligned}\omega\left\langle\left\langle\psi^{pd,\downarrow}_{\mathbf{k}}\psi^{pd,\downarrow}_{-\mathbf{k-q}}\left|S^{-}_{-\mathbf{q}}\right.\right\rangle\right\rangle &= -\frac{i}{2\pi}\left(\left\langle\psi^{pd,\downarrow}_{-\mathbf{k-q}}\psi^{pd,\uparrow}_{\mathbf{k+q}}\right\rangle+\left\langle\psi^{pd,\uparrow}_{-\mathbf{k}}\psi^{pd,\downarrow}_{\mathbf{k}}\right\rangle\right)\\ &+\left\langle\left\langle\left[\psi^{pd,\downarrow}_{\mathbf{k}}\psi^{pd,\downarrow}_{-\mathbf{k-q}},H\right]\left|S^{-}_{-\mathbf{q}}\right.\right\rangle\right\rangle_{tr}\\ &+\frac{1}{N}\left\{\left(J_{\mathbf{q}}-t_{\mathbf{k+q}}\right)\left\langle\psi^{pd,\uparrow}_{\mathbf{k+q}}\psi^{pd,\downarrow}_{-\mathbf{k-q}}\right\rangle\right.\\ &\left.+\left(J_{\mathbf{q}}-t_{\mathbf{k}}\right)\left\langle\psi^{pd,\downarrow}_{\mathbf{k}}\psi^{pd,\uparrow}_{-\mathbf{k}}\right\rangle\right\}\left\langle\left\langle S^{+}_{\mathbf{q}}\left|S^{-}_{-\mathbf{q}}\right.\right\rangle\right\rangle\end{aligned}\tag{94}$$

$$\begin{aligned}\omega\left\langle\left\langle\psi^{\uparrow,pd}_{-\mathbf{k}}\psi^{pd,\downarrow}_{-\mathbf{k-q}}\left|S^{-}_{-\mathbf{q}}\right.\right\rangle\right\rangle &= -\frac{i}{2\pi}\left(\left\langle\psi^{pd,\uparrow}_{-\mathbf{k}}\psi^{\uparrow,pd}_{-\mathbf{k}}\right\rangle-\left\langle\psi^{pd,\downarrow}_{-\mathbf{k-q}}\psi^{\downarrow,pd}_{-\mathbf{k-q}}\right\rangle\right)\\ &+\left\langle\left\langle\left[\psi^{\uparrow,pd}_{-\mathbf{k}}\psi^{pd,\downarrow}_{-\mathbf{k-q}},H\right]\left|S^{-}_{-\mathbf{q}}\right.\right\rangle\right\rangle_{tr}\\ &+\frac{1}{N}\left\{\left(J_{\mathbf{q}}-t_{\mathbf{k}}\right)\left\langle\psi^{\uparrow,pd}_{-\mathbf{k}}\psi^{pd,\uparrow}_{-\mathbf{k}}\right\rangle\right.\\ &\left.-\left(J_{\mathbf{q}}-t_{\mathbf{k+q}}\right)\left\langle\psi^{\downarrow,pd}_{-\mathbf{k-q}}\psi^{pd,\downarrow}_{-\mathbf{k-q}}\right\rangle\right\}\left\langle\left\langle S^{+}_{\mathbf{q}}\left|S^{-}_{-\mathbf{q}}\right.\right\rangle\right\rangle\\ &+\frac{1-P}{N}\omega\left\langle\left\langle S^{+}_{\mathbf{q}}\left|S^{-}_{-\mathbf{q}}\right.\right\rangle\right\rangle.\end{aligned}\tag{95}$$

With the help of equations (92), (93), (94) and (95) we construct the following four equations

$$\left(\omega-E_{\mathbf{p}}+E_{\mathbf{k}}\right)\left\langle\left\langle\alpha^{pd,\downarrow}_{\mathbf{k}}\alpha^{\uparrow,pd}_{\mathbf{p}}\left|S^{-}_{-\mathbf{q}}\right.\right\rangle\right\rangle=\frac{i}{2\pi}\left(u_{\mathbf{k}}u_{\mathbf{p}}+v_{\mathbf{k}}v_{\mathbf{p}}\right)\left(n_{\mathbf{p}}-n_{\mathbf{k}}\right)\tag{96}$$

$$+\frac{1}{N}\left(u_{\mathbf{k}}u_{\mathbf{p}}+v_{\mathbf{k}}v_{\mathbf{p}}\right)\left\{\left(J_{\mathbf{q}}-t_{\mathbf{p}}\right)n_{\mathbf{p}}-\left(J_{\mathbf{q}}-t_{\mathbf{k}}\right)n_{\mathbf{k}}\right\}\left\langle\left\langle S_{\mathbf{q}}^{+}\left|S_{-\mathbf{q}}^{-}\right.\right\rangle\right\rangle$$
$$+\left(Pu_{\mathbf{k}}u_{\mathbf{p}}+(P-1)v_{\mathbf{k}}v_{\mathbf{p}}\right)\frac{\omega}{N}\left\langle\left\langle S_{\mathbf{q}}^{+}\left|S_{-\mathbf{q}}^{-}\right.\right\rangle\right\rangle$$

$$\left(\omega-E_{-\mathbf{k}}+E_{-\mathbf{p}}\right)\left\langle\left\langle\alpha_{-\mathbf{k}}^{\uparrow,pd}\alpha_{-\mathbf{p}}^{pd,\downarrow}\left|S_{-\mathbf{q}}^{-}\right.\right\rangle\right\rangle=\frac{i}{2\pi}\left(u_{\mathbf{p}}u_{\mathbf{k}}+v_{\mathbf{p}}v_{\mathbf{k}}\right)\left(n_{-\mathbf{p}}-n_{-\mathbf{k}}\right)\quad(97)$$
$$-\frac{1}{N}\left(u_{\mathbf{p}}u_{\mathbf{k}}+v_{\mathbf{p}}v_{\mathbf{k}}\right)\left\{\left(J_{\mathbf{q}}-t_{\mathbf{p}}\right)\left(P-n_{\mathbf{p}}\right)-\left(J_{\mathbf{q}}-t_{\mathbf{k}}\right)\left(P-n_{-\mathbf{k}}\right)\right\}\left\langle\left\langle S_{\mathbf{q}}^{+}\left|S_{-\mathbf{q}}^{-}\right.\right\rangle\right\rangle$$
$$-\left(Pu_{\mathbf{k}}u_{\mathbf{p}}+(P-1)v_{\mathbf{k}}v_{\mathbf{p}}\right)\frac{\omega}{N}\left\langle\left\langle S_{\mathbf{q}}^{+}\left|S_{-\mathbf{q}}^{-}\right.\right\rangle\right\rangle$$

$$\left(\omega-E_{-\mathbf{k}}-E_{\mathbf{p}}\right)\left\langle\left\langle\alpha_{-\mathbf{k}}^{\uparrow,pd}\alpha_{\mathbf{p}}^{\uparrow,pd}\left|S_{-\mathbf{q}}^{-}\right.\right\rangle\right\rangle=\frac{i}{2\pi}\left(u_{\mathbf{p}}v_{\mathbf{k}}-u_{\mathbf{k}}v_{\mathbf{p}}\right)\left(n_{-\mathbf{k}}+n_{\mathbf{p}}-P\right)\quad(98)$$
$$+\frac{1}{N}\left(u_{\mathbf{p}}v_{\mathbf{k}}-v_{\mathbf{p}}u_{\mathbf{k}}\right)\left\{\left(J_{\mathbf{q}}-t_{\mathbf{p}}\right)n_{\mathbf{k}+\mathbf{q}}-\left(J_{\mathbf{q}}-t_{\mathbf{k}}\right)\left(P-n_{-\mathbf{k}}\right)\right\}\left\langle\left\langle S_{\mathbf{q}}^{+}\left|S_{-\mathbf{q}}^{-}\right.\right\rangle\right\rangle$$
$$+\left(Pu_{\mathbf{p}}v_{\mathbf{k}}-(P-1)u_{\mathbf{k}}v_{\mathbf{p}}\right)\frac{\omega}{N}\left\langle\left\langle S_{\mathbf{q}}^{+}\left|S_{-\mathbf{q}}^{-}\right.\right\rangle\right\rangle$$

$$\left(\omega+E_{\mathbf{k}}+E_{-\mathbf{p}}\right)\left\langle\left\langle\alpha_{\mathbf{k}}^{pd,\downarrow}\alpha_{-\mathbf{p}}^{pd,\downarrow}\left|S_{-\mathbf{q}}^{-}\right.\right\rangle\right\rangle=\frac{i}{2\pi}\left(u_{\mathbf{k}}v_{\mathbf{p}}-u_{\mathbf{p}}v_{\mathbf{k}}\right)\left(n_{-\mathbf{p}}+n_{\mathbf{k}}-P\right)\quad(99)$$
$$+\frac{1}{N}\left(u_{\mathbf{k}}v_{\mathbf{p}}-u_{\mathbf{p}}v_{\mathbf{k}}\right)\left\{\left(J_{\mathbf{q}}-t_{\mathbf{k}}\right)n_{\mathbf{k}}+\left(J_{\mathbf{q}}-t_{\mathbf{p}}\right)\left(P-n_{-\mathbf{p}}\right)\right\}\left\langle\left\langle S_{\mathbf{q}}^{+}\left|S_{-\mathbf{q}}^{-}\right.\right\rangle\right\rangle$$
$$-\left(Pv_{\mathbf{p}}u_{\mathbf{k}}-(P-1)v_{\mathbf{k}}u_{\mathbf{p}}\right)\frac{\omega}{N}\left\langle\left\langle S_{\mathbf{q}}^{+}\left|S_{-\mathbf{q}}^{-}\right.\right\rangle\right\rangle.$$

Here $n_{\mathbf{k}}=\left\langle\alpha_{\mathbf{k}}^{pd,\uparrow}\alpha_{\mathbf{k}}^{\uparrow,pd}\right\rangle=\left\langle\alpha_{\mathbf{k}}^{pd,\downarrow}\alpha_{\mathbf{k}}^{\downarrow,pd}\right\rangle$ are the occupation numbers in the superconducting state. Then we use the identity

$$\begin{aligned}\left\langle\left\langle S_{\mathbf{q}}^{+}\left|S_{-\mathbf{q}}^{-}\right.\right\rangle\right\rangle &= -\sum_{\mathbf{k}}\left(u_{\mathbf{k}+\mathbf{q}}u_{\mathbf{k}}\right)\left\langle\left\langle\alpha_{\mathbf{k}}^{pd,\downarrow}\alpha_{\mathbf{k}+\mathbf{q}}^{\uparrow,pd}\left|S_{-\mathbf{q}}^{-}\right.\right\rangle\right\rangle \\ &+ \sum_{\mathbf{k}}\left(v_{\mathbf{k}+\mathbf{q}}u_{\mathbf{k}}\right)\left\langle\left\langle\alpha_{\mathbf{k}}^{pd,\downarrow}\alpha_{-\mathbf{k}-\mathbf{q}}^{pd,\downarrow}\left|S_{-\mathbf{q}}^{-}\right.\right\rangle\right\rangle \\ &- \sum_{\mathbf{k}}\left(u_{\mathbf{k}+\mathbf{q}}v_{\mathbf{k}}\right)\left\langle\left\langle\alpha_{-\mathbf{k}}^{\uparrow,pd}\alpha_{\mathbf{k}+\mathbf{q}}^{\uparrow,pd}\left|S_{-\mathbf{q}}^{-}\right.\right\rangle\right\rangle \\ &+ \sum_{\mathbf{k}}\left(v_{\mathbf{k}+\mathbf{q}}v_{\mathbf{k}}\right)\left\langle\left\langle\alpha_{-\mathbf{k}}^{\uparrow,pd}\alpha_{-\mathbf{k}-\mathbf{q}}^{pd,\downarrow}\left|S_{-\mathbf{q}}^{-}\right.\right\rangle\right\rangle.\end{aligned}\quad(100)$$

The general expression for the susceptibility is given by

$$\chi^{+-}(\mathbf{q},\omega) = -2\pi i \left\langle\left\langle S^{+}_{\mathbf{q}} \left| S^{-}_{-\mathbf{q}} \right.\right\rangle\right\rangle .$$

With the help of equation (100) (and equations (96)–(99)) it is calculated as

$$\chi(\mathbf{q},\omega) = \frac{\chi_0(\mathbf{q},\omega)}{1 + J_{\mathbf{q}}\chi_0(\mathbf{q},\omega) + \Pi(\mathbf{q},\omega) + Z(\mathbf{q},\omega)},$$

where

$$\begin{aligned}
\chi_0(\mathbf{q},\omega) &= \frac{P}{N}\sum_{\mathbf{k}} \left(x_{\mathbf{k}}x_{\mathbf{k+q}} + y_{\mathbf{k}}y_{\mathbf{k+q}} + 2z_{\mathbf{k}}z_{\mathbf{k+q}}\right) \frac{f_{\mathbf{k+q}} - f_{\mathbf{k}}}{\omega + i\Gamma + E_{\mathbf{k}} - E_{\mathbf{k+q}}} \\
&+ \frac{P}{N}\sum_{\mathbf{k}} \left(x_{\mathbf{k}}y_{\mathbf{k+q}} - z_{\mathbf{k}}z_{\mathbf{k+q}}\right) \frac{1 - f_{\mathbf{k}} - f_{\mathbf{k+q}}}{\omega + i\Gamma + E_{\mathbf{k}} + E_{\mathbf{k+q}}} \\
&+ \frac{P}{N}\sum_{\mathbf{k}} \left(y_{\mathbf{k}}x_{\mathbf{k+q}} - z_{\mathbf{k}}z_{\mathbf{k+q}}\right) \frac{f_{\mathbf{k}} + f_{\mathbf{k+q}} - 1}{\omega + i\Gamma - E_{\mathbf{k}} - E_{\mathbf{k+q}}}
\end{aligned}$$

is the susceptibility in the BCS theory (see equation(38)),

$$\begin{aligned}
\Pi(\mathbf{q},\omega) &= \frac{P}{N}\sum_{\mathbf{k}} \left(x_{\mathbf{k}}x_{\mathbf{k+q}} + z_{\mathbf{k}}z_{\mathbf{k+q}}\right) \frac{t_{\mathbf{k}}f_{\mathbf{k}} - t_{\mathbf{k+q}}f_{\mathbf{k+q}}}{\omega + i\Gamma + E_{\mathbf{k}} - E_{\mathbf{k+q}}} \\
&+ \frac{P}{N}\sum_{\mathbf{k}} \left(y_{\mathbf{k}}y_{\mathbf{k+q}} + z_{\mathbf{k}}z_{\mathbf{k+q}}\right) \frac{t_{\mathbf{k}}\left(1 - f_{\mathbf{k}}\right) - t_{\mathbf{k+q}}\left(1 - f_{\mathbf{k+q}}\right)}{\omega + i\Gamma - E_{\mathbf{k}} + E_{\mathbf{k+q}}} \\
&+ \frac{P}{N}\sum_{\mathbf{k}} \left(x_{\mathbf{k}}y_{\mathbf{k+q}} - z_{\mathbf{k}}z_{\mathbf{k+q}}\right) \frac{t_{\mathbf{k}}f_{\mathbf{k}} - t_{\mathbf{k+q}}\left(1 - f_{\mathbf{k+q}}\right)}{\omega + i\Gamma + E_{\mathbf{k}} + E_{\mathbf{k+q}}} \\
&+ \frac{P}{N}\sum_{\mathbf{k}} \left(y_{\mathbf{k}}x_{\mathbf{k+q}} - z_{\mathbf{k}}z_{\mathbf{k+q}}\right) \frac{t_{\mathbf{k}}\left(1 - f_{\mathbf{k}}\right) - t_{\mathbf{k+q}}f_{\mathbf{k+q}}}{\omega + i\Gamma - E_{\mathbf{k}} - E_{\mathbf{k+q}}}
\end{aligned}$$

as already determined in [25, 53] and

$$
\begin{aligned}
Z(\mathbf{q},\omega) &= \frac{1}{N}\sum_{\mathbf{k}} (P x_{\mathbf{k}} x_{\mathbf{k+q}} + (P-1) z_{\mathbf{k}} z_{\mathbf{k+q}}) \frac{\omega + i\Gamma}{\omega + i\Gamma + E_{\mathbf{k}} - E_{\mathbf{k+q}}} \\
&+ \frac{1}{N}\sum_{\mathbf{k}} (P y_{\mathbf{k}} y_{\mathbf{k+q}} + (P-1) z_{\mathbf{k}} z_{\mathbf{k+q}}) \frac{\omega + i\Gamma}{\omega + i\Gamma - E_{\mathbf{k}} + E_{\mathbf{k+q}}} \\
&+ \frac{1}{N}\sum_{\mathbf{k}} (P x_{\mathbf{k}} y_{\mathbf{k+q}} - (P-1) z_{\mathbf{k}} z_{\mathbf{k+q}}) \frac{\omega + i\Gamma}{\omega + i\Gamma + E_{\mathbf{k}} + E_{\mathbf{k+q}}} \\
&+ \frac{1}{N}\sum_{\mathbf{k}} (P y_{\mathbf{k}} x_{\mathbf{k+q}} - (P-1) z_{\mathbf{k}} z_{\mathbf{k+q}}) \frac{\omega + i\Gamma}{\omega + i\Gamma - E_{\mathbf{k}} - E_{\mathbf{k+q}}}.
\end{aligned}
$$

In the normal state the functions $\chi_0(\mathbf{q},\omega)$, $\Pi(\mathbf{q},\omega)$ and $Z(\mathbf{q},\omega)$ are written as

$$
\chi_0(\mathbf{q},\omega) = \frac{P}{N}\sum_{\mathbf{k}} \frac{f_{\mathbf{k+q}} - f_{\mathbf{k}}}{\omega + i\Gamma + \varepsilon_{\mathbf{k}} - \varepsilon_{\mathbf{k+q}}}
$$

which is the Pauli–Lindhard function,

$$
\Pi(\mathbf{q},\omega) = \frac{P}{N}\sum_{\mathbf{k}} \frac{t_{\mathbf{k}} f_{\mathbf{k}} - t_{\mathbf{k+q}} f_{\mathbf{k+q}}}{\omega + i\Gamma + \varepsilon_{\mathbf{k}} - \varepsilon_{\mathbf{k+q}}}
$$

which is the same correction as determined by Hubbard–Jain [42] and

$$
Z(\mathbf{q},\omega) = \frac{P}{N}\sum_{\mathbf{k}} \frac{\omega + i\Gamma}{\omega + i\Gamma + \varepsilon_{\mathbf{k}} - \varepsilon_{\mathbf{k+q}}}
$$

which is the same function as determined by Zavidonov–Brinkmann [86].

Appendix B

We collect here the temperature dependence of the Fermi surface for various gap symmetries.

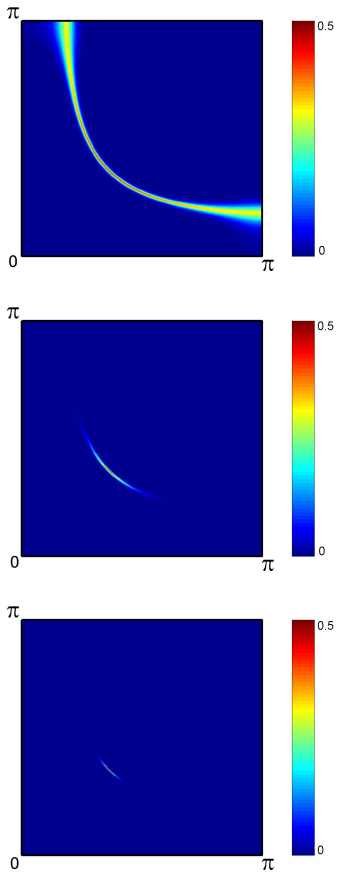

Figure 55: Temperature dependence of the Fermi surface for $d_{x^2-y^2}$–wave gap symmetry in the superconducting state. T=89 K , T=50 K and T=20 K are shown (top to bottom).

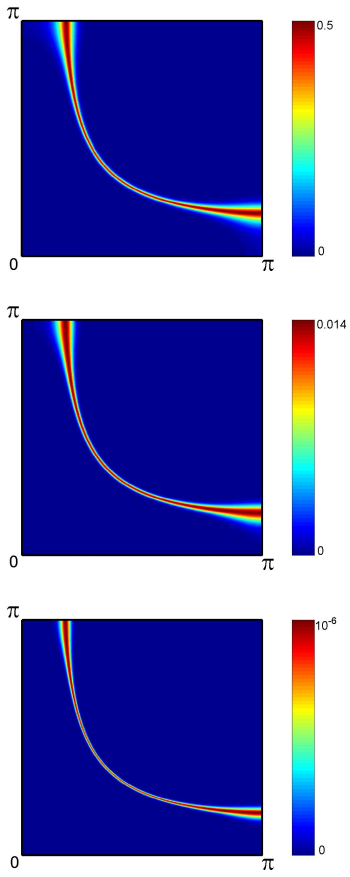

Figure 56: Temperature dependence of the Fermi surface for s–wave gap symmetry in the superconducting state. T=89 K, T=50 K and T=20 K are shown (top to bottom).

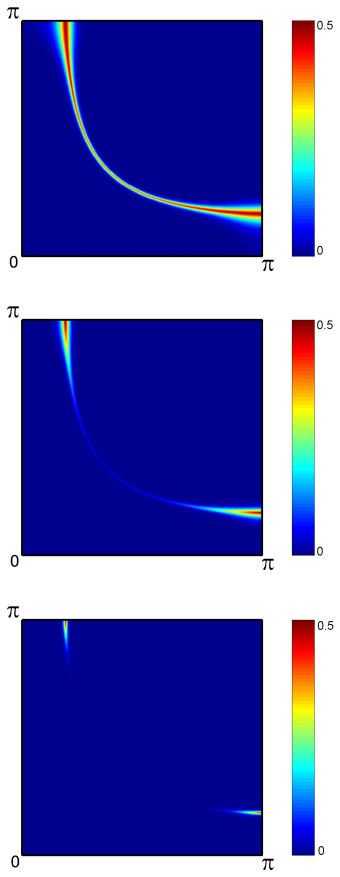

Figure 57: Temperature dependence of the Fermi surface for d_{xy}–wave gap symmetry in the superconducting state. T=89 K, T=50 K and T=20 K are shown (top to bottom).

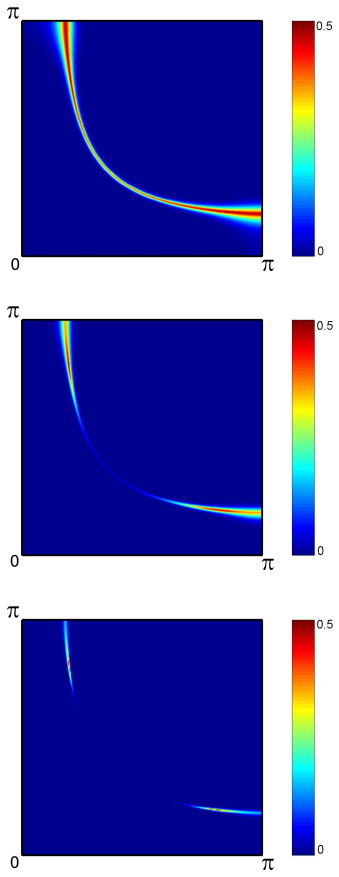

Figure 58: Temperature dependence of the Fermi surface for extended s–wave gap symmetry in the superconducting state. T=89 K, T=50 K and T=20 K are shown (top to bottom).

References

[1] J. Bardeen, L. N. Cooper and J. R. Schrieffer, Phys. Rev. **108**, 1175 (1957)

[2] M. Bankay, M. Mali, J. Roos, I. Mangelschots and D. Brinkmann, Phys. Rev. B **46**, 11228 (1992)

[3] S. E. Barrett, D. J. Durand, C. H. Pennington, C. P. Slichter, T. A. Firedmann, J. P. Rice and D. M. Ginsberg, Phys. Rev. B **41**, 6283 (1990)

[4] K. W. Becker and U. Muschelknautz, Phys. Rev. B **48**, 13826 (1993)

[5] J. G. Bednorz and K. A. Müller, Z. Phys. B **64**, 189 (1986)

[6] J. Beenen and D. M. Edwards, Phys. Rev. B **52,** 13636 (1995)

[7] C. Berthier, M. H. Julien, M. Horvatic and Y. Berthier, J. Phys. I France **6**, 2205 (1996)

[8] P. Bourges, L. P. Regnault, Y. Sidis, C. Vettier, Phys. Rev. B **53**, 876-885 (1996)

[9] D. Brinkmann and M. Mali, NMR Basic Principles and Progress Vol. **31**, 172 (1994)

[10] N. Bulut and D. J. Scalapino, Phys. Rev. B **53**, 5149-5152 (1996)

[11] N .Bulut and D. J. Scalapino, Phys. Rev. B **50**, 16078-16081 (1994)

[12] N. Bulut and D. J. Scalapino, Phys. Rev. B **47**, 3419-3422 (1993)

[13] N. Bulut and D. J. Scalapino, Phys. Rev. Lett. **68**, 706-709 (1992)

[14] N. Bulut and D. J. Scalapino, Phys. Rev. B **45**, 2371-2384 (1992)

[15] N. Bulut and D. J. Scalapino, Phys. Rev. Lett. **67**, 2898-2901 (1991)

[16] N. Bulut, D. Hone, D. J. Scalapino and N. E. Bickers, Phys. Rev. Lett. **64**, 2723-2726 (1990)

[17] N. Bulut, D. W. Hone, D. J. Scalapino and N. E. Bickers, Phys. Rev. B **41**, 1797-1811 (1990)

[18] A. V. Chubukov, D. Pines and J. Schmalian, in Physics of Conventional and Unconventional Superconductors, edited by K. H. Bennemann and J. B. Ketterson (Springer-Verlag, Berlin, 2003, Vol. 1.)

[19] A. Damascelli, Z. Hussain, Zhi-Xun Shen, Rev. Mod. Phys. **75**, 473 (2003)

[20] D. Duffy, P. J. Hirschfeld and D. J. Scalapino, Phys. Rev. B **64**, 224522 (2001)

[21] I. Eremin, Physica B **234-236**, 792 (1997)

[22] I. Eremin, O. Kamaev, and M. V. Eremin, Phys. Rev. B **69**,094517 (2004)

[23] I. Eremin, D. Manske, Phys. Rev. Lett. **94**, 067006 (2005)

[24] I. Eremin, D. K. Morr, A. V. Chubukov, K. Bennemann, M. R. Norman, Phy. Rev. Lett. **94**, 147001 (2005)

[25] M. Eremin, I. Eremin and S. Varlamov, Phys. Rev. B **64**, 214512 (2001)

[26] M. Eremin, O. Kamaev and I. Eremin, Journal of Superconductivity: Incorporating Novel magnetism, Vol. 15 No. 5, 413 (2002)

[27] M. V. Eremin, S. G. Solov'yanov and S. V. Varlamov, JETP **85**, 963 (1997)

[28] M. Eschrig and M. R. Norman, Phys. Rev. Lett. **89**, 277005 (2002)

[29] M. Eschrig and M. R. Norman, Phys. Rev. B **67**, 144503 (2003)

[30] H. Fong, P. Bourges, Y. Sidis, L. P. Regnault, A. Ivanov, G. D. Gu, N. Koshizuka, B. Keimer, Nature **398**, 588-591 (1999)

[31] A. Furrer, Neutron Scattering in Layered Copper–Oxide Superconductors, Kluwer (1998)

[32] A. B. Harris and R. V. Lange, Phys. Rev. **157**, 295 (1967)

[33] H. He, Y. Sidis, P. Bourges, G. D. Gu, A. Ivanov, N. Koshizuka, B. Liang, C. T. Lin, L. P. Regnault, E. Schoenherr, B. Keimer, Phys. Rev. Lett. **86**, 1610 (2001)

[34] L. C. Hebel and C. P. Slichter, Phys. Rev. **107**, 901 (1957)

[35] V. Hinkov, S. Pailhes, P. Bourges, Y. Sidis, A. Ivanhov, A. Kulakov, C. T. Lin, D. P. Chen, C. Bernhard and B. Keimer, Nature **430,** 650-654 (2004)

[36] J .Hubbard, Proc. R. Soc. A, Vol. **276**, 238-257 (1963)

[37] J. Hubbard, Proc. R. Soc. A, Vol. **277**, 237-259 (1964)

[38] J. Hubbard, Proc. R. Soc. A, Vol. **281**, 401-419 (1964)

[39] J. Hubbard, Proc. R. Soc. A, Vol. **285**, 542-560 (1965)

[40] J. Hubbard, Proc. R. Soc. A, Vol. **296**, 82-99 (1967)

[41] J. Hubbard, Proc. R. Soc. A, Vol. **296**, 100-112 (1967)

[42] J. Hubbard and K. P. Jain, J. Phys. C ser. 2, vol 1, 1650 (1968)

[43] P. Hüsser, H. U. Suter, E. P. Stoll, P. F. Meier, Phys. Rev. B **61**, 1567 (2000)

[44] K. Ishida, K. Yoshida, T. Mito, Y. Tokunaga, Y. Kitaoka and K. Asayama, Phys. Rev. B **58**, 5960 (1998)

[45] Y. Itoh, T. Machi, S. Adachi, A. Fukuoka, K. Tanabe and H. Yasuoka, J. Phys. Soc. Jpn. **67**, 312 (1998)

[46] A. A. Kordyuk, S. V. Borisenko, M. Knupfer and J. Fink, Phys. Rev. B **67**, 064504 (2003)

[47] M. L. Kulic, A. I. Lichtenstein, E. Goreatchkovski, M. Mehring, Physica C **244**, 185-192 (1995)

[48] M. L. Kulic, E. Goreatchkovski, A. I. Lichtenstein, M. Mehring, Physica C **252**, 27-48 (1995)

[49] Laura M. Roth, Phys. Rev. Lett. **20,** 1431-1434 (1968)

[50] F. Mack, M. L. Kulic, M. Mehring, Physica C **295**, 136-149 (1998)

[51] J. A. Martindale, S. E. Barrett, K. E. O'Hara, C. P. Slichter, W. C. Lee and D. M. Ginsberg, Phys. Rev. B **47**, 9155 (1993)

[52] T. Mayer, Modellrechnungen zu NMR–Experimenten an Kuprat–Supraleitern, Diplomarbeit (2002)

[53] T. Mayer, M. Eremin, I. Eremin, P. F. Meier, Physica C **400**, 408-410 (2004)

[54] P. F. Meier, Physica C **364**, 411 (2001)

[55] F. Mila and T. M. Rice, Physica C **157**, 561 (1989)

[56] T. Moriya, J. Phys. Soc. Jpn **18** 516-523 (1963)

[57] H. A. Mook, F. Dogan, B. C. Chakoumakos, cond-mat/9811100 (1998)

[58] H. A. Mook, M. Yethiraj, G. Aeppli, T. E. Mason, T. Armstrong, Phys. Rev. Lett. **70**, 3490-3493 (1993)

[59] R. W. Morse, "Progress in Cyrogenics" edited by K. Mendelssohn (Heywood, London), p. 219, Vol I (1959)

[60] M. R. Norman, Phys. Rev. B **63**, 092509 (2000)

[61] W. Nolting, Viel–Teilchen–Theorie, Vieweg (1999)

[62] N. Nücker, J. Fink, J. C. Fuggle, P. J. Durham, W. M. Temmerman, Phys. Rev. B **37**, 5158-5163 (1988)

[63] H. K. Onnes, Leiden Comm. **120b**, **122b** (1911)

[64] F. P. Onufrieva, V. P. Kushnir and B. P. Toperverg, Phys. Rev. B **50**, 12935 (1994)

[65] F. Onufrieva and J. Rossat-Mignod, Phys. Rev. B **52**, 7572 (1995)

[66] S. M. Quinlan, D. J. Scalapino and N. Bulut, Phys. Rev. B **49**, 1470-1473 (1994)

[67] S. Renold, S. Plibersek, E. P. Stoll, T. A. Claxton, P. F. Meier, Eur. Phys. J. B **23**, 3 (2001)

[68] D. Reznik, P. Bourges, L. Pintschovius, Y. Endoh, Y. Sidis, T. Masui and S. Tajima, Phys. Rev. Lett. **93**, 207003 (2004)

[69] A. Rigamonti, F. Borsa and P. Carretta, Rep. Prog. Phys. **61**, 1367-1439 (1998)

[70] A. Schilling, M. Cantoni, J. D. Guo, H. R. Ott, Nature **363**, 56-58 (1993)

[71] J. R. Schrieffer, Theory of Superconductivity, Benjamin (1964)

[72] J. R. Schrieffer and P. A. Wolff, Phys. Rev. **149**, 491 (1966)

[73] I. Sega, P. Prelovsek and J. Bonca, Phys. Rev. B **68**, 054524 (2003)

[74] C. P. Slichter, Principles of Magnetic Resonance, Springer (1990)

[75] R. Stern, M. Mali, J. Roos and D. Brinkman, Phys. Rev. B **51**, 15478 (1995)

[76] A. Sudbo, S. Chakravarty, S. Strong and P. W. Anderson, Phys. Rev. B **49**, 12245-12254 (1994)

[77] M. Takigawa and D. B. Mitzi, Phys. Rev. Lett. **73**, 1287 (1994)

[78] M. Takigawa, J. L. Smith and W. L. Huts, Phys. Rev. B **44**, 7764 (1991)

[79] M. Takigawa, A. P. Reyes, P. C. Hammel, J. D. Thompson, R. H. Heffner, Z. Fisk, and K. C. Ott, Phys. Rev. B **43**, 247 (1991)

[80] T. Tanamoto, H. Kohno and H. Fukuyama, J. Phys. Soc. Jpn. **62**, 1455 (1993)

[81] D. Thelen and D. Pines, Phys. Rev. B **49**, 3528 (1994)

[82] T. Timusk and B. Statt, Rep. Prog. Phys. **62,** 61-122 (1999)

[83] C. C. Tsuei, J. R. Kirtley, Rev. Mod. Phys. **72**, 969 (2000)

[84] K. Yamada, C. H. Lee, K. Kurahashi, J. Wada, S. Wakimoto, S. Ueki, H. Kimura, Y. Endoh, S. Hosoya, G. Shirane, R. J. Birgeneau, M. Greven, M. A. Kastner and Y. J. Kim, Phys. Rev. B **57**, 6165 (1998)

[85] K. Yosida, Phys. Rev. **110**, 769 (1958)

[86] A. Yu. Zavidonov and D. Brinkmann, Phys. Rev. B **58**, 12486 (1998)

[87] Y. Zha, V. Barzykin, D. Pines, Phys. Rev. B **54**, 7561 (1996)

[88] F. C. Zhang and T. M. Rice, Phys. Rev. B **37,** 3759-3761 (1988)

Acknowledgements

This work has been supported by many people. In particular I want to express my gratitude to

P. F. Meier for his enthusiasm, support and encouragement throughout my Diploma and PhD Thesis projects,

M. Eremin and I. Eremin for fruitful collaborations and discussions. Without their pioneering work concerning calculation of the spin susceptibility beyond the random–phase approximation scheme, this Thesis would not have been possible,

H. Keller and H. Beck for being the supervisors of my Thesis,

A. Uldry for proof–reading a part of this work,

M. Mali for bringing to my attention the problematic of the spin susceptibility in the superconducting state of cuprates**,**

CAP group for the extraordinary friendly and helpful working environment, which has made working on this Thesis a pleasurable experience,

My family for their constant support during my Diploma and PhD Thesis work.